Doctoral Dissertation

Development of niobium-based half-Heusler thermoelectric materials with high efficiency and high-temperature stability

高い効率と高い高温安定性を有するニオブ基ハーフホイスラー熱電材料の開発

Wanthana Silpawilawan

December 2019

Graduate School of Engineering

Osaka University

Thesis Advisors:

Associate Professor Hiroaki Muta, Ph.D.
Division of Sustainable Energy and Environmental Engineering,
Graduate school of Engineering, OSAKA UNIVERSITY

Professor Ken Kurosaki, Ph.D. (co-advisors)
Institute for Integrated Radiation and Nuclear Science, KYOTO UNIVERSITY

Thesis Committee:

Professor Takao Yamamoto, Ph.D.
Professor Takaori Kitada, Ph.D.
Associate Professor Yoko Akiyama, Ph.D.
Associate Professor Hiroaki Muta, Ph.D.
Graduate School of Engineering
OSAKA UNIVERSITY

Professor Ken Kurosaki, Ph.D.
Institute for Integrated Radiation and Nuclear Science
KYOTO UNIVERSITY

TABLE OF CONTENTS

Abstract

Thermoelectric (TE) materials have a potential for converting waste heat or heat loss every time an engine runs, a machine operates, into electricity. This feature is beneficial to improve sustainable energy solutions, as well as non-renewable source efficiency in a global. The efficiency of a TE device is determined by a temperature gradient across the device and a material's performance called the TE figure of merit, *zT*. *zT* is determined by $zT = S^2\sigma T\kappa^{-1}$, where *S* is the Seebeck coefficient, σ is the electrical conductivity, *T* is the absolute temperature, and κ is the thermal conductivity ($\kappa = \kappa_{el} + \kappa_{lat}$, the electronic and lattice contributions, respectively). $zT \geq 1$ is a target for the practical applications of TE devices for power generation. Key strategies to achieve this target are increasing *S* and suppressing κ_{lat}. Lately, half-Heusler (HH) compounds are capable of TE materials due to their outstanding performance, excellent electrical properties, especially high *S*. However, to achieve a high-performance module, not only *zT* but high-temperature stability and compatibility of *n*- and *p*-type materials also become vital parameters.

In this thesis, I figure out that the NbFeSb compound is more stable than typical ZrCoSb at high-temperature both in an inert atmosphere and in air. It could be concluded that NbFeSb is more suitable for *p*-type HH TE material than ZrCoSb in the viewpoint of not only the TE properties but also the thermomechanical properties and high-temperature stability. Furthermore, I also studied the substitution effect on the TE properties of NbFeSb substituted 10% Nb site with Ti, Zr, or Hf. In this case, the Ti-substituted sample is improved and exhibited the highest power factor and *zT* values.

Secondly, I am searching for the *n*-type HH compound that provided similar performance and thermomechanical properties with my previous *p*-type for the fabrication of TE generator modules. In this part, I focus on the $Nb_{0.85}CoSb$ system, which exhibits extremely low lattice thermal conductivity and good TE performance due to the Nb-site vacancies, introduce alloy disorder scattering. The results revealed that the Ti-substituted system exhibits better performance in both TE and thermomechanical properties than the Zr- and Hf-substituted

systems. Moreover, the Ti-substituted samples show excellent high-temperature stability in an inert atmosphere up to 1073 K and in the air up to 773 K.

Then, to confirm the experimental results, we theoretically simulate a *2π*-module based on the Nb-based HH compounds of *n*-type $Nb_{0.75}Ti_{0.1}CoSb$ and *p*-type $Nb_{0.9}Ti_{0.1}FeSb$ using the COMSOL code. The maximum conversion efficiency of over 4.0% with the maximum power density of is 2.31 Wcm^{-2} are obtained when the cold-side and hot-side temperatures are 298 K and 773 K, respectively.

Finally, Nb-based HH compounds are developed through substitution, leading to high TE efficiency and high-temperature stability. Furthermore, the compatibility of *n*- and *p*-type TE materials promote a HH TE module with high-performance. I expect this study would lead to a novel strategy for practically useful in TE devices.

Chapter I

Introduction

1.1 Background

Increasing of energy demand since the industrial Revolution was begun in Great Britain in the 18th century, the agricultural societies were transformed into the industrialized and spread to everywhere of the world as well as economic growth and technology have been developed rapidly. To operate all technology, they had to use a massive amount of variety of energy sources, namely oil, natural gas, and coal. At the global viewpoint, more than 85% of the total energy consumption produced by non-renewable resource; coal is the dominant fuel for power generation, accounting for 38%, gas is the second most used fuel of 23%, oil and nuclear is around 10%, and other 18% [1]. In the 21st century, our world was handling severe environmental problems such as pollution, global warming caused by CO_2, and depletion of natural resources [2]. As we know that fossil fuels are creating much harm on earth, contribute to climate change [3-5]. In addition to solving these issues, discovering sustainable and environment-friendly energy, as well as increasing energy efficiency, are an alternative vision for renewable resources [6-7]. Over the last decade, waste heat has become a big part of several sectors, such as industrial, livelihoods, and infrastructure [7-9]. As can be seen from Figure 1.1, 100% of energy input can produce useful energy for the vehicle, only 12.6% apart form that is energy loss in terms of waste heat. To minimized waste heat, energy recovery systems have been more discovered. One of the impressive technology to resolve this issue is thermoelectric (TE) conversion technology. This technology could convert waste heat into useful energy. In order to achieve recovery of waste

heat, the temperature difference between the heat source and heat sink is a significant determinant of quality. However, the quality of waste heat recovery can be categorized by the temperature range of the waste heat sources; (1) high-quality (at temperature above 650 ^{o}C, e.g., industrial plants), (2) medium-quality (at 232 - 650 ^{o}C, e.g., vehicle, steam and power generation), and (3) low-quality (below 232 ^{o}C, e.g., household utilities, geothermal sources). Nonetheless, the most advantages part for practical used are from a part of the medium to high-quality heat source [10]. Waste heat recovery technology or TE conversion technology has been developed for several years, we know as, thermoelectric generators (TEGs).

TEGs working on a class of TE materials [11-14]. This material can convert waste heat from varied sources, namely automotive exhaust, industrial processes, electronics, power generation, and even a small portion like heat from human-body, to electric energy. TEGs consists of a series of couples of *n*- and *p*-type TE material operating between a temperature difference. It can be competent in representing solid-state heat pumps which without any moving parts, and machine running sound, and reliable, making them ideal for environmental-friendly and given power generation [15,16]. However, improving the efficiency of waste heat recovering is a big challenge for this research field. TE device has been achieved since the middle of 1999s in several TE materials. According to the appropriate operating temperature, the TE materials can be classified into three groups. 1) low-temperature range <400 K is Bi_2Ti_3 based. 2) middle-temperature range 600 – 900 K is PbTe based, half-Heusler compound, and Skutterudite. 3) high-temperate range >900 K is SiGe based [17]. Technically, the efficiency of TE materials can be determined by $zT = S^2\sigma T/\kappa_e + \kappa_{lat}$, where zT is the dimensionless figure of merit, S is the Seebeck coefficient, σ is the electrical conductivity, T is the absolute temperature, κ_e and κ_{lat} are electronic and lattice thermal conductivity, respectively. $zT \geq 1$ is a target for the practical applications of TE devices for power generation. Key strategies to achieve this target are increasing S through band engineering [18-20] and suppressing κ_{lat} by introducing phonon scattering through alloying, nanostructuring, and rattling [21-24]. However, above strategies could be improved the performance of TE material. On the other hand, in the viewpoint of the TE module, not only high zT but operated-temperature range, thermomechanical properties of TE material, and compatibility of *n*- and *p*-type also necessary for enhancing the efficiency of TE module.

To date, a promising candidate for thermoelectric such as Zintl phases, clathrates, and skutterudites have been revealed and high efficiency, as known as complex bulk materials [25-27]. Furthermore, Half-Heusler (HH) compounds are one of the most promising candidates for such advanced TE materials, which excellence electrical performance, stable at high-temperature, good mechanical properties, and non-toxic as well as working on mid-to-high temperature range [20,28-36]. According to my earlier point, HH compounds have gained much attention in present research studied and are selected for the fabrication of a TE module. Furthermore, to develop high performance TE module not only TE properties but also thermal stability and compatibility of *n*-type and *p*-type materials are needed.

This dissertation comprises five chapters; Chapter I introduces the principle of TE effect, including the TE properties (electron and phonon transportation in TE materials), and the efficiency of the TE module are described. Based on the above strategies, thermomechanical properties such as high-temperature stability and thermal expansion coefficient are reviewed. Moreover, the advantages of Nb-based HH compounds are showing in this chapter. Chapter II, the high-temperature stability and thermal expansion coefficient of *p*-type NbFeSb, are investigated. This result confirmed that NbFeSb exhibits more suitable for *p*-type HH TE material than traditional *p*-type HH compounds (ZrCoSb). Furthermore, the TE performance of *p*-type NbFeSb is improved through the substitution technique. $Nb_{1-x}M_xFeSb$ is substituted by 10% of Ti, Zr, Hf at Nb site. TE properties and thermomechanical properties are performed in the temperature range of 300 – 1073 K. For *n*-type HH compounds, Nb_yCoSb is a representative of *n*-type Nb-based HH compounds in the present studied. The advantage of Nb_yCoSb is explained in Chapter III. Also, the TE performance enhancement of $Nb_{0.75}M_{0.1}CoSb$ (*M* = Ti, Zr, and Hf) is investigated under the condition relevant to the previous chapter. In Chapter IV, the best *p*-type and *n*-type Nb-based HH compounds from Chapters II and III are created as 2π-module by multiphysics modeling in the COMSOL program to simulate the conversion efficiency and power output of the 2π-module. Finally, Chapter V will conclude all the results in this dissertation. The critical knowledge point in this dissertation plays an essential role in practical application.

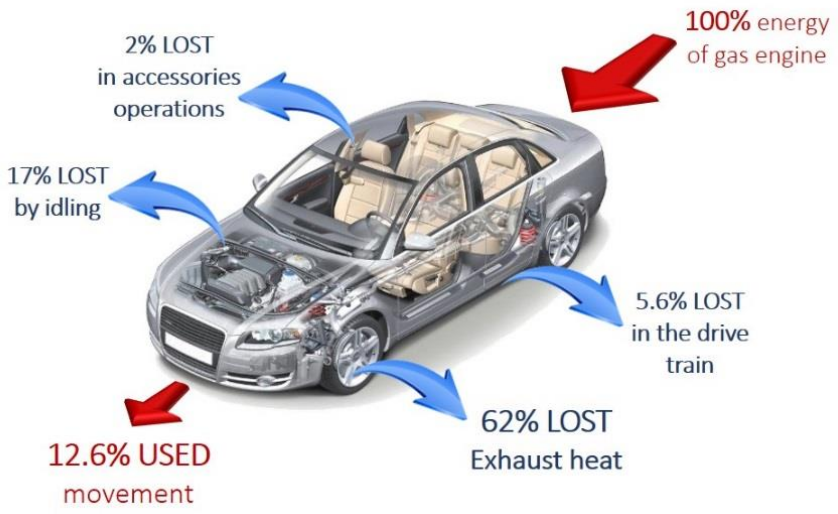

Figure 1.1 Energy loss in a vehicle, currently vehicles are only able to use around 20% of the energy content of the fuel as power, the heat loss around 62%, is big part form exhaust heat [40].

1.2 Thermoelectric Phenomena and Their Application

To understand the performance of thermoelectric generator (TEGs), it is vital to understand the principal theory of thermoelectricity effect, which is discussed below based on the three TE effects; the Seebeck effect, Peltier effect, Thomson effect, and Hall effect.

1.2.1 Basic Thermoelectric Effect

Thermoelectric (TE) phenomena were found in 1821 by Thomas Johann Seebeck, the German physicist. He realized that the loop made by two different metals, A and B. There are two junctions in the circuit (joined H and C). If between the junction H and C has a different temperature, both charged carrier electron and hole, moves from the hot side to the cold side. Then the current would flow in the loop. The voltage, V, has linearly related to the temperature difference of both parties, ΔT. The constant of this relation is called the Seebeck coefficient, S, given as;

$$S_{AB} = \frac{V}{\Delta T} = S_A - S_B, \tag{1.1}$$

where both S_A and S_B are the absolute S values of the conductors. As shown in Figure 1.2a, between these two junctions of two difference materials occurs the Seebeck effect during a temperature gradient. The Seebeck effect determined the founding of a voltage gradient (V) across a material in response to a temperature gradient [37].

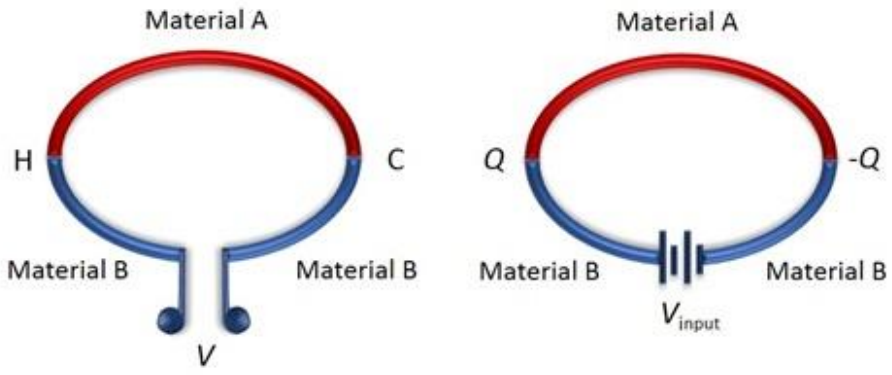

Figure 1.2 Schematic illustration of (a) Seebeck effects and (b) Peltier effects

The temperature gradient creates a higher charge carrier's concentration at the cold side of the sample, which corresponds to the generation of a voltage differential across the specimen. The sign of the Seebeck coefficient is typically negative for *n*-type electrical conduction, where electrons are the primary charge carriers and positive for *p*-type conduction, where holes are the majority carriers.

In contrast, the Peltier effect was discovered in 1834 by Jean Charles Athanase Peltier. It was explained that an electrical current could cause temperature difference at the junction under isothermal conditions, as shown in Figure 1.2b. The Peltier coefficient (Π) is described as the following equation;

$$\Pi_{AB} = \frac{1}{I}\frac{dQ_{AB}}{dt} \tag{1.2}$$

where, I and dQ_{AB}/dt are the electrical currents and the rate of heat transfer at the junction, respectively. When the voltage is applied, the Peltier heat Q generates at one intersection, and the Peltier cooling $-Q$ generates at the other terminal. The dependence of the Peltier effect upon

the current suggests a greater degree of control over the performance of a thermoelectric device than does the Seebeck effect, which measures the tendency of material for establishing a voltage gradient in response to a temperature gradient.

Next, the Thomson effect describes the radiation or absorption of heat energy from a material that has both temperature and voltage gradients. The Thompson effect states that in the absence of Joule heating, the heat gained or lost is given by

$$\tau = \frac{dQ_{\mathrm{T}}}{IdtdT} \tag{1.3}$$

where τ, Q, I, t and T are the Thomson coefficient, heat, electrical current, spatial coordinate, and temperature, respectively. It should be noted that while the Seebeck and Peltier coefficients describe heat transfer in a system of two dissimilar materials, the Thompson effect describes heat flow in a single material. From the Thompson effect, it can be shown that

$$\tau_{\mathrm{A}} - \tau_{\mathrm{B}} = T\frac{dS_{\mathrm{AB}}}{dT} \tag{1.4}$$

and consequently that

$$\Pi_{\mathrm{AB}} = S_{\mathrm{AB}}T \tag{1.5}$$

The Thomson effect leads to a direct relationship between the Seebeck and Peltier coefficient.

Edwin Herbert Hall discovered the Hall effect in the year 1879. It signifies the response of charge carriers by an electric field within a conductor due to an applied magnetic field B, which is arranged non-parallel to a direction of a current density j (i.e., $j \times B$). The charge carriers experience a Lorentz force due to the perpendicular magnetic component and, as a result, are deflected from their original path and accumulated vertically to the direction of the electrical current. The accumulation of charge carriers gives rise to the generation of a voltage perpendicular to the direction of the electrical current and is denoted as the Hall voltage. The Hall effect is reversible and only observed if a magnetic field is applied. In the simple case, the charge carriers create the Hall voltage VH due to the magnetic field B, which is given by

$$V_{\mathrm{H}} = \frac{-I \cdot B}{n_{\mathrm{H}} \cdot e \cdot d} \tag{1.6}$$

Where the I is an applied current, B is a magnetic field, d is the thickness of the specimen, e is an electron charge and n_{H} is a charge carrier concentration. Hall coefficient R_{H} is defined as

$$R_{\mathrm{H}} = \frac{E_y}{j_x \cdot B} = \frac{U_{\mathrm{H}} \cdot t}{I \cdot B} = \frac{1}{n_{\mathrm{H}} \cdot e} \tag{1.7}$$

E_y is the induced transversal electrical field and j_x is the direction of the current density (perpendicular to the magnetic field). Latter is defined as $j_x = ne^2\tau E_x/m$, where τ is the charge carrier relaxation time, E_x is the longitudinal electrical field and m is a mass of the carriers. The charge carrier concentration means an effective charge carrier concentration, which is a superposition of minority and majority charge carrier concentrations. This is accordingly to the of the charge carrier mass m, which also becomes a superposition of two distinct charge carrier masses. Furthermore, the Hall mobility μ_{H} of a particular material can be derived from the relation between the Hall constant RH and the electrical conductivity σ, which is expressed as $\mu_{\mathrm{H}} = |\sigma \cdot R_{\mathrm{H}}|$.

1.2.2 Thermoelectric Figure of Merit and Conversion Efficiency

Using Seekbeck effect, the TE device can generate electric power. When one side of TE device is heated, the thermoelectric voltage is induced in proportion to the temperature difference. While Peltier effect act as the refrigerator. The principal of TE module consists of pairs n-type and p-type legs as shows in Figure 1.3a heat generator and 1.3b refrigerator. n- and p-type legs are connected electrically in series and thermally in parallel. The total electrical resistance and thermal conductance of n- and p-type materials are given as

$$r_{np} = L\left(\frac{\rho_n}{A_n} + \frac{\rho_p}{A_p}\right) \tag{1.8}$$

$$K_{np} = \kappa_n A_n + \kappa_p A_p \tag{1.9}$$

Where the ρ, L, A and κ are the resistivity, the length, the cross section area of the legs and the thermal conductivity, respectively.

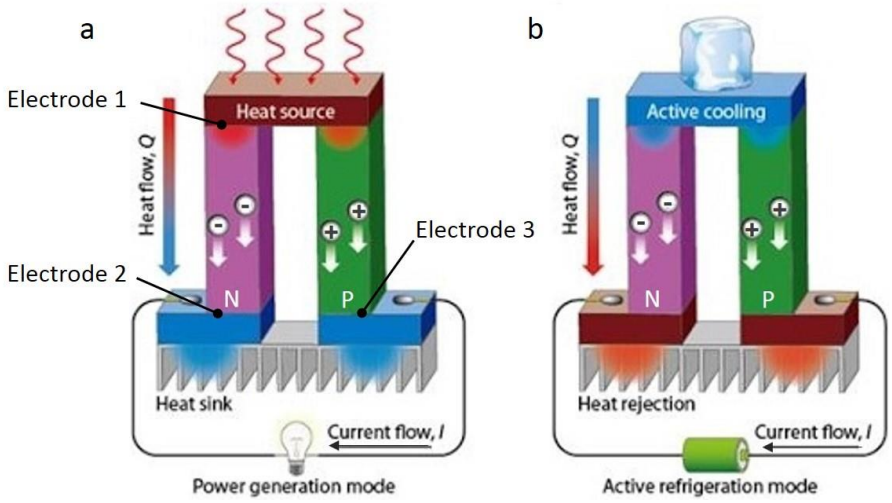

Figure 1.3 Schematic of a TE couple consisted of *n*-type and *p*-type thermoelectric material for (a) TE power generation and (b) TE cooler. Figure from reference [38].

To prove the relation of thermoelectric figure of merit (zT) and conversion efficiency (η), the character of TE power generation is considered.

At electrode 1, the total heat flow (Q_{total}) contained, Q_{np} is the absorbing heat, $Q_{H\to L}$ is the heat flow from total thermal conductance, and $Q_{J\to H}$ is the heat flow from the Joule heating. So,

$$Q_{np} = S_{np} I T_H \tag{1.10}$$

$$Q_{H\to L} = -K_{np}(T_H - T_C) \tag{1.11}$$

$$Q_{J\to H} = \frac{1}{2} I^2 r_{np} \tag{1.12}$$

I is the current in the closed circuit. S_{np} is the Seebeck coefficient of this circuit. S_n and S_p are the Seebeck coefficients of n-type and p-type segments, respectively.

$$S_{np} = S_n - S_p \tag{1.13}$$

$$Q_{total} = -Q_{np} - Q_{H\to L} + Q_{J\to H} \tag{1.14}$$

$$Q_{total} = S_{np} I T_{\mathrm{H}} + K_{np}(T_{\mathrm{H}} - T_{\mathrm{C}}) - \frac{1}{2} I^2 r_{np} \tag{1.15}$$

Also, if V is the thermal electromotive force,

$$I = \frac{V}{R + r_{np}} = \frac{S_{np}(T_{\mathrm{H}} - T_{\mathrm{C}})}{R + r_{np}} \tag{1.16}$$

If R is the load resistance and P is the output power,

$$P = \left[S_{np}(T_{\mathrm{H}} - T_{\mathrm{C}}) \right]^2 \frac{R}{(R + r_{np})^2} \tag{1.17}$$

From above relations, the conversion efficiency η for whole circuit is

$$\eta = \frac{P}{Q_{total}} = \frac{\left[S_{np}(T_{\mathrm{H}} - T_{\mathrm{C}}) \right]^2 \dfrac{R}{(R + r_{np})^2}}{S_{np} I T_{\mathrm{H}} + K_{np}(T_{\mathrm{H}} - T_{\mathrm{C}}) - \dfrac{1}{2} I^2 r_{np}} = \frac{T_{\mathrm{H}} - T_{\mathrm{C}}}{T_{\mathrm{H}}} \frac{R / r_{np}}{1 + \dfrac{K_{np} r_{np} (R + r_{np})^2}{S_{np}^2 T_{\mathrm{H}} r_{np}^2} - \dfrac{T_{\mathrm{H}} - T_{\mathrm{C}}}{2 T_{\mathrm{H}}}} \tag{1.18}$$

$K_{np}r_{np}$ could be minimized as the selection of cross section area in semiconductors.

$$\frac{\kappa_n \rho_p}{\kappa_p \rho_n} = \left(\frac{A_p}{A_n} \right)^2 \tag{1.19}$$

If one selects cross section area to satisfy the equation (1.19), the efficiency is

$$\eta = \frac{T_{\mathrm{H}} - T_{\mathrm{C}}}{T_{\mathrm{H}}} \frac{R / r_{np}}{1 + \dfrac{1(R + r_{np})^2}{Z_{np} T_{\mathrm{H}} r_{np}^2} - \dfrac{T_{\mathrm{H}} - T_{\mathrm{C}}}{2 T_{\mathrm{H}}}} \tag{1.20}$$

$$Z_{np} = \frac{S_{np}^2}{\left(\sqrt{\kappa_p \rho_p} + \sqrt{\kappa_n \rho_n} \right)^2} \tag{1.21}$$

Z_{np} is the TE figure of merit from the properties of semiconductor. From the above Equation 1.20 and 1.21, one can know that the conversion efficiency is the harmonic increment function of Z_{np}. The figure of merit for each leg is

$$Z = \frac{S^2}{\kappa \rho} = \frac{S^2 \sigma}{\kappa} \tag{1.22}$$

Where σ is the electrical conductivity and $S^2\sigma$ is power factor. In order to maximize the conversion efficiency, the ratio between external and internal resistance is regard as $m=R/r_{np}$.

$$\eta = \frac{T_H - T_C}{T_H} \frac{\frac{m}{m+1}}{1 + \frac{1}{Z_{np}} \frac{m+1}{T_H} - \frac{T_H - T_C}{2T_H(m+1)}} \tag{1.23}$$

by $\partial\eta/\partial m = 0$,

$$m_{opt} = \sqrt{1 + z_{np} \frac{T_H + T_C}{2}} = \sqrt{1+zT} \tag{1.24}$$

Here, zT is called as dimensionless figure of merit, written by

$$zT = \frac{S^2\sigma}{\kappa_{total}} T \tag{1.25}$$

Where κ_{total} is the sum of thermal conductivity contributions from electron (κ_e) and lattice phonons (κ_{lat}), $\kappa_{total} = \kappa_e + \kappa_{lat}$. $S^2\sigma$ term is defined as power factor (PF), which estimates the capability of a TE material to produce useful electricity. From above equation, the efficiency of thermoelectric module (or thermoelectric generator) is given by the following equation.

$$\eta = \frac{T_H - T_C}{T_H} \frac{\sqrt{1+zT} - 1}{\sqrt{1+zT} + \frac{T_C}{T_H}} \tag{1.26}$$

A potential TE material for application must have a higher zT value. From equation 1.25 large Seebeck coefficient, high electrical conductivity, and low thermal conductivity are required for high zT. Furthermore, the high efficiency value for a TE module can be obtained by enhancing zT. This relation is shown in Figure 1.4

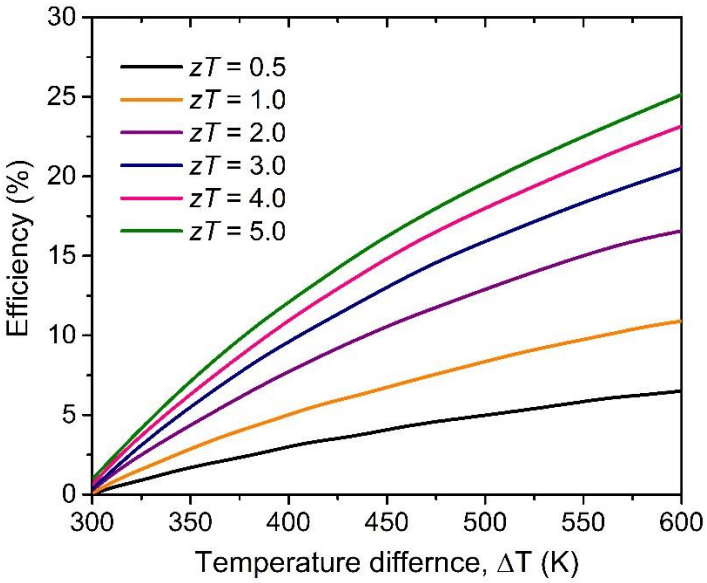

Figure 1.4 Thermoelectric conversion efficiency (η) estimated as a function of zT and temperature difference (ΔT) of thermoelectric leg. Figure from reference 39.

The relation between η from equation 1.26 and zT is plotted in Figure 1.4. It can be explained that high zT provided the high efficiency for TE single leg. To reach maximum thermoelectric efficiency, more massive temperature difference, and high zT value are essential. As can be seen, if maximum zT = 5.0 and ΔT = 600 K the maximum conversion efficiency (η_{max}) can be reach up to 25%, comparable to TE material with zT around 1.0, η_{max} is achieved to 10% when the temperature difference is same. However, zT of TE material can be improved through understanding the conflicting properties of TE material as shown in Figure 1.5.

The conflicting parameter between Seebeck coefficient (S) and electrical conductivity (σ) through carrier concentration (n) of metals or degenerate semiconductors, is given below.

$$S = \frac{8\pi^2 k_B^2}{3e\hbar^2} m^* T \left(\frac{\pi}{3n}\right)^{2/3} \tag{1.27}$$

where k_B, e, h, m^* are Boltzmann constant, electron charge, Planck constant, and effective mass, respectively.

The electrical conductivity and electrical resistivity (ρ) are related to n through the carrier mobility (μ),

$$\frac{1}{\rho} = \sigma = ne\mu \tag{1.28}$$

Figure 1.5 shows the compromise between large power factor and high electrical conductivity in thermoelectric materials that could be blocked to maximize the *zT*. The peak of the power factor typically occurs at carrier concentrations between 10^{19} to 10^{21} cm^{-3}, depending on the material system.

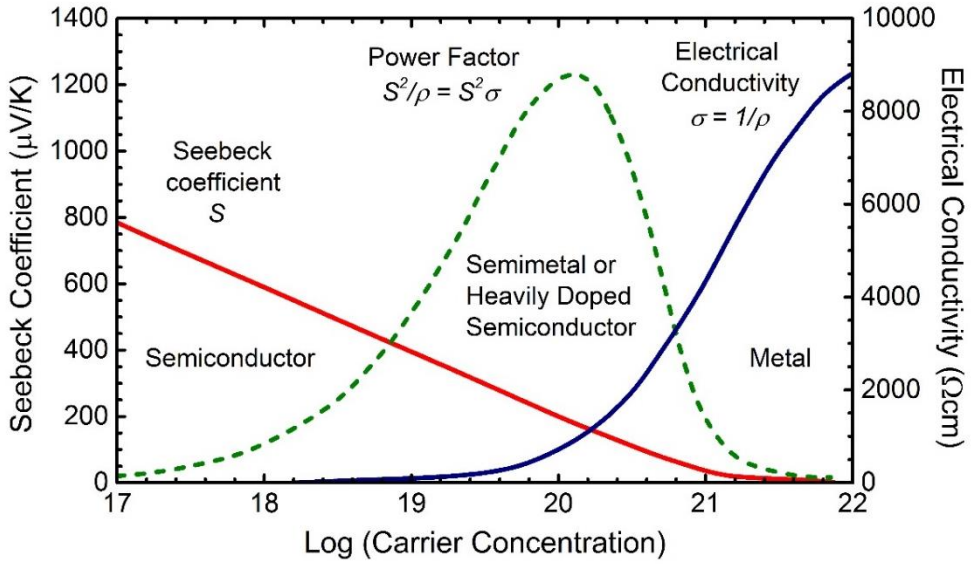

Figure 1.5 Carrier concentration dependence of thermoelectric properties.

The thermoelectric power factor maximizes somewhere between metal and semiconductors. Suitable thermoelectric materials are typically exhibited by heavily doped semiconductors such as SnSe, Skutterudites, and half-Heusler compounds. As mentioned above, the optimization of carrier concentration should be considered to improve a large power factor and lead to enhance the *zT* of TE materials. [40]

1.3 Electron and phonon transportation

The characterization of TE materials primarily in The characterization of TE materials involves mostly the measurement of the variables in equation $zT = S^2\sigma T/\kappa$, which are the temperature-dependent values of S, ρ, and κ. This a reasonable equation because the efficiency of the TE materials is the main topic for the advancement of the research on TE materials. For the further understanding of the materials, however, a physical interpretation of the particular variables is necessary. This complicated by the fact that S, ρ and κ are interdependent on each other and are determined by several different phenomena [41-43].

Both, the single parabolic band model and the Debye approximation facilitate the interpretation of the measured transport properties of the HH material. The former issued to interpret the electronic characteristics of the HH material and its deviations from metal with a single parabolic band structure. The other, the Debye approximation, estimates the weighing of different scattering types (e.g., phonon-phonon interactions or scattering at crystal defects). Moreover, it consequently gives more insight into the lattice thermal conductivity of the material and helps to interpret possible deviations from this model further. These models can be applied to HH materials. The details will be discussed in the next Chapter.

1.3.1 Single parabolic band model

Attempts to thoroughly understand the transport properties, a single parabolic band (SPB) model is used. The electrical transport properties can be explained through a useful single band model for different carrier scattering mechanisms. The ideal of parabolic band approximation having energy which prediction transport properties in a thermoelectric material. The following equation can express it almost up to the Brillouin zone boundaries.

$$E(k) = \frac{h^2 k^2}{2m_b^*} \tag{1.29}$$

where $E(k)$ is the energy of electron states, h is the reduced Planck constant, k is the crystal momentum and m_b^* is the band effective mass.

The number of free electron limit given by Ohm's law as:

$$\sigma = \frac{ne^2\tau}{m^*} = ne\mu \tag{1.30}$$

Equation 1.30 shows that the electrical conductivity (in terms of effective mass m^*) depends on both the carrier density n and the carrier mobility μ. Where the effective mass is obtained from the band curvature $1/m^* = \partial^2 E/\hbar^2 \partial k^2$. The generalization of Ohm's law and be made to deal with solids for which the effective mass tensor is anisotropic.

The Fermi integral is written as

$$F(\eta)_i = \int_0^\infty \frac{x^i dx}{1 + e^{(x-\eta)}} \tag{1.31}$$

$$S = \frac{k_B}{e}\left[\frac{2F_1(\eta)}{F_0(\eta)} - \eta\right] \tag{1.32}$$

$$n_H = 4\pi\left[\frac{2m^* k_B T}{h}\right]^{3/2} \frac{F_{1/2}(\eta)}{r_H} \tag{1.33}$$

where F_i is the Fermi Dirac integral of order i, η is the reduced Fermi energy, k_B is the Boltzmann constant, h is the Planck constant, and r_H is the Hall factor (for HH compound in this study, r_H = 1).

Thermal transport, similar as electrical transport follows from Boltzmann equation. The total thermal conductivity κ of any material is combined with the electronic thermal conductivity, κ_e and lattice thermal conductivity, κ_{lat}.

$$\kappa = \kappa_e + \kappa_{lat} \tag{1.34}$$

The electronic thermal conductivity, κ_e is approximated with the Wiedemann-Franz law.

$$\kappa_e = L\sigma T \tag{1.35}$$

where L is the Lorenz number, which also can be calculated by using a single parabolic band:

$$L = \frac{k^2}{e^2} \frac{(1+\lambda)(3+\lambda)F_\lambda(\eta)F_{\lambda+2}(\eta) - (2+\lambda)^2 F_{\lambda+1}(\eta)^2}{(1+\lambda)^2 F_\lambda(\eta)} \tag{1.36}$$

for free electrons $L = 2.45 \times 10^{-8}$ WΩK^{-2}.

1.3.2 Debye model

The Debye model used to approximate all phonon modes to have a similar velocity in the dispersion relation of frequency versus wave vector as the following equation:

$$\omega = c \times k \tag{1.37}$$

Where the ω is an angular frequency, the c is the speed of light and k is the wave vector. Using this approximation based on the Boltzmann equation can be attained.

The lattice thermal conductivity, κ_{lat} is independent of electrical properties because it is contributed by phonons traveling through the crystal lattice transport heat. An ideal property for a TE material is Phonon Glass-Electron Crystal (PGEC). Therefore, an approach of minimizing lattice thermal conductivity by phonon scattering while maintaining, or increasing carrier mobility is considered as the greatest way to enhance zT. The lattice thermal conductivity can be defined by:

$$\kappa_{lat} = \frac{1}{3} C_v v l \tag{1.38}$$

C_v is the specific heat capacity, v the mean velocity of the particles (phonons) and l is the mean free path between two scattering events.

The phonon relaxation time τ_{ph}, which consists of several scattering types, can be approximated and compared to the experimental data. In this model, the lattice thermal conductivity κ_{lat} is derived from the thermal conductivity data $\kappa(T)$ by application of the Wiedemann-Franz law and the calculated Lorenz number L_0. In the following, the derivation of the lattice thermal.

$$\tau^{-1} = \tau_{\text{U}}^{-1} + \tau_{\text{B}}^{-1} + \tau_{\text{PD}}^{-1} \tag{1.39}$$

where τ_U, τ_B and τ_{PD} are Umklapp scattering, boundary scattering, point defect scattering, respectively.

1. Phonon-phonon Umklapp scattering

$$\tau_U^{-1} = \frac{\overline{M}v^3}{V^{1/3}\omega^2\gamma^2 T} \tag{1.40}$$

Phonon-phonon process, also known as Umklapp scattering, is strongly related to the harmonicity between the bonding, described by the Gruneisen parameter (γ), average mass ($\overline{M}$), and temperature (T) [44]. The phonon-phonon process usually becomes the dominant phonon interaction with increasing temperature.

2. Boundary scattering

$$\tau_B^{-1} = \frac{d}{v_g} \tag{1.41}$$

Boundary scattering in polycrystalline materials can be estimated from grain size d and group velocity v_g, according to Equation 1.41. This scattering influenced by low dimensional materials such as nanostructures, nanowires, thin films, and nanocomposites [45, 46].

3. Point Defect Scattering

$$\tau_{PD}^{-1} = \frac{V\omega^4}{4\pi v_p^2 v_g}\left(\sum_i f_i\left(1-\frac{m_i}{m^*}\right)^2 + \sum_i f_i\left(1-\frac{r_i}{r^*}\right)^2\right) \tag{1.42}$$

Point defect scattering is contributed by both strain contrast and mass induced by point defects within the lattice structure of a material. The lattice disorder in a material due to alloying, can be described by point defect scattering, as shown in Equation 1.42. Here, f_i is the fraction of atoms with mass m_i and radii r_i, that consistent with the average mass m^* and radius r^* and, respectively [47-49].

1.4 Thermal stability

Further to my previous point, to develop a high-performance TE module, not only TE properties but also thermal stability and compatibility of *p*-type and *n*-type materials become key parameters. The thermal stability of materials is necessary for the TE module, which working under high-temperature differences. Notably, the similarity of TE properties as well as thermal stability between *p*-type and *n*-type TE material. In this dissertation, I focus on two parameters that provide a high-performance in the TE module 1. high-temperature stability and 2. thermal expansion coefficient. The thermal expansion coefficient (α_L) is used to determine the expansion characteristics as a function of temperature. To clearly understand, the detail of these two parameters are described below.

1.4.1 High-temperature stability

High-temperature stability of TE material represents by phase stability during heating. This temperature behavior of materials can be determined via high-temperature powder X-rays diffraction method (HT-XRD) (see Figure 2.4) in the temperature range from room temperature to 1073 K. The powder XRD investigation of the sample is performed by using Cu Kα monochromatic radiation and a scintillation counter to achieve highest resolution. To verify phase stability, the powder samples are placed in a chamber, which different atmospheres (continuous helium-flow or in the air) and high-temperature attachment. It is expected that the sample maintains a constant phase geometry of the experiment.

Owing to the practical use of the TE module, the TE material would be mechanically and chemically stable throughout the entire temperature range of operation intended. It means a melting point sufficiently high, a slow oxidation rate, maintains the chemical composition, and no phase transitions within the corresponding temperature. Materials such as TAGS or $LaTe_x$ alloys have been little used or abandoned because of the difficulties in handling them at high temperatures. Other materials such as high-quality Bi-Sb and Bi_2Te_3 based alloys are not mechanically robust, due in particular to their anisotropic crystal structure which results in the existence of cleavage planes [50]. Therefore, suitability as high-temperature stability of TE materials is determined by the purpose of application temperatures, as summarized in Table 1.1.

Table 1.1 Classification of thermoelectric material [51]

Low temperature material (20– 350 ºC)	**Intermediate temperature material (350 – 600 ºC)**	**High temperature material (> 600 ºC)**
Bismuth telluride, Lead-Telluride, Mg_2Si	Skutterudites, Half-Heusler, Clathrates	Silicon-Germanium, Silicide, Tin selenide, $SrTiO_3$(Oxide compounds)

Thermoelectric materials can be roughly divided into the groups of low, intermediate, and high-temperature materials according to their application temperatures. However, the optimal application range of the half-Heusler compound is between 400-600 ºC [52]. As mentioned before, the most advantageous part for practical use belongs to the medium to the high-quality heat source, which relevant to the application temperatures.

1.4.2 Thermal expansion coefficient

Among those parameters, the thermal expansion coefficient is critically important. Linear thermal expansion coefficient (α_L) is a mechanical property of the material that indicates the length change of the sample upon heating. The α_L defined as the fractional of length change per unit rise in temperature can be expressed as:

$$\alpha_L = \frac{1}{L_{RT}} \frac{L(T) - L_{RT}}{T - T_{RT}} \tag{1.43}$$

Where L_{RT} is the sample's length at room temperature.

To investigate the thermal expansion coefficient, two physical quantities (displacement and temperature) must be measured on a sample that is undergoing a thermal cycle. Technically, three primary techniques for α_L measurement are dilatometry, interferometry, and X-ray diffraction analysis [53].

Dilatometry techniques are widely used. A specimen is heated with following Ar gas. Displacement of the specimen is transmitted to a sensor through pushrods, as shown in Figure 2.4. The length change of specimen is compared with the reference Alumina as the result of Alumina can extend the temperature range up to 1600 ^{o}C.

Interferometry using optical interference techniques. Displacement of the specimen ends is measured in terms of the number of wavelengths of monochromatic light. Precision is significantly higher than with thermomechanical dilatometry. However, the technique relies on the optical reflectance of the specimen surface. Interferometry is not used much above 700 °C.

X-ray diffraction analysis can be used to study the lattice parameter changes during heating. The lattice parameter is obtained using HT-XRD (Figure 2.3). A second-order polynomial can fit the temperature dependence of lattice parameter (a) as:

$$a(T) = a_0 + a_1 T + a_2 T^2 \tag{1.44}$$

Where a_0, a_1, and a_2 are fitting parameter.

According to the definition of the linear thermal expansion coefficient (α_L) (equation 1.43), $\alpha_L=(1/a)(da/dT)$, we obtain the temperature dependence of the thermal expansion coefficient as: [54]

$$\alpha_L(T) = \left(a_1 + 2a_2 T\right) \Big/ \left(a_0 + a_1 T + a_2 T^2\right) \tag{1.45}$$

In our laboratory, α_L value can be evaluated by using two methods 1) dilatometer measurement and 2) calculated from lattice expansion by high-temperature x-ray diffraction (HT-XRD) method.

Additionally, thermal expansion is practically and theoretically crucial for predicting residual stresses in electronic devices and also TE module. The decision in this issue is a small percentage of linear thermal expansion coefficient difference (%$\Delta\alpha_L$) between *p*-type and *n*-type TE material. These values would be avoiding the ineffective in the thermoelectric module during operating on high temperature. The linear thermal expansion coefficient of well-known couple TE materials is summarized in Table 1.2.

Table 1.2 Published data on the linear thermal expansion coefficients of a variety of couple thermoelectric materials

TE Module *p* / *n*	**type**	zT_{max}	α_L **(×10^{-6} K^{-1}) from RT**	**Reference**	**%$\Delta\alpha_L$**
FeNbSb / ZrNiSn	*p*	1.5	9.0×10^{-6} @1073K	[34]	18
	n	1.2	11.0×10^{-6} @673K	[55]	
*M*CoSb / *M*NiSn	*p*	0.5	8.8×10^{-6} @1073K	[34]	20
	n	1.2	11.0×10^{-6} @673K	[55]	
$MnSi_{1.75}$ / $Mg_2(Si\text{-}Sn)$	*p*	0.5	9.9×10^{-6} @298K	[56]	45
	n	1.3	20.0×10^{-6} @723K	[57]	
$Ca_3Co_4O_9$ / $In_{1.95}Sn_{0.05}O_3$	*p*	0.21	10.9×10^{-6} @973K	[58]	26
	n	0.07	14.7×10^{-6} @1173K	[59]	
Cu_2Se / $Yb_{0.3}Co_4Sb_{12}$	*p*	1.19	23.0×10^{-6} @773K	[60]	56
	n	1.5	10.0×10^{-6} @600K	[61]	
Bi_2Te_3 / PbTe	*p*	1.2	17.1×10^{-6} @298K	[62]	21
	n	0.97	20×10^{-6} @300K	[63]	
$Ge_{0.15}$-$Si_{0.85}$/ $Ge_{0.15}$-$Si_{0.85}$	*p*	0.8	5.0±0.5×10^{-6} @1073K	[64]	<1
	n	1.0	5.0±0.5×10^{-6} @1073K	[64]	
PbTe-PbS/PbTe-PbS	*p*	2.3	21.4±0.3×10^{-6} @773K	[65]	<1
	n	1.5	21.4±0.3×10^{-6} @773K	[65]	

A couple of TE materials used to fabricate a thermoelectric module are summarized above. The α_L of each material were investigated from different literature and also different temperature. However, the percentage of linear thermal expansion coefficient difference ($\%\Delta\alpha_L$) between *p*-type and *n*-type are calculated in Table 1.2. As can be seen, the $\%\Delta\alpha_L$ between the different material types of *p*-type and *n*-type legs in the thermoelectric module is acknowledged by ≥18%. On the other hand, the $\%\Delta\alpha_L$ between the same material type of *p*-type and *n*-type (Si/Si and PbTe/PbTe) is observed less than 1%. In this case, *p*-type NbFeSb and *n*-type $Nb_{0.85}CoSb$ are different types of material. The $\%\Delta\alpha_L$ of NbFeSb/$Nb_{0.85}CoSb$ is acceptable if it is smaller than the data in Table 1.2. It is expected that NbFeSb/$Nb_{0.85}CoSb$ HH TE material is an excellent couple for the fabrication of a TE module. This point will be addressed in more detail in Chapter III.

1.5 Half-Heusler (HH) as a promising thermoelectric material with 18 VEC

Half-Heusler alloys are named by Friedrich Heusler, a German mining engineer and chemist who studied $MnCu_2Sn$ in 1903. The half-Heusler crystal structure is closely related to the Full-Heusler (FH) structure, except it has a 1:1:1 ratio of elements rather than 1:2:1. HH compounds have a general formula of *XYZ*, where *X* and *Y* are transition metals, and *Z* is the main group element. HH compounds take the form of the cubic crystal structure of MgAgAs-type, space group $F\bar{4}3m$ (No. 216), as shown in Figure 1.6a. The *Z* atom is located at (0,0,0), the *Y* atom at (¼, ¼, ¼), and the *X* atom at (½, ½, ½). The fourth face-centered-cubic (fcc) sublattice located at (¾, ¾, ¾) remains vacant. The FH structure can be made by simply filling the vacant sublattice with *Y* atoms, forming a composition of XY_2Z. Where the two sublattices, Y and Y2, are symmetrically equivalent [66], as shown in Figure 1.6b.

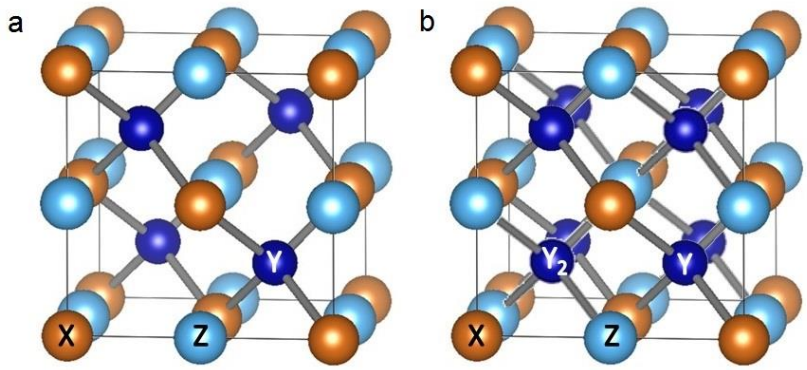

Figure 1.6 (a) The crystal structure of half-Heusler and (b) full-Heusler alloys. Half-Heusler alloys have composition XYZ, whereas in the full-Heusler structure, the vacancies are filled in with a second atom (Y2-site), making the composition XY_2Z.

Half-Heusler compounds can be thought of as comprising an X^{n+} ion stuffing a zine blende YZ^{n-} sublattice where the number of valence electrons associated with YZ^{n-} are 18 ($d^{10} + s^2 + p^6$). It has been demonstrated that the half-Heusler compounds with 18 valence electrons per unit cell exhibit large *S* values because of the existence of a narrow gap and sharp slope in the density of states around the Fermi level. [67-69] The electrical *p*-type or *n*-type HH compound can be controlled by adjusting the number of VEC. The Fermi level will lie up to the conduction band for *n*-type, while the Fermi level lies down to the valence band for *p*-type.

In various half-Heusler compounds, *M*NiSn and *M*CoSb (*M* = Ti, Zr, Hf) have been recognized as *n*- and *p*-type TE materials, respectively. Although the maximum *zT* values of the *n*-type *M*NiSn are nearly unity, those of the *p*-type *M*CoSb are still low to be around 0.5. [70-72] Recently, Fu et al. reported the highest *zT* of 1.5 at 1200 K for the *p*-type FeNbSb-based half-Heusler compounds. [73] Then *n*- and *p*-type HH compounds become a promising TE candidate with $zT > 1$. Furthermore, one of the effective ways to enhance the thermoelectric properties of these compounds is the substitution technique. The ability to substitute any of these three sublattices opens the door for a wide variety of compounds to be synthesized. Various atomic substitutions are employed to reduce thermal conductivity and enhance electrical conductivity. This property can be determined by band structure.

In the band structure, one of the most critical parameters is the density of state (DOS) effective mass (m_d^*). For metals or degenerate semiconductors (parabolic band and energy-independent scattering approximation). A large m_d^* means a large Seebeck coefficient. A large m_d^* can be achieved by either a high band degeneracy (N_V) or a heavy single band effective mass m_d^* because of $m_d^* = N_V^{2/3} m_d^*$. As mention above, HH compound crystallizes in a cubic structure with space group $F\bar{4}3m$. The high symmetry of a simple HH structure usually leads to a high band degeneracy. Figure 1.7a) shows the calculated band structure of NbFeSb is a narrow indirect-band-gap semiconductor. The conduction band minimum(CBM) of NbFeSb is located at point *X* with a band degeneracy of $N_V = 6$. In contrast, the valence band maximum (VBM) is located at point *L* with twofold orbital degeneracy. The high band degeneracy of the valence band makes NbFeSb more promising as a *p*-type TE material. Moreover, W. Li et al. revealed that Nb-site plays a vital role in optimizing band structure, leading to an improvement of the thermoelectric performance [74].

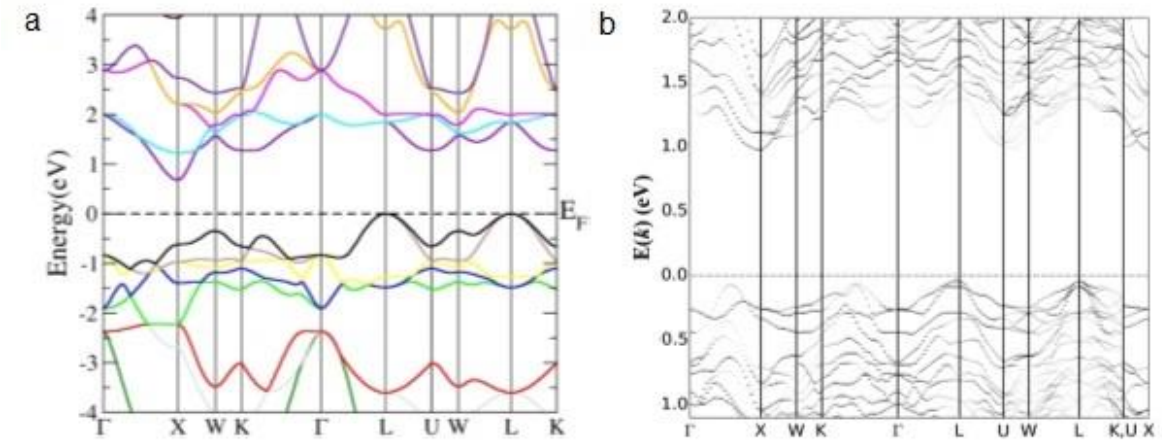

Figure 1.7 Calculated band structure of a) FeNbSb and b) $Nb_{0.8}CoSb$.

Additionally, several 19 VEC compounds such as NbCoSb have been found to be stable and exhibit thermoelectric properties as good as other HH family. This material is more effective with Nb vacancies with a nominal composition Nb_yCoSb. A large number of Nb vacancies reduce the overall electron count and stabilizing the material. Density functional theory predicts the 18-electron $Nb_{0.8}CoSb$ to be the stable composition for this compound, and excess electrons beyond 18 electrons provide heavy doping needed to improve the thermoelectric properties. However, any changes in the composition will act as dopants [75-77]. The Fermi level of the vacancy free is located deep in the conduction band corresponding to heavily doped *n*-type behavior, $Nb_{0.8}CoSb$ is a precise valence semiconductor [77], as shown in Figure 1.7b). Thus Nb_yCoSb with Nb vacancies sit is an interested candidate for *n*-type of Nb-based half-Heusler compound. The crystal structure of $Nb_{0.8}CoSb$ is shown in Figure 1.8.

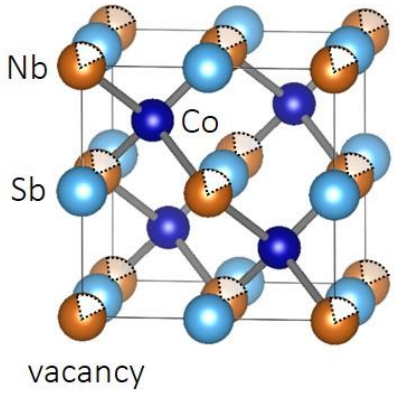

Figure 1.8 The crystal structure of *n*-type $Nb_{0.8}CoSb$ half-Heusler compound with Nb vacancies.

As mentioned above, *p*-type NbFeSb and *n*-type Nb_yCoSb are Niobium-based half-Heusler compounds, which becomes a good candidate for thermoelectric materials, owing to its excellent thermoelectric properties. However, thermal stability, such as high-temperature stability, thermal expansion, and other thermomechanical properties, are very limited in this research filed. Nevertheless, this characteristic is worth investigating for the fabrication of a thermoelectric module.

1.6 Purpose of dissertation

Further to the previous discussion, enhancing the thermoelectric module performance still a significant challenge for practical application. To achieve this point, explored the appropriate material is needed. Suitability as thermoelectric material is not only determined by a high *zT*. Other properties that make up a usable material are just as important. These include good mechanical properties and high-temperature stability, as well as the compatibility and the non-toxicity of the elements contained. Half-Heusler compounds (18 VEC) have the potential to be a promising thermoelectric candidate because of its excellent electrical property. On the other hand, the thermomechanical property of these materials is limited. Especially, the thermomechanical properties and high-temperature stability of HH materials have never been reported. However, HH compound plays an interesting role in the fabricated TE module for many years. Several TE modules made from HH compound both *p*-type and *n*-type leg with a different class of half-Heusler compound. Thus this study is the first report on the Nb-based (NbFeSb/$Nb_{0.85}$CoSb) HH thermoelectric module. Therefore, the performance of *n*- and *p*-type HH material, mechanical, thermal stability, and conversion efficiency of HH module have been precisely investigated.

In Chapter 2, the enhancement of *zT* for *p*-type NbFeSb HH compound through substitution technique is proposed using the combined method of arc-melting and spark plasma sintering to form $Nb_{0.9}M_{0.1}$FeSb (*M*= Ti, Zr, Hf) compounds. It is expected that NbFeSb shows outstanding high-temperature stability with maximized *zT* as well as a smaller $\%\Delta\alpha_L$ value than the literature review (Table 1.2). TE properties and thermomechanical properties are performed in the temperature range of 300 – 1073 K, which related to the operating temperature of this material. Furthermore, traditional *p*-type ZrCoSb has performed thermal stability compared with *p*-type NbFeSb. It is confirmed that NbFeSb exhibits more stable as well as higher *zT*.

In Chapter 3, $Nb_{0.85}$CoSb has the potential to be an *n*-type HH leg for assembling an Nb-based module. Here, $Nb_{0.85}$CoSb is selected, be it the Nb-based HH compound as well as an 18 VEC. This HH material would significantly reduce κ_{lat}. Besides the substitution effect, the Nb vacancies occur via minimizing the number of Nb atom in the unit cell to control the VEC number (similar to *p*-type NbFeSb-based). $Nb_{0.75}M_{0.1}$CoSb is substituted by 10% of Ti, Zr, and Hf at Nb-site. Also, the TE performance enhancement of $Nb_{0.75}M_{0.1}$CoSb (*M* = Ti, Zr, and Hf) is

investigated under the condition relevant to the previous chapter. It is intended that the obtained *n*-type are enhanced and matched with *p*-type in the previous chapter, in the viewpoint of TE properties and thermal stability.

In Chapter 4, the best *p*-type and *n*-type Nb-based HH compounds from Chapters II and III are created as *2π*-module by multiphysics modeling in the COMSOL program to simulate the conversion efficiency and power output of the *2π*-module. The compatibility of *p*-type and *n*-type provide that the Nb-based HH couple is an alternative to fabrication a module for practical application. Finally, Chapter 4 concludes all the results in this thesis. It is expected that the TE module based on *p*-type NbFeSb and *n*-type $Nb_{0.85}CoSb$ would be developed the efficiency and high-temperature stability of the module. The critical knowledge point in this dissertation would play an essential role in practical application.

In this dissertation, the concept for developing the Nb-based TE module performance is shown in Figure 1.9.

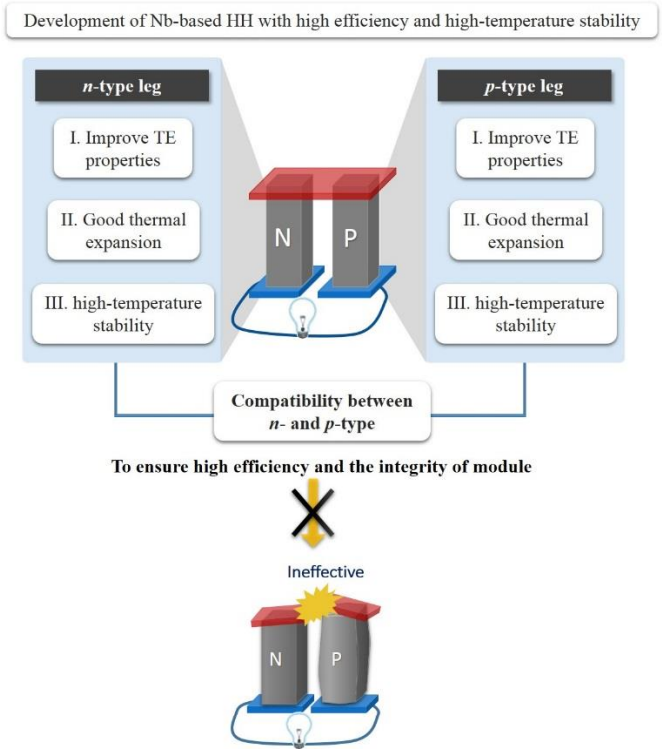

Figure 1.9 The concept for developing conversion efficiency of Nb-based HH TE module, are studied in this thesis.

1.7 Reference

[1] BP Statistical review of world energy 2019, London, 2019.

[2] Global energy and CO_2 status report, *International Energy Agency*, 2018.

[3] J. S. Sawyer, Man-made carbon dioxide and the "Greenhouse" effect, *Nature*, 239, 23-26 (1972).

[4] J. M. Murphy et al., UK climate projections science report: climate change projections, *Met Office Hadley Centre*, Exeter, UK, 2009.

[5] E. J. Chaisson, Long-term global heating from energy usage, 89, 28 (2008).

[6] A. J. Armstrong and Dr. J. Hamrin, *The renewable energy policy manual*, U. S. Export Council for Renewable Energy, October 2000.

[7] J. Twidell and T. Weir, *Renewable energy resources*, Taylor & Francis, 2006.

[8] Waste heat recovery: technology and opportunities in U.S. industry, BCS, Incorporated, March 2008.

[9] New technologies wasted energies, CNRS News, retrieved, July 2018.

[10] Goldstick, R., Principles of Waste Heat Recovery, Atlanta, GA: The Fairmont Press, Inc., 1986.

[11] G. J. Snyder and E. S. Toberer, *Nature*, 7, 105-114 (2008).

[12] G. S. Nolas, D. T. Morelli, and T. M. Tritt, *Annual Review of Materials Science* 29, 89 (1999).

[13] R. P. Hermann, R. Jin, W. Schweika, F. Grandjean, D. Mandrus, B. C. Sales, and G. J. Long, *Physical Review Letters* 90, 135505 (2003).

[14] J. Yang and F. Stabler, *Journal of Electronic Materials* 38, 1245 (2009).

[15] F. J. Disalvo, Thermoelectric cooling and power generation, *Science*, 285, 703-706 (1999).

[16] B. Abeles, *Physical Review*, 131, 1906 (1963).

[17] Rowe, D. M., *Renewable Energy*, 16, 1251-1256 (1999).

[18] J. Xin, Y. Tang, Y. Liu, X. Zhao, H. Pan and T. Zhu, *npj Quantum Mater.*, 3, 9 (2018).

[19] Y. Pei, X. Shi, A. LaLonde, H. Wang, L. Chen and G. J. Snyder, *Nature*, 473, 66-69 (2011).

[20] C. Fu, T. Zhu, Y. Liu, H. Xie and X. Zhao, *Energy Environ. Sci.*, 8, 216-220 (2015).

[21] H. Xie, H. Wang, Y. Pei, C. Fu, X. Liu, G. J. Snyder, X. Zhao and T. Zhu, *Adv. Funct. Mater.*, 23, 5123-5130 (2013).

[22] M. S. Dresselhaus, G. Chen, M. Y. Tang, R. Yang, H. Lee, D. Wang, Z. Ren, J-P. Fleurial and P. Gogna, *Adv. Mater.*, 19, 1043-1053 (2007).

[23] K. Biswas, J. He, I. D. Blum, C. I. Wu, T. P. Hogan, D. N. Seidman, V. P. Dravid and M. G. Kanatzidis, *Nature*, 489, 414-418 (2012).

[24] B. C. Sales, D. Mandrus and R. K. Williams, *Science*, 272, 1325-1328 (1996).

[25] C. Uher, in Thermoelectric Materials Research I (ed. T. Tritt) 139-253 (Semiconductors and Semimetals Series 69, Elsevier, 2011).

[26] G. S. Nolas, J. Poon and M. Kauzlarich, *Mater. Res. Soc. Bull*. 31, 199 (2006).

[27] S. M. Kauzlarich, S. R. Brown and G. J. Snyder, *Dalton trans*., 2099 (2007).

[28] G. Joshi, R. He, M. Engber, G. Samsonidze, T. Pantha, E. Dahal, K. Dahal, J. Yang, Y. Lan, B. Kozinsky and Z. Re, *Energ. Environ. Sci.*, 7, 4070-4076 (2014).

[29] C. Fu, S. Bai, Y. Liu, Y. Tang, L. Chen, X. Zhao and T. Zhu, *Nat. Commun*., 6, 8144 (2015).

[30] W. G. Zeier, J. Schmitt, G. Hautier, U. Aydemir, Z. M. Gibbs, C. Felser and G. J. Snyder, *Nat. Rev. Mat*., 1, 16032 (2016).

[31] W. Li, G. Yang and J. Zhang, *J. Phys. D*, 49, 195601 (2016).

[32] T. Zhu, C. Fu, H. Xie, Y. Liu and X. Zhao, *Adv. Energy Mater.*, 5, 1500588 (2015).

[33] K. Xia, Y. Liu, S. Anand, G. J. Snyder, J. Xin, J. Yu, X. Zhao and T. Zhu, *Adv. Funct. Mater.*, 28, 1705845 (2018).

[34] W. Silpawilawan, K. Kurosaki, Y. Ohishi, H. Muta and S. Yamanaka, *J. Mater. Chem. C*, 5, 6677-6681 (2017).

[35] W. Silpawilawan, Y. Ohishi, H. Muta, S. Yamanaka and K. Kurosaki, *Mater. Trans.*, 59, 1030-1034 (2018).

[36] J. Shen, Z. Wang, J. Chu, S. Bai, X. Zhao, L. Chen and T. Zhu, *ACS Appl. Mater. Interfaces*, 11, 14182-14190 (2019).

[37] F. J. DiSalvo, *Science*, 285, 703 (1999).

[38] J. F. Li, W. S. Liu, L. D. Zhao, *NPG Asia Mater.* 2, 152–158 (2010).

[39] D. M. Rowe and C. M. Bhandari, Modern Thermoelectrics, Holt, Rinehart and Winston, London, 1983.

[40] G. Jeffrey Snyder and Eric S. Toberer, *Nature Materials*, 7, 105-114 (2008).

[41] J. M. Ziman, Principles of the Theory of Solids, Cambridge University Press, Cambridge, 1972.

[42] Neil W. Ashcroft and N. David Mermin, Solid State Physics, Holt, Rinehart and Winston, 1976.

[43] R. Smith, J. Janak and C. Adler, Electronic Conduction in Solids, McGraw-Hill, 1967.

[44] J. S. Dugdale and D. K. MacDonald. *Phys. Rev.* 98, 1751 (1955).

[45] A. J. Minnich, M. S. Dresselhaus, Z. F. Ren and G. Chen, *Energy Environ. Sci.* 2, 466 (2009).

[46] S. K. Bux, R. G. Blair, P. K. Gogna, H. Lee, G. Chen, M. S. Dresselhaus, R. B. Kaner and J. P. Fleurial, *Adv. Funct. Mater.* 19, 2445 (2009).

[47] J. D. Chung and A. J. H. McGaughey, *J. Heat Trans.* 126, 376 (2004).

[48] P. G. Klemens, *Proceedings of the Physical Society. Section A* 68, 1113 (1955).

[49] J. Callaway and H. C. von Baeyer, *Physical Review* 120, 1149 (1960).

[50] Z. Xu, H. Wu, T. Zhu, C. Fu, X. Liu, L. Hu, J. He, and X. Zhao, *NPG Asia Materials*, 8, e302 (2016).

[51] S. Leblanc, S. K. Yee, M. L. Scullin, C. Dames, and K. E. Goodson, *Renew. Sustainable Energy Rev*., 32, 313 (2014).

[52] G. Schierning, R. Chavez, R. Schmechel, B. Balke, G. Rogl, and P. Rogl, *Transl. Mater. Res*., 2, 025001 (2015).

[53] R.E. Taylor, CINDAS Data Series on Materials Properties, Thermal Expansion of Solids, 1–4, ASM International (1998).

[54] G. Rogl, A. Grytsiv, M. Gurth, A. Tavassoli, C. Ebner, A. Wunschek, S. Puchegger, V. Soprunyuk, W. Schranz, E. Bauer, H. Muller, M. Zehetbauer, P. Rogl, *Acta Materialia*, 107, 178-195 (2016).

[55] D. Jung, K. Kurosaki, C. Kim, H. Muta, and S. Yamanaka, *Journal of Alloys and Compounds*, 489, 328-331 (2010).

[56] I. Engstrom and B. Lonnberg, *Journal of applied Physics*, 63, 4476 (1988).

[57] M. Sondergaard, M. Christensen, K. A. Borup, H. Yin, B. B. Iversen, *Journal of Electronic Materials*, 42, 1417-1421 (2013).

[58] P. Guo, X. Huang, X. Zhu, Z. Lu, Y. Zhou, L. Li, Z. Li, B. Wei, Y. Zhang, W. Su., *Fuel Cells*, 13, 666-672 (2013).

[59] Z. Grades, Nanostructure materials and their application in thermoelectric energy harvesting, 2018.

[60] Liu, H., Shi, X., Xu, F. *et al.* Copper ion liquid-like thermoelectrics. *Nature Mater* 11, 422–425 (2012).

[61] M. Gu, S. Bai, X. Xia, X. Huang, X. Li, X. Shi, and L. Chen, *Appl. Sci.*, 7, 952 (2017).

[62] L. M. Pavlova, Yu. I. Shtern, R. E. Mironov, High temperature, 49, 369-379 (2011).

[63] T. S. Rohr and G. Hawkins, *Optics Express*, 23, 580-596 (2015).

[64] Silicon germanium thermoelectric materials and module development program, Harrison, New Jersey, 1969.

[65] J. E. Ni, E. D. Case, R. D. Schmidt, C. I. Wu, T. P. Hogan, R. M. Trejo, M. J. Kirkham, E. Lara-Curzio, and M. Kanatzidis, *Journal of Materials Science*, 48, 6233-6244 (2013).

[66] F. Casper, T. Graf, S. Chadov, B. Balke, and C Felser, *Semicond. Sci. Technol*., 27, 063001 (2012).

[67] C. Fu, T. Zhu, Y. Liu, H. Xie and X. Zhao, *Energy Environ. Sci.,* 8, 216 (2015).

[68] C. Fu, T. Zhu, Y. Pei, H. Xie, H. Wang, G. J. Snyder, Y. Liu, Y. Liu and X. Zhao, *Adv. Energy Mate.*, 4, 1400600 (2014).

[69] Hsin Lin, L. Andrew Wray, Yuqi Xia, Suyang Xu, Shuang Jia, Robert J. Cava, Arun Bansil & M. Zahid Hasan, *Nat. Mater.*, 9, 546 (2010).

[70] T. Sekimoto, K. Kurosaki, H. Muta and S. Yamanaka, *Jpn. J. Appl. Phys.*, 46, L673 (2007).

[71] T. Sekimoto, K. Kurosaki, H. Muta and S. Yamanaka, *Mater. Trans.*, 46, 1481-1484 (2005).

[72] Y. Xia, S. Bhattacharya, B. Ponnambalam, A. L. Pope, S. J. Poon, and T.M. Tritt, *J. Appl. Phys.*, 88, 1952 (2000).

[73] C. Fu, S. Bai, Y. Liu, Y. Tang, L. Chen, X. Zhao, T. Zhu, *Nat. Commun.*, 6, 8144 (2015).

[74] W. Li, G. Yang, and J. Zhang, *J. Phys. D: Appl. Phys*., 49, 195601 (2016).

[75] W. G. Zeier, S. Anand, L. Huang, R. He, H. Zhang, Z. Ren, C. M. Wolverton, and G. J. Snyder, *Chemistry of Materials*, 29, 1210-1217 (2017).

[76] K. Xia, Y. Liu, S. Anand, G. Jeffrey Snyder, J. Xin, J. Yu, X. Zhao, and T. Zhu, *Advanced Functional Materials*, 28, 1705845 (2018).

[77] K. Xia, P. Nan, S. Tan, Y. Wang, B. Ge, W. Zhang, S. Anand, X. Zhao, G. Jeffrey Snyder, and T. Zhu, *Energy and Environmental Science*, 12, 1568 (2019).

Chapter II

Thermoelectric and Thermomechanical Properties of *p*-type NbFeSb HH Compound

2.1 Introduction

Due to half-Heusler compounds crystallize in the cubic MgAgAs-type structure with the space group $F\bar{4}3m$ (No. 216). [1] It has been demonstrated that the half-Heusler compounds with 18 valence electrons per unit cell exhibit large *S* values because of the existence of a narrow gap and sharp slope in the density of states around the Fermi level. [1-4] On the other hand, this material still has a large thermal conductivity. The challenge in the chapter is discovering the best *p*-type which exhibits more stable at high-temperature and improving TE properties by suppressing κ_{lat} via substitution. Moreover, reports on the effect of substitute elements on the TE properties and thermomechanical properties of *p*-type NbFeSb is very limited [5,6].

In this chapter, there are two objectives 1) To confirm that NbFeSb system exhibit not only high *zT* but also high-temperature stability than other famous *p*-type ZrCoSb system, 2) To improve TE properties of NbFeSb by substitute 10% of Ti, Zr, Hf at Nb-site. It is expected that the appropriate *p*-type HH compound demonstrates not only high *zT* but also excellent thermal stability. To understand the advantage of the substitution effect, the TE properties, mechanical properties, and thermal stability are investigated.

2.2 Experimental Details

The experimental section in this chapter is carried out in our lab at Osaka University. In this thesis study, bulk samples of half-Heusler ternary compounds are prepared by arc-melting (AM), followed spark plasma sintering (SPS) technique. For the as-sinter sample, the microstructural via X-ray powder diffraction (XRD) analysis. Crystallographic characterizations scanning electron microscopy (FE-SEM) with Energy Dispersive X-ray spectrometry (EDX) are evaluated at room temperature. The thermoelectric properties are evaluated thought Laser flash (LF), Hall effects, and ZEM-3 method from 300 K to 1073 K. The linear thermal expansion coefficient is measured by a dilatometer (Bruker AXS) and calculated by lattice expansion from high-temperature XRD patterns. The physical properties are derived from the sound velocities via an ultrasonic pulse-echo method at room temperature. The detail is explained in this chapter.

2.2.1 Synthesis of *p*-type NbFeSb Half-Heusler Compounds

In chapter II, there are two sets of *p*-type samples. First, the nominal composition of undoped NbFeSb and ZrCoSb are studied in 2.3.1. Second, the nominal composition of Nb1-x*M*xFeSb (*M*=Ti, Zr, Hf) with x = 0.1 are studied in 2.3.2 and 2.3.3. Ingots are synthesized by arc-malting under an Ar atmosphere. Nb (chunk, 99.9%), Co (shot, 99.97%), Sb (shot, 99.999%), Ti (stick, 99.9%), Zr (chunk, 99.9%), and Hf (chunk, 99.9%) are used as the starting materials. The melting processes are performed in a furnace which is evacuated to the low pressure of 5×10^{-3} MPa and, following by filling with high-purity Ar (5N) of 0.04 MPa. A small amount of pure Zr was put in the chamber to eliminate remaining oxygen in the side (see Figure 2.1). All ingots are flipped and re-melted at least six times to homogenize the alloys during the arc melting process.

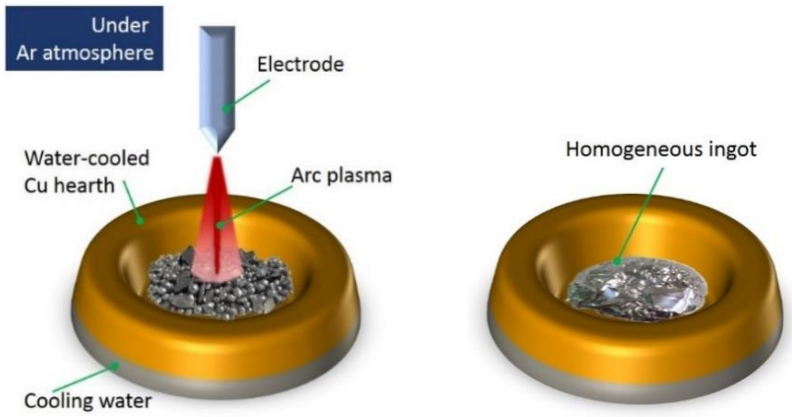

Figure 2.1 Schematic of arc-melting (AM) process.

The obtained ingots are crushed into powders, then loaded into a graphite die and between graphite punches for subsequently compacted into polycrystalline bulk samples using the spark plasma sintering (SPS) technique (see Figure 2.2). The powder sample is sintered under 50 MPa pressure in a flowing Ar atmosphere at 1123 K, 50 minutes for the NbFeSb sample, and 1323 K, 5 minutes for the ZrCoSb sample. An undoped NbFeSb and ZrCoSb samples are prepared using the same method for high-temperature stability comparison. The density (*d*) of as-sintered samples is evaluated from the measured weight and dimensions.

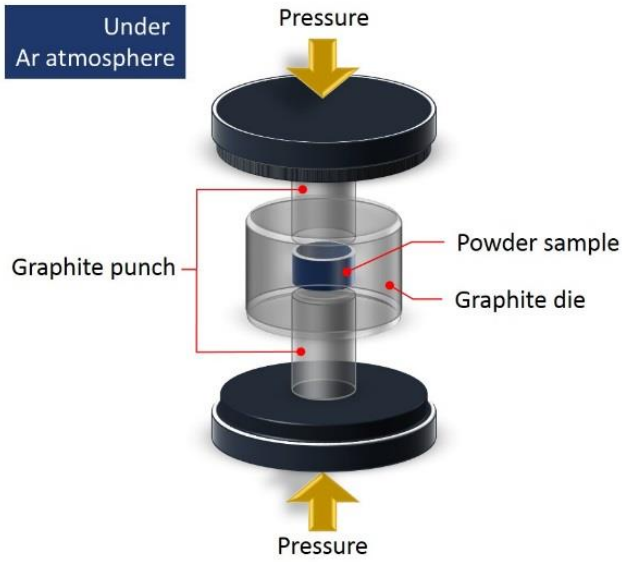

Figure 2.2 Schematic of Spark Plasma Sintering (SPS) method

2.2.2 Phase Analysis and Microstructure Observation

The crystal structure is investigated by powder X-ray diffraction (XRD) analysis. The data are collected on a diffractometer on Rigaku Ultima IV with Cu Kα radiation (λ_0 = 1.5406 Å) in air at 300 K. The microstructure of the SPS samples is investigated by scanning electron microscopy (SEM). The chemical composition is analyzed by energy dispersive X-ray (EDX) spectroscopy, which the detector resolution is 138 eV. The standard deviation of the obtained average compositions is within ±2%.

2.2.3 Electrical and Thermal Transport Measurements

σ and S are measured using a commercial apparatus (ZEM-3, ADVANCE RIKO, Inc.) under a reduced He atmosphere from 300 - 1073 K. The accuracy is ±3%. The Hall carrier concentration (n_H) and Hall mobility (μ_H) are calculated by $n_H = 1/eR_H$ and $\mu_H = \sigma R_H$, where e is the elementary charge and R_H is the Hall coefficient. R_H is measured by van de Pauw method in a vacuum under applied magnetic field (0.5 T) using a commercial apparatus (Resitest8300, TOYO Corporation) at 300 K. The estimated error of Hall coefficient is within ±5%. κ is calculated from heat capacity (C_p), thermal diffusivity (α), and d using the relationship $\kappa = \alpha C_p d$. α is measured from 300 - 1073 K using a flash diffusivity apparatus (LFA-457, NETZSCH) with a standard deviation of ±3%. C_p is estimated by the model of Dulong and Petit, i.e., $C_p = 3nR$, where n is the number of atoms per formula unit, and R is the gas constant.

2.2.4 High-temperature Stability and Linear Thermal Expansion Measurement

High-temperature stability is measured by using high-temperature XRD (HT-XRD) on Ultima IV (Rigaku) with Cu $K\alpha$ radiation. The HT-XRD patterns for the powder samples are collected from 300 - 1073 K in both a He atmosphere and in air. The α_L is calculated using the changed lattice parameter (a) values, evaluated from HT XRD patterns changed as the temperature increased in a He atmosphere. Studying lattice expansion under a He atmosphere provides high resistance to oxidation and unabsorbed the X-rays. during the heating process.

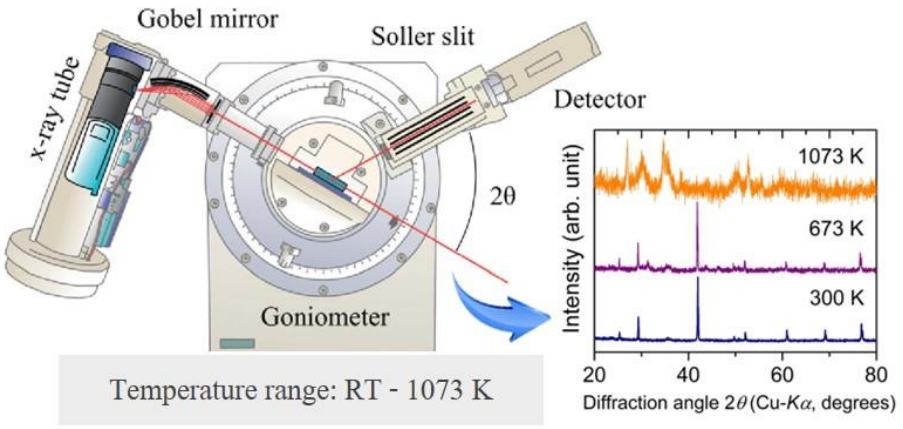

Figure 2.3 Schematic of high temperature XRD (HT-XRD) method.

Thermal expansion is measured using a push-rod dilatometer (TD5000SA, Bruker AXS) from 300 - 1073 K in an Ar atmosphere. The dilatometer is a thermo-analytical technique for determining dimensional of materials changes during heating or cooling. For the analysis, as shown in Figure 2.4, the specimen and alumina reference is placed directly against the push-rod. The sample length change based on the temperature setting transmits the change values to the linear variable displacement transducer. The alumina reference sample corrects the measurement. The coefficient of thermal expansion (α_L) is determined by Equation 2.1.

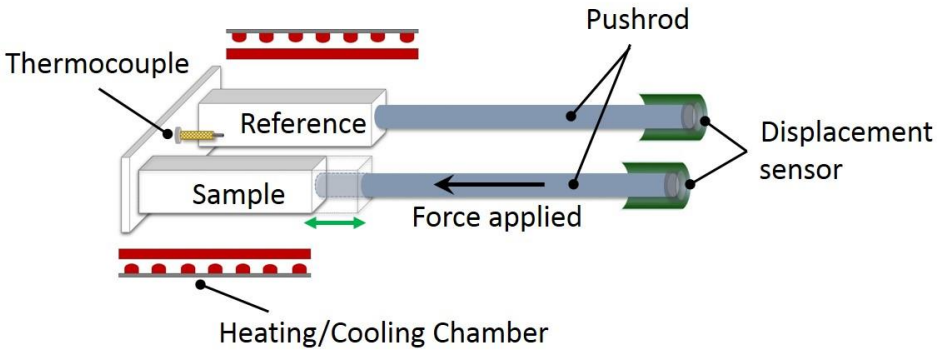

Figure 2.4 Schematic of Dilatometer method

$$\alpha_L = \frac{1}{L_{RT}} \frac{L(T) - L_{RT}}{T - T_{RT}} \quad (2.1)$$

Where L_{RT} is the sample's length at room temperature.

In this study, the rectangular-shaped samples were cut from the SPS samples and used for the dilatometer measurement. To perform a dilatometric analysis, a sample is inserted into one side of the holder; the other side is a reference sample (Al_2O_3), within a movable furnace. Pushrods are positioned directly against the sample and transmit the length change to a linear variable displacement transducer. The data are obtained in terms of thermal expansion curves, the average value of the linear thermal expansion coefficient (α_L) in the temperature range from T_{RT} (=300) to T (= 1073 K) is calculated.

Mechanical property is obtained by sound velocity in solid. The longitudinal (v_L) and shear sound velocities (v_S) were measured by an ultrasonic pulse-echo method at room temperature in the air using a 5 MHz longitudinal and shear sound wave echogenic transducer (Figure 2.5). The relative accuracy of each velocity is around ±5%.

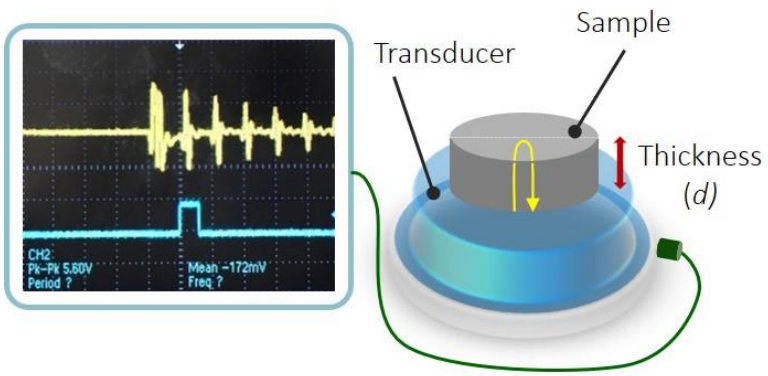

Figure 2.5 Schematic of an ultrasonic pulse-echo method.

The Debye temperature (θ_D), and bulk modulus (B) were calculated from the sound velocities as a followed equation:

$$v_L = \frac{2L}{t_2 - t_1} \tag{2.2}$$

$$v_S = \left[\left(\frac{t_3 - t_2}{D} \right)^{1/2} + \left(\frac{t_2 - t_1}{2L} \right)^{1/2} \right]^{-1/2} \tag{2.3}$$

$$E = \frac{G(3v_L^2 - 4v_S^2)}{(v_L^2 - v_S^2)} \tag{2.4}$$

$$B = \left(v_L^2 - \frac{4}{3} v_S^2 \right) d, \tag{2.5}$$

$$\theta_D = \left(\frac{h}{k_B} \right) \left(\frac{3nN_A d}{4\pi M} \right)^{1/3} v_m, \tag{2.6}$$

where h is the Plank constant, k_B is the Boltzmann constant, n is the number of atoms per molecule, N_A is Avogadro's number, M is molar weight, and v_m is average sound velocity described as equation below.

$$v_m = \left[\frac{1}{3} \left(\frac{2}{v_S^3} + \frac{1}{v_L^3} \right) \right]^{-1/3}, \tag{2.7}$$

On the other hand, the Grüneisen parameter (γ) can be written as follows:

$$\gamma = \frac{3\alpha_L BV}{C_V} \tag{2.8}$$

Where, V is the molar volume and C_V is the heat capacity and estimated as 74.83 $Jmol^{-1}K^{-1}$ using Dulong-Petit model.

2.3 Results and Discussion

2.3.1 Thermal stability of NbFeSb versus ZrCoSb

ZrCoSb-based has been the best *p*-type in the HH family until NbFeSb-based was studied and exhibit excellent TE properties. However, another property relevant to the performance of TE material has not been reported. Therefore, in this thesis, I need to explore which one is more suitable at the high-temperature range and can be compared with the best *n*-type in nowadays. Herein I comprehensively evaluated the elastic modulus, thermal expansion, and high-temperature stability of undoped NbFeSb and ZrCoSb bulk samples in the temperature range from 300 – 1073 K.

Figure 2.6 shows the powder XRD patterns of the SPS bulk samples, together with the literature data. [7,8] The samples are identified as the half-Heusler phase with no impurity phases. The lattice parameter of the half-Heusler phase calculated from the XRD patterns and the density of the SPS bulk samples are summarized in Table 2.1. The lattice parameters of both NbFeSb and ZrCoSb obtained in the present study are well consistent with the literature data. The bulk samples had high densities enough for measurements of the thermal conductivity and thermomechanical properties.

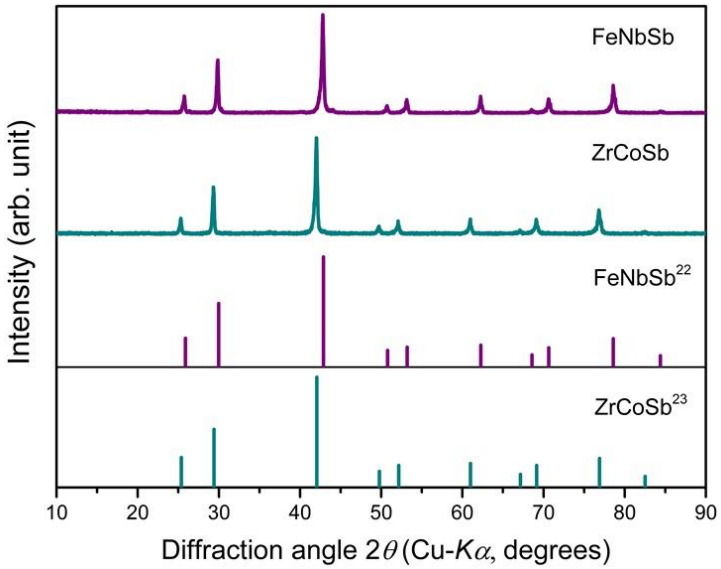

Figure 2.6 Powder XRD patterns of the SPS bulk samples of NbFeSb and ZrCoSb.

Table 2.1 Lattice parameter of the half-Heusler phase and density of the SPS bulk samples of NbFeSb and ZrCoSb.

Compound	***a* (nm)**	**Density (g cm^{-3})**		**Relative density**
		Theoretical	**Experimental**	**(%T.D.)**
NbFeSb	0.5956(3) 0.5958 [7]	8.49	8.46	99
ZrCoSb	0.6074(3) 0.6069 [8]	8.08	7.75	96

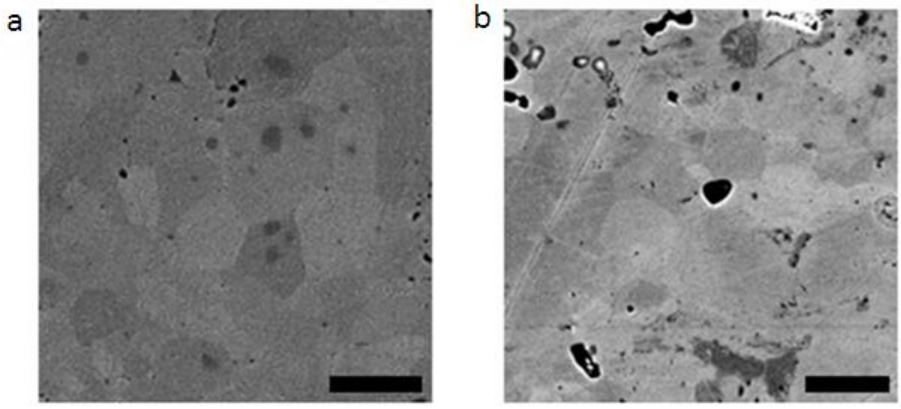

Figure 2.7 SEM images of the SPS bulk samples of (a) NbFeSb and (b) ZrCoSb. Scale bars in (a) and (b) are 5 μm and 15 μm, respectively.

Figure 2.7 shows the SEM images of the SPS bulk samples. It is confirmed that both samples of NbFeSb and ZrCoSb had no remarkable cracks, although small pores existed in the ZrCoSb sample. From the images, the average grain sizes are determined as around 3 μm and 10 μm for NbFeSb and ZrCoSb, respectively.

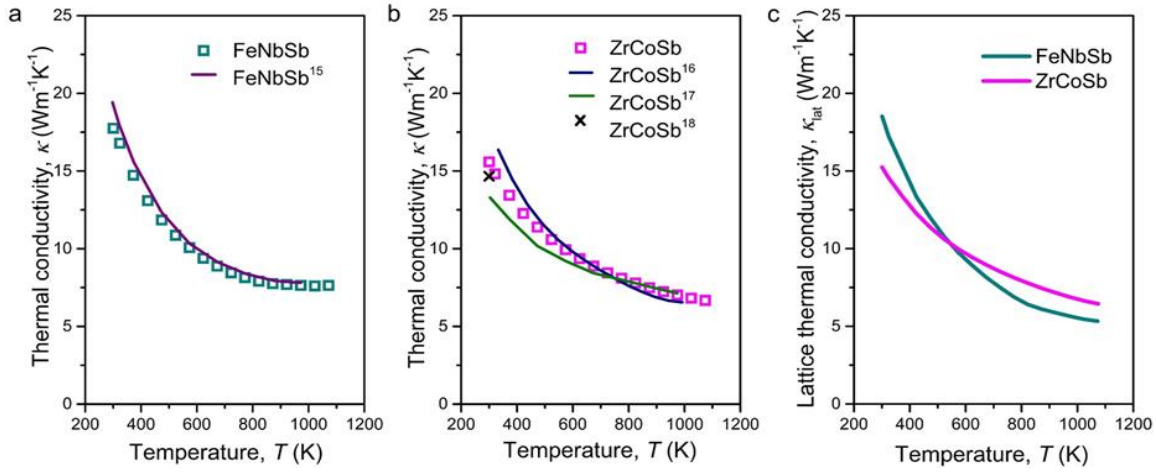

Figure 2.8 Temperature dependence of the thermal conductivity (κ) of the SPS bulk samples of (a) NbFeSb and (b) ZrCoSb. (c) Temperature dependence of the calculated lattice thermal conductivity (κ_{lat}) of the samples.

Figure 2.8a and 2.8b show the temperature dependences of the κ of the SPS bulk samples of NbFeSb and ZrCoSb, respectively, in which the literature data [9-12] are shown for comparison. The κ values obtained in the present study are well consistent with the literature data. The κ of both samples decreased with increasing temperature roughly proportional to T^{-1}, meaning that the phonon contribution is predominant. Figure 2.8c shows the κ_{lat} of the samples. It is confirmed that NbFeSb exhibited lower κ_{lat} at high temperatures than that of ZrCoSb, meaning that NbFeSb is more suitable than ZrCoSb as TE materials for high temperature application. This lower κ_{lat} of NbFeSb than that of ZrCoSb at high temperatures would be due to the effective phonon-phonon scattering occurred in NbFeSb. As summarized in Table 2.3, NbFeSb exhibits higher Grüneisen parameter (γ) than that of ZrCoSb, leading to high anharmonicity and low κ_{lat} at high temperatures.

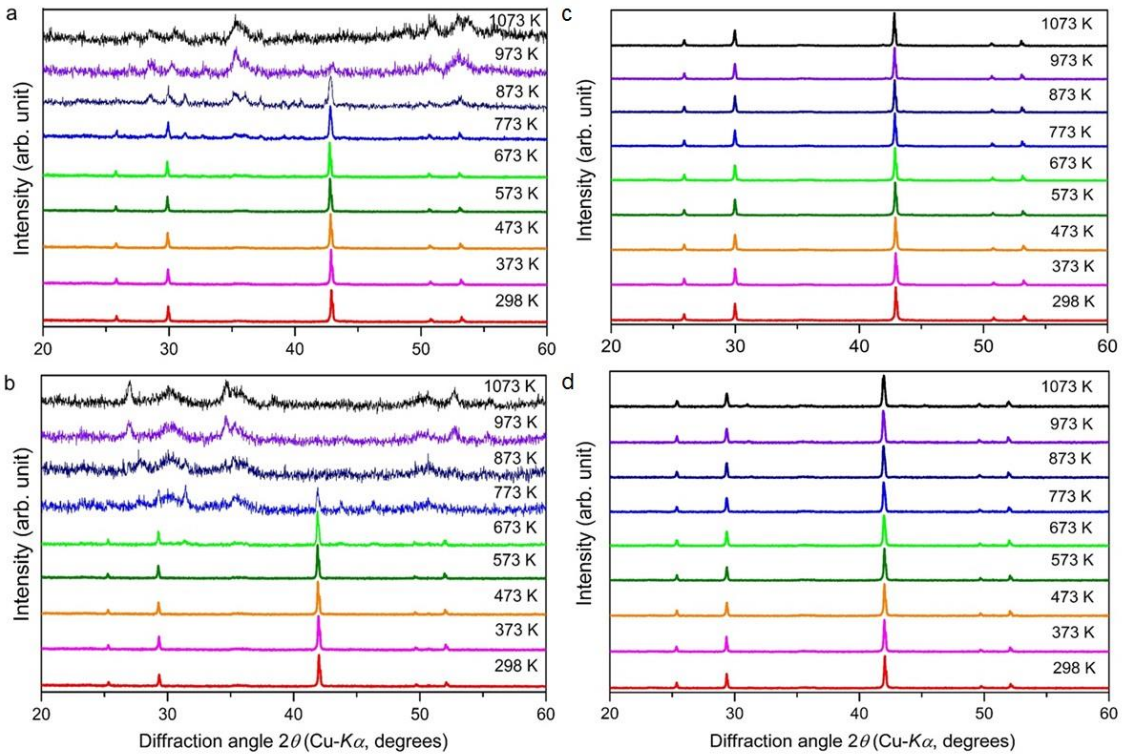

Figure 2.9 HT-XRD patterns of a) NbFeSb and b) ZrCoSb collected in air. c) NbFeSb and d) ZrCoSb collected in a He atmosphere.

Figure 2.9a and 2.9b shows the HT-XRD patterns of NbFeSb and ZrCoSb collected in air, in the temperature range from room temperature to 1073 K. The XRD patterns changed significantly at high temperatures for both samples. At 773 K, the half-Heusler phase is confirmed in NbFeSb, while not confirmed in ZrCoSb. These HT-XRD results indicate that NbFeSb is more stable at high temperatures than ZrCoSb not only in an inert atmosphere but also in air.

Figure 2.9c and 2.9d show the HT-XRD patterns of NbFeSb and ZrCoSb collected in a He atmosphere, in the temperature range from room temperature to 1073 K. The peaks are mostly the same but shifted to lower angle with increasing temperatures in both of them. However, a few peaks for impurities are observed above 873 K in ZrCoSb, while the phase structure of NbFeSb did not change at high temperatures. The lattice parameters at high temperatures are calculated

from the HT-XRD patterns for both samples, and the data are plotted as a function of temperature (Figure 2.10).

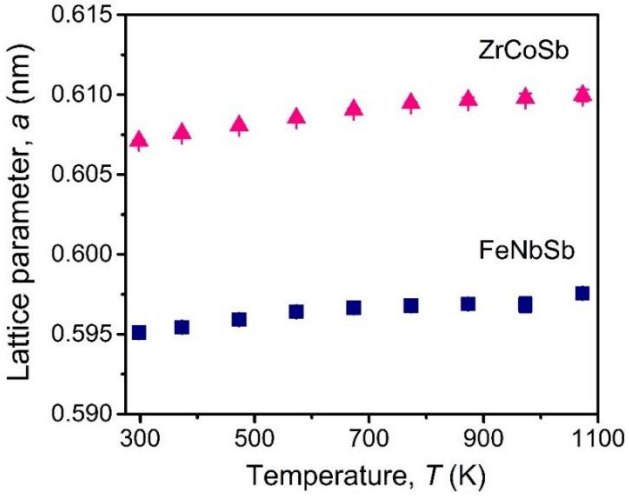

Figure 2.10 Temperature dependence of the lattice parameters of NbFeSb and ZrCoSb. The lattice parameters were calculated from the HT-XRD patterns collected in a He atmosphere.

In addition to the HT-XRD measurements, we also performed the dilatometer measurement to check the validity for the thermal expansion data. The average α_L values determined by the HT-XRD and dilatometer measurement are summarized in Table 2.2.

Table 2.2 Linear thermal expansion coefficient (α_L) of NbFeSb and ZrCoSb obtained by the HT-XRD and dilatometer measurements. The errors of the α_L determined by the HT-XRD analysis were evaluated from the errors of the lattice parameters. On the other hand, the uncertainty in the dilatometer measurement is below 10%.

Compound	**Type**	**Average α_L ($\times 10^{-6}$ K^{-1}) ,300-1073 K**	
		HT-XRD	**Dilatometer**
NbFeSb	*p*	8.0	9.0
ZrCoSb	*p*	7.5	8.8 (8.916)
TiNiSn [13]	*n*	10.5	-
ZrNiSn [13]	*n*	11.0	-
HfNiSn [13]	*n*	9.6	-

Table 2.2 summarizes the average values of the α_L for NbFeSb and ZrCoSb determined by the HT-XRD and dilatometer measurements. The α_L value of ZrCoSb determined by the dilatometer measurement is well consistent with the literature value [16]. The values obtained from the dilatometer measurement are higher than those obtained from the HT-XRD. Although the reason of this difference is still unclear, the same tendency has been observed in the *n*-type half-Heusler compounds, *M*NiSn (*M* = Ti, Zr, Hf) [13]. It was confirmed that the α_L values of NbFeSb are slightly higher than those of ZrCoSb. Note that here, the α_L values of *n*-type *M*NiSn are larger than those of both NbFeSb and ZrCoSb; the values determined by the HT-XRD analysis of TiNiSn, ZrNiSn, and HfNiSn are 10.5, 11.0, 9.6×10^{-6} K^{-1}, respectively [13]. In fabricating TE devices, similar values (or small percentage) of the α_L should be required for *n*-type and *p*-type materials to reduce the thermal stress arising across the temperature gradient. Therefore, from the viewpoint of thermal expansion, it can be said that NbFeSb has better compatibility with *n*-type *M*NiSn than ZrCoSb.

Table 2.3 Physical properties of the SPS bulk samples of NbFeSb and ZrCoSb obtained by the sound velocity measurements. In calculating the Grüneisen parameter (γ), the α_L values obtained by the HT-XRD measurement were used. The uncertainty in the sound velocity measurement is 2% and 7% for NbFeSb and ZrCoSb, respectively.

Mechanical properties	**NbFeSb**	**ZrCoSb**
Longitudinal sound velocity, v_L (ms^{-1})	4751	5545
Shear sound velocity, v_S (ms^{-1})	2750	3123
Average sound velocity, v_m (ms^{-1})	3052	3474
Bulk modulus, B (GPa)	146	128 (135 [10])
Debye temperature, θ_D (K)	352	376 (392 [10])
Grüneisen parameter, γ	1.49	1.44

Table 2.3 summarizes the physical properties of the SPS bulk samples of FeNbSb and ZrCoSb. The literature values of bulk modulus (B) and θ_D for ZrCoSb [10]. are shown for comparison. For the isotropic materials, the B and θ_D can be written in terms of the longitudinal (v_L) and shear sound velocities (v_S) by Equation 2.2 - 2.7 [14]. On the other hand, the Grüneisen parameter (γ) can be calculated by Equation 2.8 [15].

In summary of this part, fine bulk-samples are obtained by an arc-melting followed by spark plasma sintering. NbFeSb exhibited lower Debye temperature and higher Grüneisen parameter than those of ZrCoSb. High-temperature XRD analyses revealed that NbFeSb is more stable at high temperatures than ZrCoSb in both an inert gas atmosphere and in air. Furthermore, NbFeSb had closer thermal expansion coefficient with those of *n*-type *M*NiSn (*M* = Ti, Zr, Hf) half Heusler compounds than ZrCoSb. It can be concluded that NbFeSb is more suitable for *p*-type half-Heusler TE materials than ZrCoSb from the viewpoint of not only the TE properties but also the thermomechanical properties and high-temperature stability. Therefore, NbFeSb is selected to be a suitable *p*-type. In the next part of this chapter, NbFeSb system is enhanced TE properties through substitution technique.

2.3.2 Improving the TE properties of NbFeSb through substitution technique

Up to now, the most successful aspect of suppression lattice thermal conductivity is substitution and nanostructuring. In this Chapter, I also studied both strategies. The first strategy is the substitution technique. Substituent elements act as point defect scattering, which can be scatted phonon transport and lead to reduce lattice thermal conductivity term. Strong point defect scattering would be enhanced by larger atomic mass and radius, as described by following equation [16,17].

$$\Gamma_M = \frac{\sum_{i=1}^{n} c_i \left(\frac{\overline{M_i}}{\overline{M}} \right)^2 f_i^1 f_i^2 \left(\frac{M_i^1 - M_i^2}{M_i} \right)^2}{\sum_{i=1}^{n} c_i} \tag{2.9}$$

$$\Gamma_S = \frac{\sum c_i \left(\frac{\overline{M_i}}{\overline{M}} \right)^2 f_i^1 f_i^2 \varepsilon_i \left(\frac{r_i^1 - r_i^2}{r_i} \right)^2}{\sum_{i=1}^{n} c_i} \tag{2.10}$$

Where Γ_M and Γ_S are mass and strain field fluctuation scattering parameter.

In this study, Ti, Zr, and Hf are selected as the substituent element for NbFeSb, and investigate the effect of the substitution on the TE properties of NbFeSb. The substitution ratio is fixed to be 0.1 for all the system, i.e., the nominal composition of the samples is set as $Nb_{0.9}M_{0.1}FeSb$ (M = Ti, Zr, Hf). Polycrystalline bulk samples are synthesized and their high temperature TE properties are examined. The powder samples are sintered at 1157 K, 30 minutes for holding time, and under 65 MPa pressure in a flowing Ar atmosphere. The result of substitution technique is shown in this topic while the consequence of nanostructuring is shown in 2.3.3.

The substituent element in this study is substituted at Nb-site because substitution at Nb-site has more impact on TE properties in HH compound compared with another site in system, as can be confirmed by Figure 2.11.

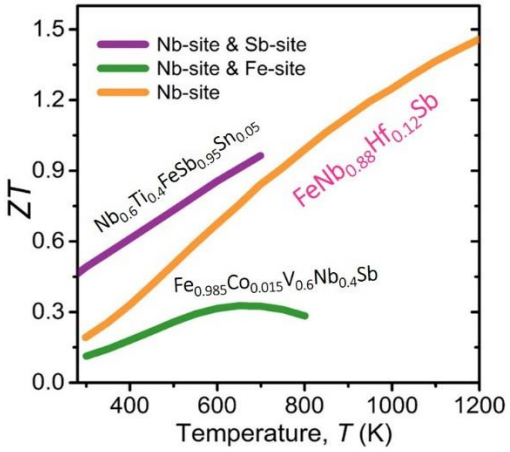

Figure 2.11 Temperature dependence of the *ZT* with different substitution sites of *p*-type HH thermoelectric materials.

The powder XRD patterns of the SPS bulk samples of $Nb_{0.9}M_{0.1}FeSb$ (*M* = Ti, Zr, Hf) are shown in Fig. 2.12. The sample of $Nb_{0.9}Ti_{0.1}FeSb$ is HH single phase with no remarkable secondary phases. On the other hand, the samples of $Nb_{0.9}Zr_{0.1}FeSb$ and $FeNb_{0.9}Hf_{0.1}Sb$ contain small amounts of secondary phases of Fe_2Nb, SbFe, and $Fe_{0.7}Hf_{0.3}$.

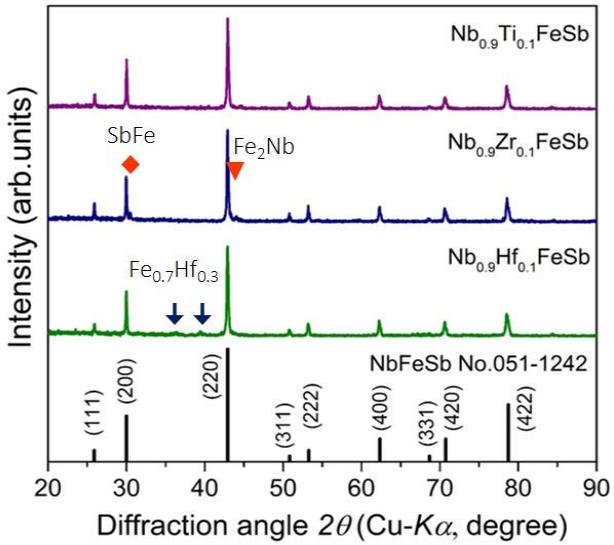

Figure 2.12 Powder X-ray diffraction patterns of the SPS bulk samples of $Nb_{0.9}M_{0.1}FeSb$ (*M* = Ti, Zr, Hf).

Actual composition determined by EDX, lattice parameter of the HH phase, and density of the SPS bulk samples of $Nb_{0.9}M_{0.1}FeSb$ (M = Ti, Zr, Hf) are summarized in Tables 2.4, 2.5, and 2.6, respectively. In all samples, the actual compositions especially the Fe and Nb contents are different from the nominal ones. There are 2 possible reasons of this composition difference; (1) evaporation of Sb during the synthesis process and (2) unreacting of Fe and/or Nb with Sb to form the HH phase due to the large difference in the melting points. In case of the Hf-doped system, the phenomenon (1) would be predominant, which results in the higher Nb content than the nominal one. On the other hand, in cases of the Zr- and Ti-doped systems, the phenomenon (2) would be predominant, which results in the lower Fe and Nb contents than the nominal ones. In order to understand the phase state more certainly, the Fe-Nb-Sb ternary phase diagram needs to be developed. The lattice parameters of the Zr- and Hf-substituted samples are similar but higher than that of the Ti-substituted sample, which can be explained by the difference of atomic radii of each element. All samples have high relative density, above 95% of the theoretical density.

Table 2.4 Comparison between our data and literature data on the zT_{max} and samples' characteristics for Ti-doped NbFeSb.

Samples' characteristics	**Literature data** [18]	**This work**
zT_{max}	~0.77	~0.7
Nominal composition	$Nb_{0.9}Ti_{0.12}FeSb$	$Nb_{0.9}Ti_{0.1}FeSb$
Actual composition of the HH phase	$Nb_{0.86}Ti_{0.11}$ $Fe_{1.02}Sb_{1.01}$	$Nb_{0.80}Ti_{0.12}$ $Fe_{0.84}Sb_{1.00}$
Hf/Nb ratio of the HH phase	0.13	0.15
Secondary phase	None	None
Relative density (%T.D.)	~97	96.0
Lattice parameter of the HH phase (nm)	0.5944	0.5951 (3)

Table 2.5 Comparison between our data and literature data on the zT_{max} and samples' characteristics for Zr-doped NbFeSb.

Samples' characteristics	**Literature data** [19]	**This work**
zT_{max}	~0.8	~0.4
Nominal composition	$Nb_{0.9}Zr_{0.1}FeSb$	$Nb_{0.9}Zr_{0.1}FeSb$
Actual composition of the HH phase	$Nb_{0.90}Zr_{0.10}$ $Fe_{1.01}Sb_{0.99}$	$Nb_{0.78}Zr_{0.13}$ $Fe_{0.88}Sb_{1.00}$
Hf/Nb ratio of the HH phase	0.11	0.17
Secondary phase	None	SbFe, Fe_2Nb
Relative density (%T.D.)	~95	95.3
Lattice parameter of the HH phase (nm)	0.5961	0.5962 (18)

Table 2.6 Comparison between our data and literature data on the zT_{max} and samples' characteristics for Hf-doped NbFeSb.

Samples' characteristics	**Literature data** [19]	**This work**
zT_{max}	~1.5	~0.4
Nominal composition	$Nb_{0.9}Hf_{0.1}FeSb$	$Nb_{0.9}Hf_{0.1}FeSb$
Actual composition of the HH phase	$Nb_{0.90}$ $Hf_{0.09}$ $Fe_{1.01}Sb_{1.00}$	$Nb_{1.10}$ $Hf_{0.16}$ $Fe_{0.89}Sb_{1.00}$
Hf/Nb ratio of the HH phase	0.10	0.15
Secondary phase	None	$Fe_{0.7}Hf_{0.3}$
Relative density (%T.D.)	~95	99.0
Lattice parameter of the HH phase (nm)	0.5965	0.5968 (12)

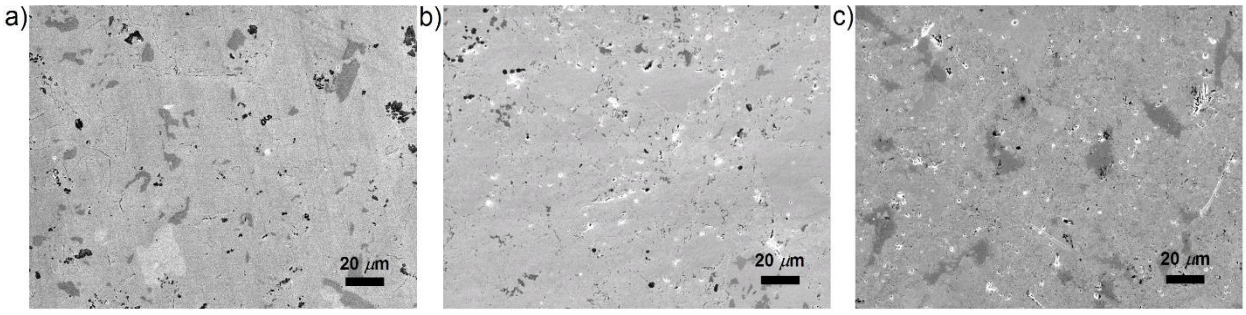

Figure 2.13 SEM images of the SPS bulk samples of (a) $Nb_{0.9}Ti_{0.1}FeSb$, (b) $Nb_{0.9}Zr_{0.1}FeSb$, and (c) $Nb_{0.9}Hf_{0.1}FeSb$.

The SEM images of the polished surface of the SPS bulk samples of $Nb_{0.9}M_{0.1}FeSb$ (M = Ti, Zr, Hf) are shown in Figure 2.13. It can be confirmed that all samples are dense with no remarkable cracks. The EDX point analysis revealed that the white inclusions observed in the SEM images of the Zr-substituted sample are an Sb-Fe alloy and an Fe-Nb alloy. On the other hand, the dark area observed in the Hf-substituted sample is determined as an Fe-Hf alloy. These results are well consistent with the results of the XRD analysis. Furthermore, it is also confirmed that the bright and dark area in Figure 2.13a correspond to the HH phase with the similar chemical composition with the matrix phase while some of the black spots are a Ti-rich phase and most of those are pores.

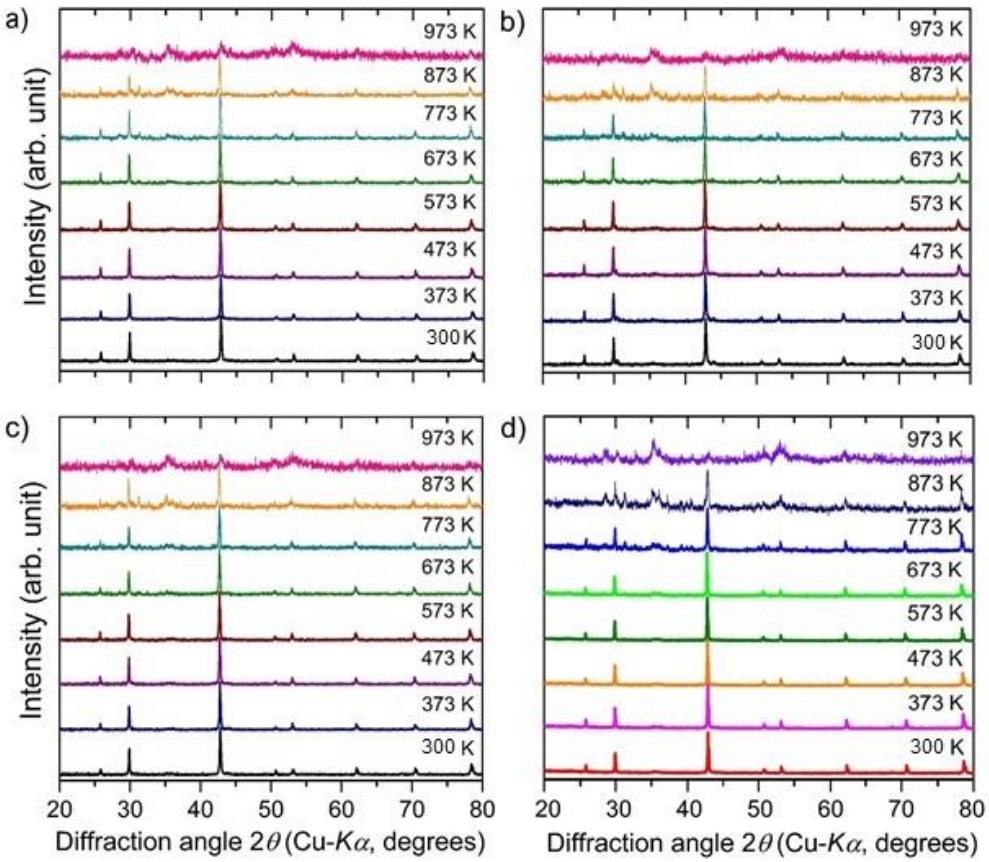

Figure 2.14 HT-XRD patterns of *p*-type HH compounds: a) $Nb_{0.9}Ti_{0.1}FeSb$, b) $Nb_{0.9}Zr_{0.1}FeSb$, c) $Nb_{0.9}Hf_{0.1}FeSb$, and d) non-doped NbFeSb collected in air.

HT-XRD patterns in Figure 2.14 indicated the thermal stability of HH compounds in air. All samples are stabled at high temperature (up to 773 K), which the main peak matches the HH phase. Above 773 K some peaks of HH phase disappear and some impurity phase occurred at higher temperature. Moreover, substituted samples are more stable than undoped one. On the other hand, HT-XRD patterns of all samples are stabled in every temperature range (300 – 1073 K) when evaluated in a He atmosphere as can be seen in Figure 2.15.

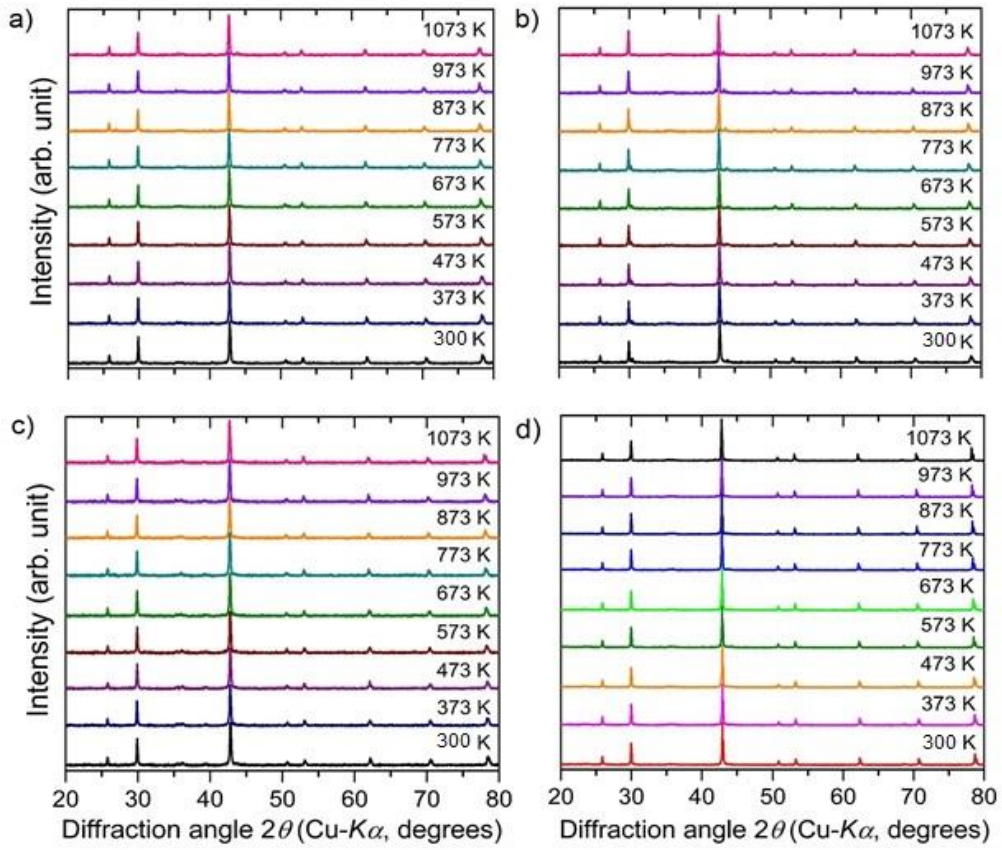

Figure 2.15 HT-XRD patterns of *p*-type HH compounds: a) $Nb_{0.9}Ti_{0.1}FeSb$, b) $Nb_{0.9}Zr_{0.1}FeSb$, c) $Nb_{0.9}Hf_{0.1}FeSb$, and d) non-doped NbFeSb collected in an inert atmosphere.

When the powder sample is kept under helium atmosphere no significant changes can be observed in a varying temperature. The XRD pattern remains a HH phase in all temperature. However, a drift of the peak positions toward lower diffraction angles with increased temperature is overlaid with the phase transformation in the contour plots. This is caused by a shift in the cell parameters caused by lattice expansion. This demonstrates an exceptionally high stability of *p*-type $Nb_{0.9}M_{0.1}FeSb$ (M= Ti, Zr, Hf) in both air and inert atmosphere.

Table 2.7 Physical properties of the SPS samples of *p*-type $Nb_{0.9}M_{0.1}FeSb$ (*M*= Ti, Zr, Hf) obtained from the sound velocity measurements.

Physical Properties	**$Nb_{0.9}Ti_{0.1}FeSb$**	**$Nb_{0.9}Zr_{0.1}FeSb$**	**$Nb_{0.9}Hf_{0.1}FeSb$**
Longitudinal velocity, v_L (ms^{-1})	4802	5242	5545
Transverse velocity, v_S (ms^{-1})	2799	3079	3064
Average sound velocity, v_m (ms^{-1})	3105	3413	3414
Young's modulus, *E* (GPa)	162	194	206
Bulk modulus, *B* (GPa)	105	123	157
Poisson ratio, ν	0.24	0.24	0.28
Debye temperature, θ_D (K)	334	351	388
Grüneisen parameter, γ	1.09	1.24	1.64

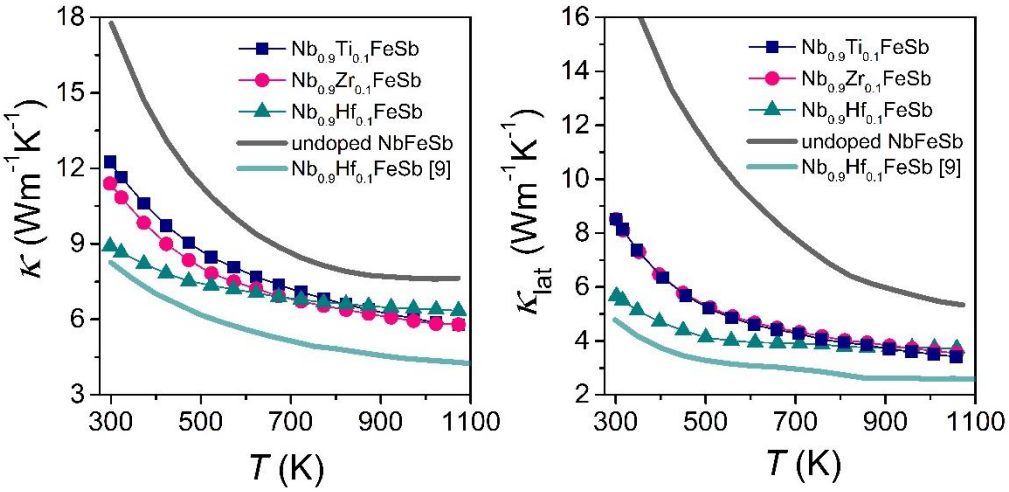

Figure 2.16 Temperature dependences of (a) total thermal conductivity (κ), and (b) lattice thermal conductivity (κ_{lat}) of the SPS bulk samples of $Nb_{0.9}M_{0.1}FeSb$ (*M* = Ti, Zr, Hf).

Figures 2.16a and 2.16b show the temperature dependences of κ and κ_{lat} of the SPS bulk samples of $Nb_{0.9}M_{0.1}FeSb$ (*M* = Ti, Zr, Hf), where the literature data for $Nb_{0.88}Hf_{0.12}FeSb$ which exhibits $zT = 1.5$ at 1200 K are shown for comparison. κ_{lat} is obtained by subtracting the electronic component (κ_{el}) from the κ, where κ_{el} is estimated via Wiedemann-Franz relationship, i.e., $\kappa_{el} = L\sigma T$ (*L* is the Lorenz number 2.44×10^{-8} $W\Omega K^{-2}$). As can be seen in Figure 2.16b, the Hf

substitution is very effective to reduce the κ_{lat} of NbFeSb compared with the Ti- and Zr-substitutions. This is because that the substitution by heavy element makes large mass fluctuation (equation 2.9) leading to effective scattering of heat carrying phonons. On the other hand, all samples exhibit similar κ_{lat} values above 800 K, which is because the phonon-phonon scattering is predominant at high temperatures, while the phonon-impurity scattering is predominant at low temperatures. The κ_{lat} values of our sample $Nb_{0.9}Hf_{0.1}FeSb$ are clearly higher than the literature data for $Nb_{0.88}Hf_{0.12}FeSb$ in spite of their similar chemical compositions. It is considered that the differences in the microstructure and actual composition would cause this κ_{lat} difference.

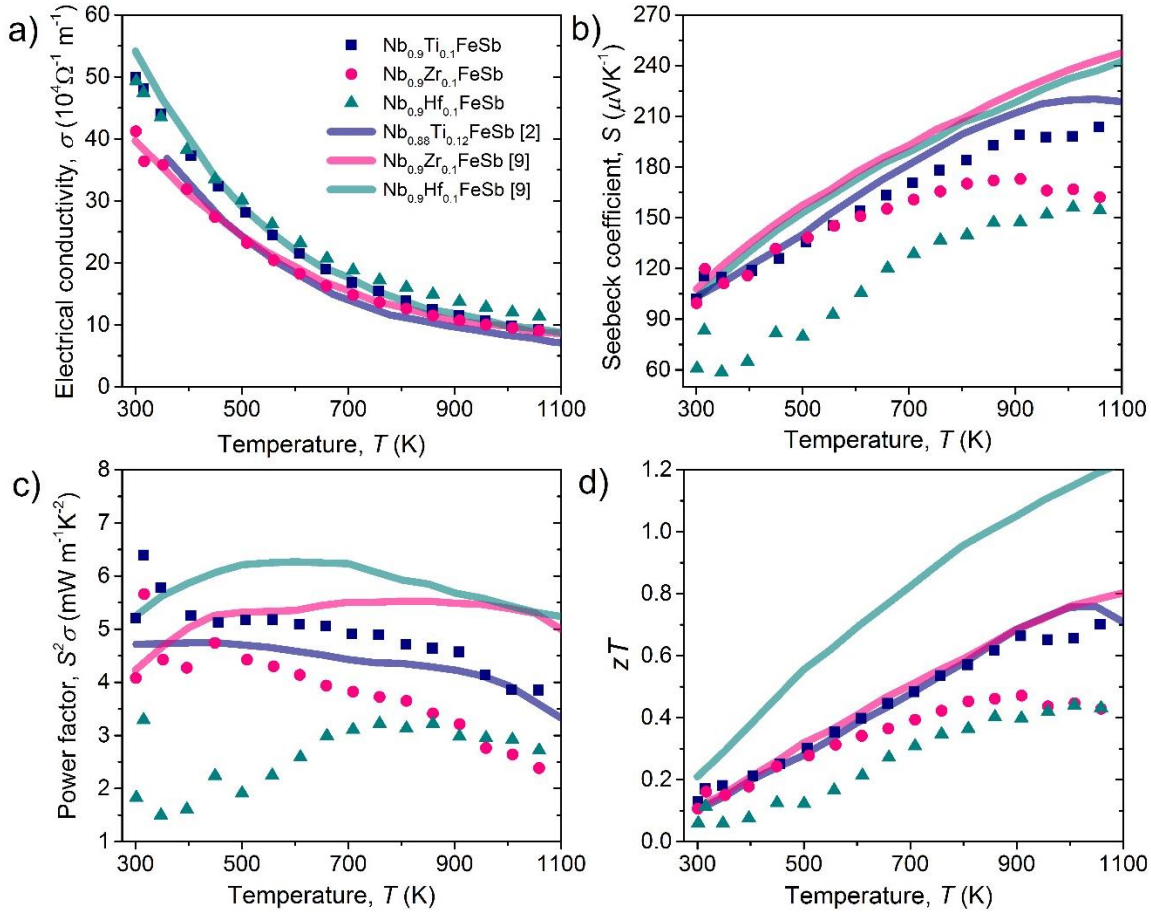

Figure 2.17 Temperature dependences of (a) electrical conductivity σ, (b) Seebeck coefficient S, (c)power factor ($S^2\sigma$), and (d) zT of our samples having the nominal compositions $Nb_{0.9}M_{0.1}FeSb$ (M = Ti, Zr, Hf), together with the literature data [16,17].

Temperature dependences of σ, S, $S^2\sigma$, and zT of the SPS bulk samples of $Nb_{0.9}M_{0.1}FeSb$ (M = Ti, Zr, Hf) samples are shown in Figs. 2.17a, 2.17b, 2.17c, and 2.17d, respectively. In these figures, the literature data [16,17] are shown for comparison. The σ values decrease while the S values increase with increasing temperature for all samples, showing metal-like behavior. The origin of the peaks observed in the temperature dependence of S is now unclear. The S values of the Ti- and Zr-substituted samples are very similar and clearly higher than those of the Hf-substituted sample, even though the nominal doping rate is the same for all samples. This can be explained from the actual composition of the HH phase summarized in Table 2.4, 2.5, and 2.6, i.e., the actual Nb/Ti and Nb/Zr ratio is almost the same but clearly different from that of Nb/Hf. On the other hand, the σ values of the Ti- and Hf-substituted samples are very similar and clearly higher than those of the Zr-substituted sample, which would be caused by both the actual composition of the HH phase and the amount of the secondary phases. As can be confirmed in Figure 2.12, the Ti-substituted sample has no remarkable secondary phases, which leads to high mobility compared with those of other samples containing some secondary phases and thereby high σ values as well as large S values are achieved in the Ti-substituted sample. As the results of σ and S, the Ti-substituted sample exhibits the best TE performance, the maximum $S^2\sigma$ and zT values are around 6 $mWm^{-1}K^{-2}$ at 350 K and 0.7 at 1073 K, respectively.

In the Hf- and Zr-doped systems, as can be confirmed in Figure 2.12 and Tables 2.5 and 2.6, our samples contain secondary phases $Fe_{0.7}Hf_{0.3}$, SbFe, and Fe_2Nb, which results in the difference between the nominal and the actual compositions. The samples reported in the literatures [17] have no such secondary phases and their actual compositions are similar with the nominal ones. The HH phases of our samples have larger M/Nb (M = Zr, Hf) ratio than the nominal ones, which leads to high doping ratio and thus small values of the Seebeck coefficient, as can be confirmed in Figure 2.15b. On the other hand, the secondary phases in our samples would scatter charge carriers, which leads to low carrier mobility. This low carrier mobility results in the similar values of the electrical conductivity between our data and the literature data (Figure 2.15a), even though our samples might have larger carrier concentration than those in the literatures. This composition difference and existing of the secondary phases would effect on the

low *zT* of our samples (Figure 2.15c). On the other hand, in the Ti-doped system, as can be confirmed in Figure 2.12 and Table 2.4, our samples contain no remarkable secondary phases and the Ti/Nb ratio is similar with the literature one [16]. As the results, our sample shows similar TE properties with the literature data [16]. Therefore, it can be concluded that synthesizing pure HH phase with optimized composition is important to obtain high *zT*.

2.3.3 Suppression κ_{lat} by introducing nanostructure

According to the previous experiment, the best nominal composition of the *p*-type half-Heusler compound is $Nb_{0.9}Ti_{0.1}FeSb$. In this part, I try to improve TE properties of HH compound by nanostructuring technique. Nanostructuring can suppress κ_{lat} because it can introduce the high density of grain boundaries, which increases more interface phonon scattering (Figure 2.18). The strategy of this work is the combination of substitution technique and nanostructuring technique. To synthesis nanostructure in HH compound, the rapid solidification of melt-spinning (MS) is used in this work.

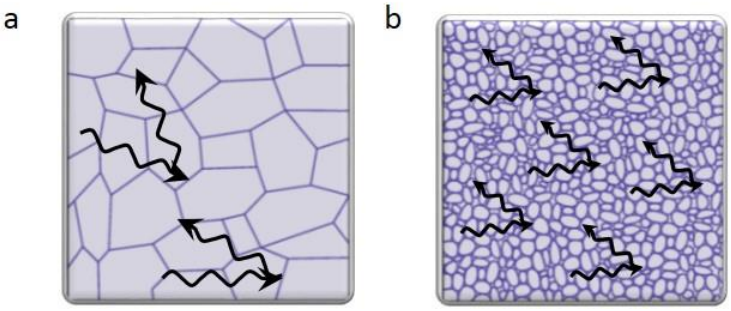

Figure 2.18 Schematic illustration of phonon scattering at the boundaries of the a) microscale grains and b) nanoscale grains in bulk material.

The starting material are mixed and placed in a boron-nitride crucible (BN crucible), and subsequently melted by heating from induction coil under an Ar atmospheric pressure of 0.2 MPa. The melted mixture is directly injected through a BN crucible with a nozzle diameter of 0.6 mm under pressure of 0.02 MPa onto a Cu wheel with two different speeds (2000 and 4000

rpm). When touching the surface wheel with different rotating speeds, a melt is rapidly solidified to thin ribbons with different structures. The obtained ribbons are named after the rotating speeds, i.e., MS-2000 and MS-4000, for the rotation speeds of the Cu wheel of 2000 and 4000, respectively. This technique called the Melt-spinning method or rapid solidification method (see Figure 2.19).

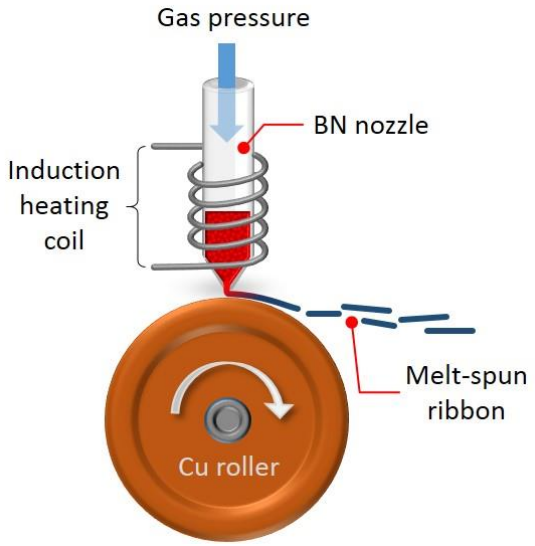

Figure 2.19 Diagram of Melt-spinning process.

The obtained ribbons are grounded into powders, pressed into a graphite die, and insert in an SPS furnace. During the SPS process in an Ar atmosphere, the maximum temperature, holding time, and maximum pressure are set to be 1153 K, 25 minutes, and 65 MPa. The bulk samples are named after SPS, i.e., MS-SPS (2000rpm) and MS-SPS (4000rpm). Then all samples are evaluated crystal structure, chemical composition, as well as electrical and thermal transport properties. The results are shown below.

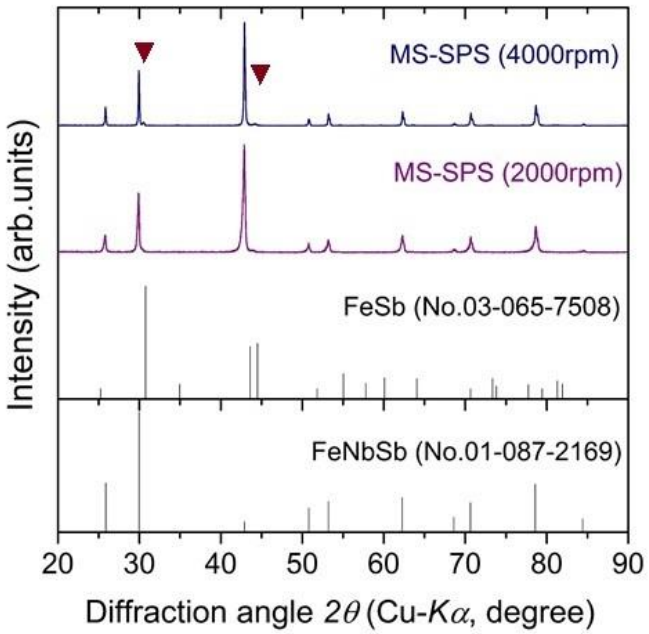

Figure 2.20 Powder XRD pattern of MS-SPS (2000rpm) and (4000rpm).

The powder XRD patterns of bulk MS-SPS samples of $Nb_{0.9}Ti_{0.1}FeSb$ are shown in Figure 2.20. All the peaks of the XRD patterns are identified as the half-Heusler phase. A small amount of impurities phase corresponds to the FeSb phase the has been observed in MS-SPS (4000rpm) sample. The lattice parameter, *a* of MS-SPS (2000rpm), and (4000rpm) are 5.953 Å and 5.956 Å, respectively.

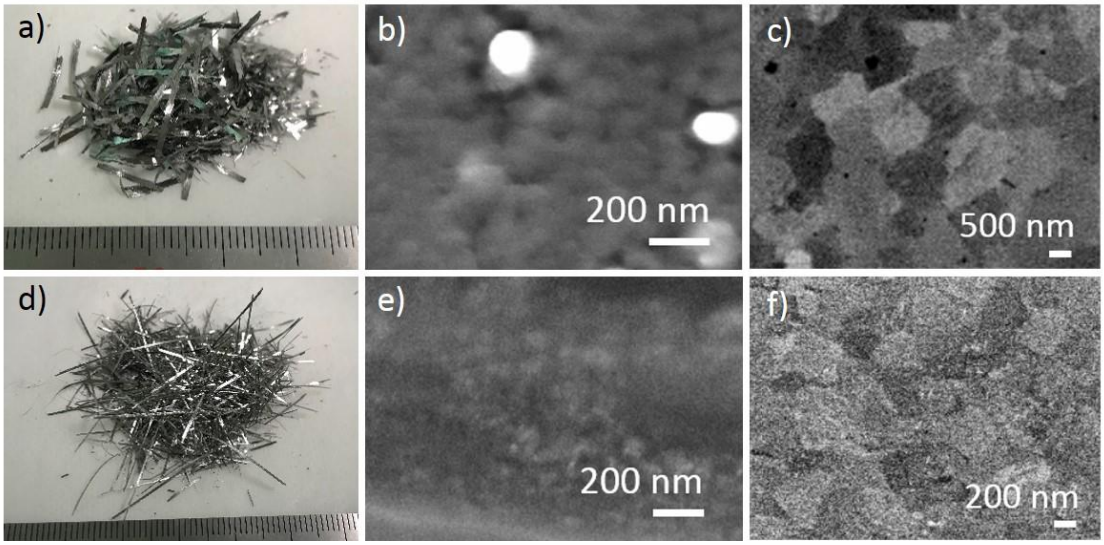

Figure 2.21 a) and d) appearance of melt-spun ribbon, b) and e) SEM images of melt-spun ribbon, c) and f) SEM images of MS-SPS bulk sample. (a,b,c) MS-2000 rpm and (d,e,f) MS-4000 rpm.

Figure 2.21 shows the appearance of the melt-spun ribbon and SEM images of melt-spun ribbon as well as MS-SPS bulk samples. The ribbon wide decreased from 1.058 mm to 0.385 mm with increasing roller speed, as shown in Figure 2.21a) and d). In the melt-spun ribbon, nano-scale particles dispersed uniformly are shown in Figure 2.21 b) and e). Moreover, the size of particles is smaller with faster the Cu wheel speed. For MS-SPS bulk samples, the grains are larger than the ribbon due to the grain growth during sintering. Nevertheless, the size of grains is in the nano-scale, as can be seen in Figure 2.21 c) and f). The estimated size of grains is 600 nm for MS-SPS (2000rpm) and 300 nm for MS-SPS (4000rpm).

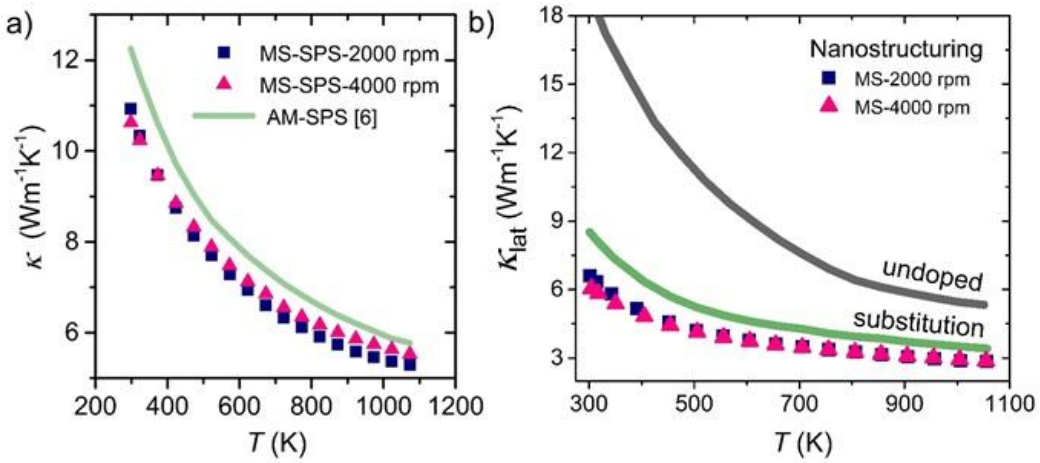

Figure 2.22 Temperature dependence of a) κ, b) κ_L of MS-SPS (2000rpm) and (4000rpm) compare with undoped and SPS sample.

The thermoelectric properties of MS-SPS (2000rpm) and MS-SPS (4000rpm) are evaluated. As can be seen in Figure 2.22, κ and κ_{lat} of $Nb_{0.9}Ti_{0.1}FeSb$ sample decreased with increasing temperature. The average κ_{lat} value of MS-SPS samples is 6 - 7 $Wm^{-1}K^{-1}$ at 300 K. It is clearly shown that the substitution technique significantly reduced κ_{lat}. Moreover, nanostructuring can be suppressed more phonon scattering in half-Heusler material compare with undoped one.

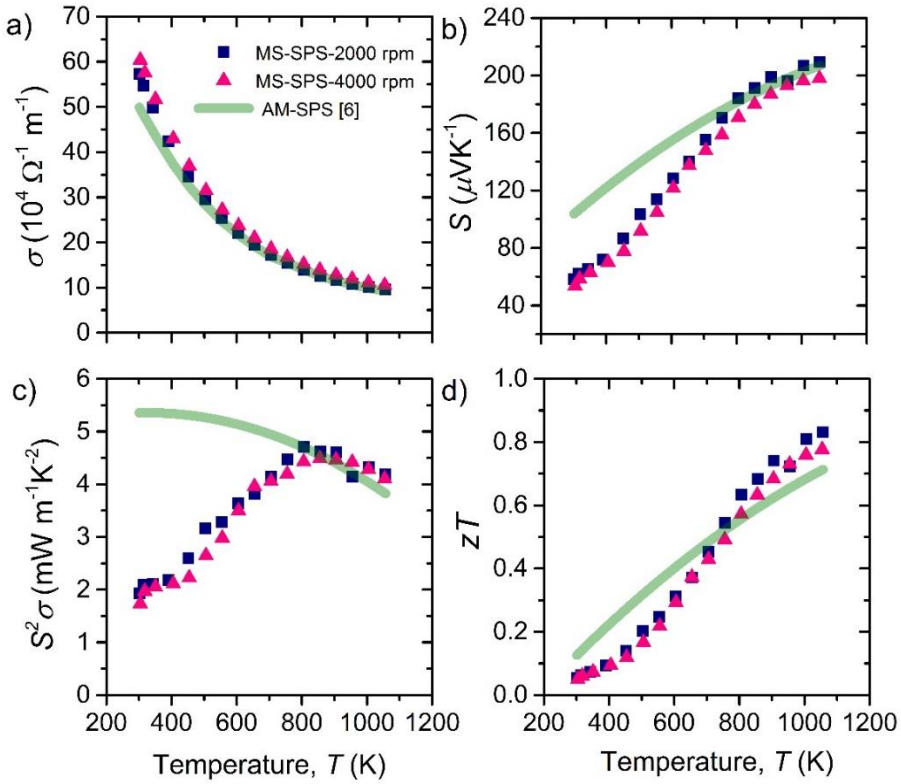

Figure 2.23 Temperature dependence of a) σ, b) S, c) $S^2\sigma$, d) zT for $Nb_{0.9}Ti_{0.1}FeSb$ MS-SPS bulk sample compared with SPS sample (green line).

The values of σ, S, $S^2\sigma$, and zT as a function of temperature can be seen in Figure 2.23. The σ of all samples indicated degenerate semiconductor behavior. σ of MS-SPS samples almost the same as SPS sample, which means MS-SPS samples suppressing the thermal transport without affecting the electrical one. Due to the increasing trends of the absolute S are positive at all temperatures, indicating p-type conductivity. The absolute S values of all MS-SPS bulk samples and SPS samples are not different at high temperatures. However, the extremely low κ_{lat} of MS-SPS samples lead to enhance zT of 0.8 at 1073 K.

2.4 Summary

The experiment in this Chapter reported the thermomechanical properties and high-temperature stability of *p*-type half-Heusler compounds NbFeSb and ZrCoSb. Fine bulk-samples are obtained by an arc-melting followed by spark plasma sintering. NbFeSb exhibited lower Debye temperature and a higher GrÜneisen parameter than those of ZrCoSb. High-temperature XRD analyses revealed that NbFeSb is more stable at high temperatures than ZrCoSb in both an inert gas atmosphere and in air. It can be concluded that NbFeSb is more suitable for *p*-type half-Heusler TE materials than ZrCoSb in the viewpoint of not only the TE properties but also the thermomechanical properties and high-temperature stability.

The TE properties of Ti-, Zr, and Hf-substituted NbFeSb samples are investigated from room temperature to 1073 K. The Ti-substituted sample is nearly a single phase while the Zr- and Hf-substituted samples contained secondary phases in addition to the HH phase. These secondary phases had significant influences on the TE properties. In the present case, the Hf-substituted sample exhibited the lowest κ_{lat}, while the Ti-substituted sample showed the highest power factor. As a result, the Ti-substituted sample exhibited the best zT values, zT_{max} = 0.7 at 1073 K.

The combination of the Melt-spinning and spark plasma sintering technique is an effective way to suppress κ_{lat} and enhance zT. In this case, melt spinning with 2000 rpm is the optimize rotation speed, which gives the lowest κ_{lat} and highest zT. The nanostructuring is possible to perform in *p*-type $Nb_{0.9}Ti_{0.1}FeSb$ half-Heusler compound.

2.5 Reference

[1] C. B. H. Evers, C. G, Richter, K. Hartjes, W. Jeitschko, *J. Alloy. Comp.*, 93, 252 (1997).

[2] C. Fu, T. Zhu, Y. Liu, H. Xie and X. Zhao, *Energy Environ. Sci.*, 8, 216 (2015).

[3] C. Fu, T. Zhu, Y. Pei, H. Xie, H. Wang, G. J. Snyder, Y. Liu, Y. Liu and X. Zhao, *Adv. Energy Mate.*, 4, 1400600 (2014).

[4] Hsin Lin, L. Andrew Wray, Yuqi Xia, Suyang Xu, Shuang Jia, Robert J. Cava, Arun Bansil & M. Zahid Hasan, *Nat. Mater.*, 9, 546 (2010).

[5] X. Zhang, Y. Wang, Y. Yan, C. Wang, G. Zhang, Z. Cheng, F. Ren, H. Deng and J. Zhang: Sci. Rep. 6, 1-13 (2016).

[6] H. Zhao, B. Cao, S. Li, N. Liu, J. Shen, S. Li, J. Jia, L. Gu, Y. Pei, G. J. Snyder, Z. Ren and X. Chen: Adv. Energy Mater. 7, 1700446-1–11 (2017).

[7] ICSD Card No: 01-087-2169 (FeNbSb)

[8] ICSD Card No: 00-054-0448 (ZrCoSb)

[9] C. Fu, S. Bai, Y. Liu, Y. Tang, L. Chen, X. Zhao, T. Zhu, *Nat. Commun.*, 6, 8144 (2015).

[10] T. Sekimoto, K. Kurosaki, H. Muta and S. Yamanaka, *Jpn. J. Appl. Phys.*, 46, L673 (2007).

[11] T. Sekimoto, K. Kurosaki, H. Muta and S. Yamanaka, *Mater. Trans.*, 46, 1481 (2005).

[12] Y. Xia, S. Bhattacharya, B. Ponnambalam, A. L. Pope, S. J. Poon, and T.M. Tritt, *J. Appl. Phys.*, 88, 1952 (2000).

[13] D. Jung, K. Kurosaki, C. Kim, H. Muta and S. Yamanaka, *J. Alloy. Comp.*, 489, 328 (2010).

[14] O. L. Anderson, *J. Phys. Chem. Solids.*, 24, 909 (1963).

[15] W. G. Zeier, A. Zevalkink, Z. M. Gibbs, G. Hautier, M. G. Kanatzidis, and G. J. Snyder, *Solid State Chem.*, 55, 6826 (2016).

[16] Y.J. Meisner and Chen L., *Appl. Phys. Lett*. 85, 1140-2 (2004).

[17] K. Biswas, J. He, I. D. Blum, C. Wu, T. P. Hogan, D. N. Seidman, V. P. Dravid, and M. G. Kanatzidis, *Nature*. 489, 414-418 (2012).

[18] C. Fu, T. Zhu, Y. Liu, H. Xie and X. Zhao: *Energy Environ. Sci*., 8, 216-220 (2015).

[19] C. Fu, S. Bai, Y. Liu, Y. Tang, L. Chen, X. Zhao and T. Zhu: *Nat. Commun.*, 6, 8144-1–7 (2015).

[20] W. Kim, *J. Mater.Chem. C*. 3, 10336 (2015).

[21] P. Esksuwanchai, S. Tanusilp, P. Jood, and M. Ohta, *Appl. Energy Mater*. 1, 6586-92 (2018).

Chapter III

Thermoelectric and Thermomechanical properties of *n*-type $Nb_{0.85}CoSb$ HH compound

3.1 Introduction

Since half-Heusler compounds have such an outstanding potential to be candidate TE materials, it has been widely reported that HH with 18 VEC exhibits a large Seebeck coefficient, good mechanical properties, and stable at high-temperature. NbCoSb is also in the HH family with nominal 19 valence electrons, which very low thermopower at RT [1,2]. However, NbCoSb with 19 VEC was achieved a peak zT of 0.5 at 973 K, but impurity phased always exist in this material [3]. Recently, $Nb_{0.8+\delta}CoSb$ ($0 \leq \delta \leq 0.05$) with a large amount of Nb vacancies was predicted to be a more stable semiconductor. Furthermore, this composition exhibit 18 VEC and an influence on the thermoelectric properties [4]. The idea of adjusting the VEC number is attracted to the present dissertation. It is expected that *n*-type $Nb_{0.8+\delta}CoSb$ is suitable for *p*-type NbFeSb HH compound.

In this study, I focus on $Nb_{0.85}CoSb$ composition due to there is a closer number to 18 VEC. The substitution technique is used to develop the thermoelectric properties of $Nb_{0.85}CoSb$. $Nb_{0.75}M_{0.1}CoSb$ is substituted by 10% of the transition metals (M = Ti, Zr, and Hf) into the Nb sites. Here, we investigate the TE and thermomechanical properties as well as the high-temperature stability of *n*-type Nb-based HH compounds. The results of *p*-type $Nb_{0.9}M_{0.1}FeSb$

are compared with *n*-type data in order to clearly understand the compatibility between *p*-type and *n*-type TE materials. Finally, I endeavor to assemble an Nb-based HH TE module consist of the best *p*-type $Nb_{0.9}M_{0.1}FeSb$ from Chapter II and the best *n*-type $Nb_{0.75}M_{0.1}CoSb$ from this Chapter. The detail of the module will present in Chapter IV.

3.2 Experimental Details

Materials synthesis and characterization: According to the literature [5], $Nb_{0.83}CoSb$ shows the best TE properties for *n*-type Nb_yCoSb HH compounds. Here, the nominal composition of $Nb_{0.75}M_xCoSb$ (*M* = Ti, Zr, Hf) with $x = 0.1$ is selected. Ingots with the nominal compositions $Nb_{0.75}M_{0.1}CoSb$ (*M* = Ti, Zr, Hf) are synthesized by arc melting under an Ar atmosphere. Nb (chunk, 99.9%), Co (shot, 99.97%), Sb (shot, 99.999%), Ti (stick, 99.9%), Zr (chunk, 99.9%), and Hf (chunk, 99.9%) are used as the starting materials. All ingots are flipped and re-melted at least six times to homogenize the alloys during arc melting. The obtained ingots are crushed into powders, then loaded into a graphite die and sintered at 1283 K for 15 min under 82 MPa under an Ar atmosphere by the spark plasma sintering (SPS). An undoped $Nb_{0.85}CoSb$ sample is prepared using the same method for comparison. The density (*d*) of as-sintered samples is evaluated from the measured weight and dimensions. The crystal structure is investigated by powder X-ray diffraction (XRD) analysis. The data are collected on a diffractometer on Rigaku Ultima IV with Cu Kα radiation (λ_0 = 1.5406 Å) in air at 300 K. The microstructure of the SPS samples is investigated by scanning electron microscopy (SEM). The chemical composition is analyzed by energy dispersive X-ray (EDX) spectroscopy with the detector resolution of 138 eV. The standard deviation of thus obtained average compositions is within ±2%.

Thermoelectric properties: σ and *S* are measured using a commercial apparatus (ZEM-3, ADVANCE RIKO, Inc.) under a reduced He atmosphere from 300 - 1073 K. The accuracy is ±3%. The Hall carrier concentration (n_H) and Hall mobility (μ_H) are calculated by $n_H = 1/eR_H$ and $\mu_H = \sigma R_H$, where *e* is the elementary charge and R_H is the Hall coefficient. R_H is measured by van de Pauw method in vacuum under applied magnetic field (0.5 T) using a commercial apparatus (Resitest8300, TOYO Corporation) at 300 K. Estimated errors of thus obtained Hall coefficient

are within ±5%. κ is calculated from heat capacity (C_p), thermal diffusivity (α) and d using the relationship $\kappa = \alpha C_p d$. α is measured from 300 to 1073 K using a flash diffusivity apparatus (LFA-457, NETZSCH) with a standard deviation around ±3%. C_p is estimated by the model of Dulong and Petit, i.e., $C_p = 3nR$, where n is the number of atoms per formula unit and R is the gas constant.

High-temperature stability and thermomechanical properties: Thermal expansion is measured using a dilatometer (TD5000SA, Bruker AXS) from 300 to 1073 K in an Ar atmosphere. The rectangular-shaped samples are cut from the SPS samples and used for the dilatometer measurement. From the obtained thermal expansion curves, the average value of the linear thermal expansion coefficient (α_L) in the temperature range from T_{RT} (=300) to T (= 773 K) is calculated by equation (2.1). The high-temperature (HT)-XRD patterns for the powder samples are collected from 300 to 1073 K in both air and inert atmosphere. The α_L is calculated using the lattice parameter values, evaluated from the HT-XRD patterns obtained from the measurements performed in the inert atmosphere. The longitudinal (v_L) and shear sound velocities (v_S) are measured by an ultrasonic pulse-echo method at 300 K in air using a 5 MHz longitudinal and shear sound wave echogenic transducer. A relative accuracy of each velocity is around ±5%. The Debye temperature (θ_D), and bulk modulus (B) are calculated from the sound velocities.

3.3 Results and Discussion

3.3.1 Thermoelectric Properties of *n*-type Nb-Based HH Compounds

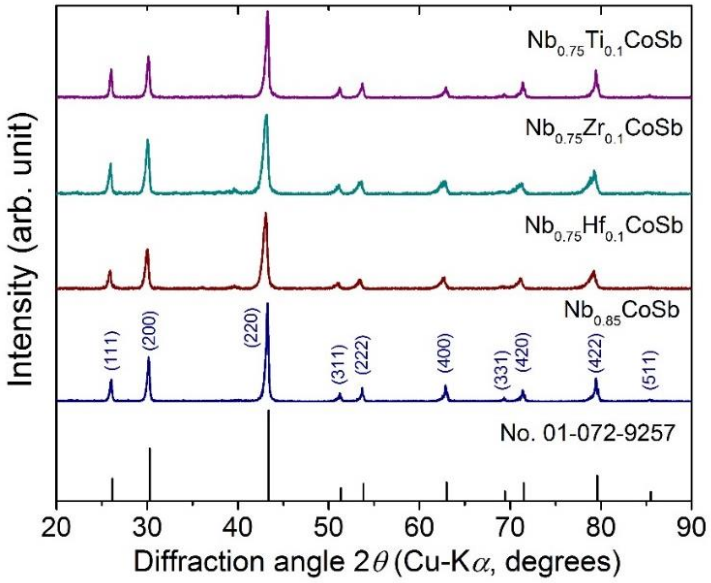

Figure 3.1 Powder XRD patterns of the SPS bulk samples of $Nb_{0.75}M_{0.1}CoSb$ (*M* = Ti, Zr, Hf).

Figure 3.1 shows the powder XRD patterns for the bulk samples of $Nb_{0.75}M_{0.1}CoSb$ (*M* = Ti, Zr, Hf). The XRD results confirm that all the samples are nearly single phase of the HH structure with space group *F*4-3*m*. As summarized in Table 3.1, the lattice parameters (*a*) increase with increasing the atomic number of *M*, which can be roughly explained from the ionic radii of M^{4+} with the coordination number of 8, i.e., Ti^{4+} (0.74 Å) < Zr^{4+} (0.84 Å) ≈ Hf^{4+} (0.83 Å). [2] The measured and relative densities of each sample are summarized in Table 3.1.

Table 3.1 The actual compositions determined by the quantitative EDS analysis, lattice parameter *a*, densities *d*, and relative densities %T.D. of the SPS bulk samples of $Nb_{0.75}M_{0.1}CoSb$ (*M* = Ti, Zr, Hf).

Compositions		***a*** **(nm)**	***d*** **(gcm^{-3})**	**%T.D.**
Nominal	**Actual**			
$Nb_{0.75}Ti_{0.1}CoSb$	$Nb_{0.76}Ti_{0.14}Co_{0.99}Sb_{1.00}$	0.59036(3)	8.15	92
$Nb_{0.75}Zr_{0.1}CoSb$	$Nb_{0.71}Zr_{0.15}Co_{0.96}Sb_{1.00}$	0.59183(5)	8.32	94
$Nb_{0.75}Hf_{0.1}CoSb$	$Nb_{0.69}Hf_{0.15}Co_{0.97}Sb_{1.00}$	0.59271(10)	8.58	97

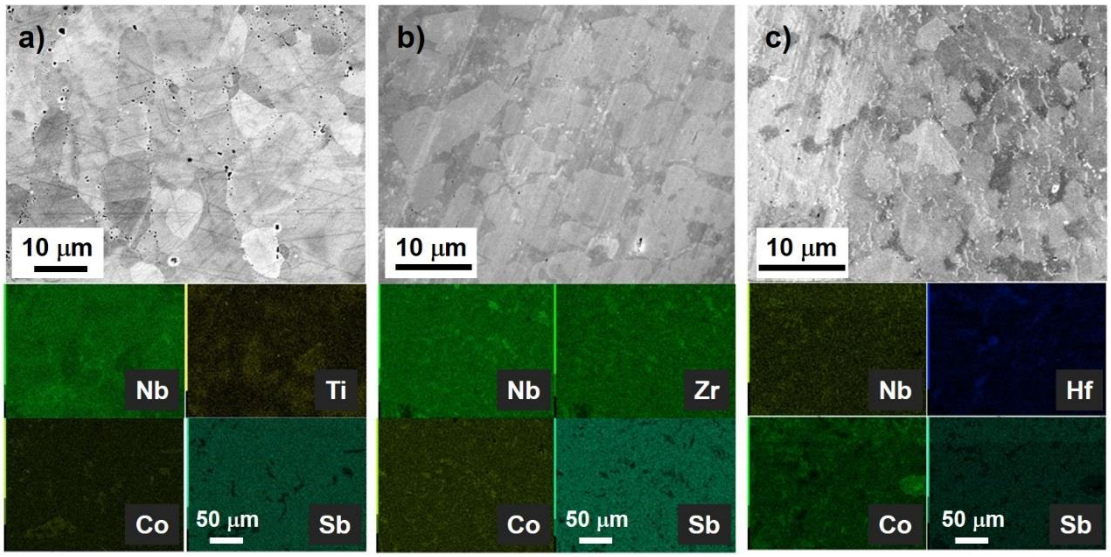

Figure 3.2 SEM and EDS elemental mapping images of the bulk samples, a) $Nb_{0.75}Ti_{0.1}CoSb$, b) $Nb_{0.75}Zr_{0.1}CoSb$, and c) $Nb_{0.75}Hf_{0.1}CoSb$.

As can be confirmed from the SEM images in Figure 3.2, the grain sizes of all the bulk samples of $Nb_{0.75}M_{0.1}CoSb$ (*M* = Ti, Zr, Hf) are around 5~12 μm. The elemental mapping analysis reveals that all elements distribute nearly homogeneously in all the bulk samples. However, in $Nb_{0.75}Zr_{0.1}CoSb$, small amounts of precipitates composed of Nb and Zr are observed. Also, in $Nb_{0.75}Hf_{0.1}CoSb$, a Nb-rich small region, as well as a large Co-rich region, is observed. The actual compositions of all the samples are determined by quantitative EDS analysis (Table 3.1). The *M* element contents in the actual compositions are slightly higher than those in the nominal ones.

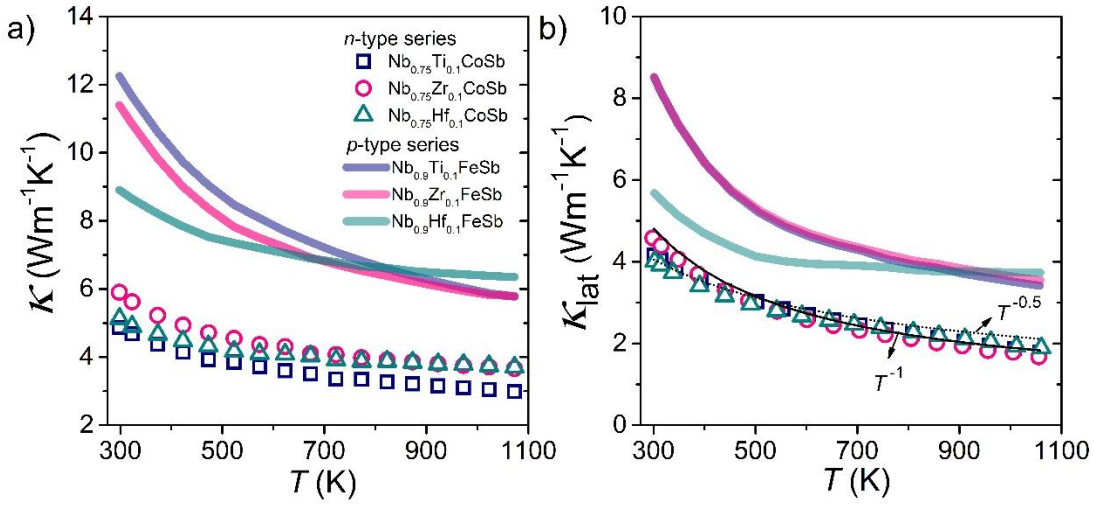

Figure 3.3 Temperature dependences of a) the thermal conductivity, κ and b) lattice thermal conductivity, κ_{lat} of the SPS bulk samples of the *n*-type $Nb_{0.75}M_{0.1}CoSb$.

Figure 3.3 shows κ and κ_{lat} of *n*-type $Nb_{0.75}M_{0.1}CoSb$, together with the previous data of *p*-type $FeNb_{0.9}M_{0.1}Sb$. κ_{lat} is calculated as $\kappa_{lat} = \kappa - L_0\sigma T$, where L_0 is the Lorenz number (2.44×10^{-8} $W\Omega K^{-2}$). All the *n*-type samples have remarkable lowest κ and κ_{lat} than those of the *p*-type samples, even though they have the same crystal structure and similar substitution ratio of *M* element. This means that not only the substituted *M* elements but also the Nb-site vacancies act as the phonon scattering center. All the κ_{lat} data follow a $\kappa_{lat} \sim T^a$ ($-0.5 < a < -1$) behavior. To confirm such low κ_{lat} of the *n*-type samples, the Grüneisen parameters (γ) of *n*- and *p*-type samples are evaluated by Equation 2.8. These mechanical properties of *n*-type samples are summarized in Table 3.2. The γ values of *n*-type $Nb_{0.75}M_{0.1}CoSb$ are 1.73~1.80 (300-773 K) , whereas those of *p*-type $FeNb_{0.9}M_{0.1}Sb$ are 1.09~1.64 (300-1073 K), as can be seen from Table 2.7. These higher γ values of the *n*-type samples means higher anharmonicity of the materials, leading to lower κ_{lat}.

Table 3.2 Physical properties of the SPS bulk samples of $Nb_{0.75}M_{0.1}CoSb$ (M = Ti, Zr, Hf) obtained by the sound velocity measurements.

Physical Properties	**$Nb_{0.75}Ti_{0.1}CoSb$**	**$Nb_{0.75}Zr_{0.1}CoSb$**	**$Nb_{0.75}Hf_{0.1}CoSb$**
Longitudinal velocity, v_L (ms^{-1})	5513	5468	5409
Transverse velocity, v_S (ms^{-1})	3059	3021	3008
Average sound velocity, v_m (ms^{-1})	3407	3366	3350
Young's modulus, E (GPa)	195	194	198
Bulk modulus, B (GPa)	146	147	147
Poisson ratio, ν	0.27	0.28	0.27
Debye temperature, θ_D (K)	385	381	379
Grüneisen parameter, γ (300-773 K)	1.73	1.75	1.80

Figure 3.4 shows the temperature dependences of σ, S, $S^2\sigma$, and zT of the n-type $Nb_{0.75}M_{0.1}CoSb$, together with the previous data of p-type $FeNb_{0.9}M_{0.1}Sb$ samples. All the samples show negative temperature dependences in both σ and S, exhibiting a typical degenerated semiconductor behavior. The n-type samples exhibit small σ values than those of the p-type samples. This is because the n-type samples have large amount of the Nb-site vacancies which introduce alloy disorder scattering, leading to the great reduction of the carrier mobility. [5] To confirm this, the Hall effect measurement is performed at 300 K. n_H and μ_H values of the n-type samples together with the previous data of the p-type samples are summarized in Table 3.3. Among the n-type samples, the Ti-doped sample shows the lowest n_H value because Ti (χ = 1.54) is more electronegative element than Zr (χ = 1.33) and Hf (χ = 1.33) [3], where χ is the electronegativity (arb. unit). In other words, Ti tends to give less free electrons to the compound. Also, the Ti-doped sample exhibits the smallest μ_H. To understand the μ_H characteristic, the effective mass (m^*/m_0) values are estimated from the measured n_H and S at 300 K (Table 3.3), using a simple parabolic band model considered with acoustic phonon scattering as follows:

$$F(\eta)_i = \int_0^\infty \frac{x^i dx}{1+e^{x-\eta}}, \qquad (3.1)$$

$$S = \frac{k_B}{e}\left[\frac{2F_1(\eta)}{F_0(\eta)} - \eta\right], \tag{3.2}$$

$$n_H = 4\pi\left[\frac{2m^* k_B T}{h^2}\right]^{3/2} \frac{F_{1/2}(\eta)}{r_H}, \tag{3.3}$$

where F_i is the Fermi Dirac integral of order i, η is the reduced Fermi energy, k_B is the Boltzmann constant, h is the Planck constant, and r_H is the Hall factor (r_H = 1).

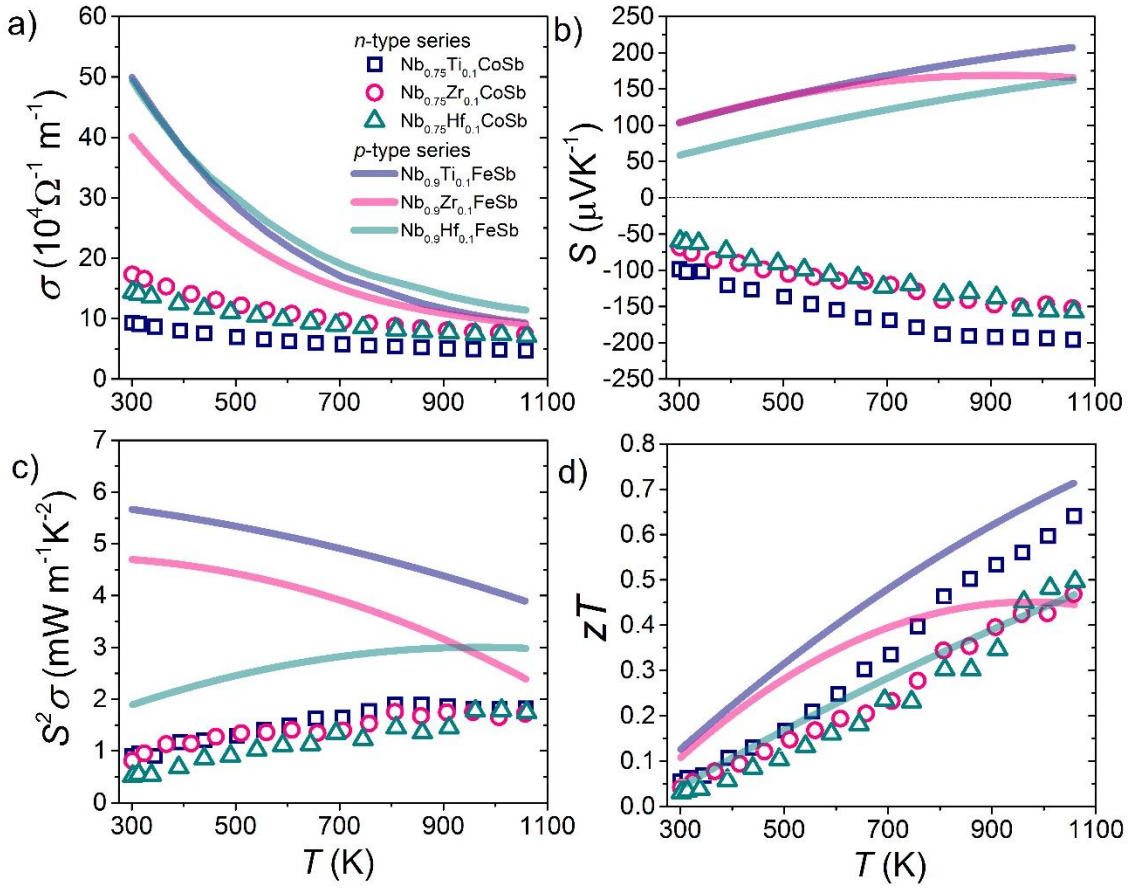

Figure 3.4 Temperature dependences of a) the electrical conductivity, σ b) Seebeck coefficient, S c) power factor, $S^2\sigma$, and d) the dimensionless figure of merit, zT of the SPS bulk samples of n-type $Nb_{0.75}M_{0.1}CoSb$.

The estimated m^*/m_0 of Ti-, Zr-, and Hr-doped samples are 2.57, 1.88, and 1.59, respectively. It can be confirmed such a large m^*/m_0 of the Ti-doped sample leads to the great reduction in mobility. [4] Further, as can be seen in Figure 3.4b, the Ti-doped sample has the largest negative *S* values for the *n*-type samples, approximately -200 μVK^{-1} at 1073 K. This large *S* value can be explained by the large m^*/m_0 compared with the other samples. The power factor values of all the *n*-type samples are lower than those of the *p*-type samples (Figure 3.4c). The maximum power factor value of the *n*-type samples is around 2 $mWm^{-1}K^{-2}$ at 800 - 1073 K obtained for the Ti-doped sample. However, owing to the low κ and κ_{lat} values, the *zT* values of the *n*-type samples are comparable to those of the *p*-type samples (Figure 3.4d). The maximum *zT* value is around 0.7 at 1073 K obtained for the Ti-doped sample.

Table 3.3 Seebeck coefficient *S*, Hall carrier concentration n_H, and Hall mobility μ_H of *n*-type $Nb_{0.75}M_{0.1}CoSb$ (*M* = Ti, Zr, Hf) at 300 K. The data for *p*-type $Nb_{0.9}M_{0.1}FeSb$ are shown for comparison.

Carrier Type	**Compounds**	***S* (μVK^{-1})**	**n_H ($\times 10^{20}$ cm^{-3})**	**μ_H ($cm^2V^{-1}s^{-1}$)**
n	$Nb_{0.75}Ti_{0.1}CoSb$	-98.4	3.71	14.2
	$Nb_{0.75}Zr_{0.1}CoSb$	-68.4	4.20	24.1
	$Nb_{0.75}Hf_{0.1}CoSb$	-59.7	4.02	23.1
p	$Nb_{0.9}Ti_{0.1}FeSb$	102.1	8.94	34.3
	$Nb_{0.9}Zr_{0.1}FeSb$	99.5	9.48	32.2
	$Nb_{0.9}Hf_{0.1}FeSb$	60.1	9.13	38.4

In the next part, to evaluate the overall characteristics for developing a HH-based TE module, the thermomechanical properties as well as the high-temperature stability of the *n*-type HH compounds are evaluated and the obtained results are compared with those of the *p*-type HH compounds.

3.3.2 High-Temperature Stability and Thermoelectric Properties of Nb-Based HH Compounds

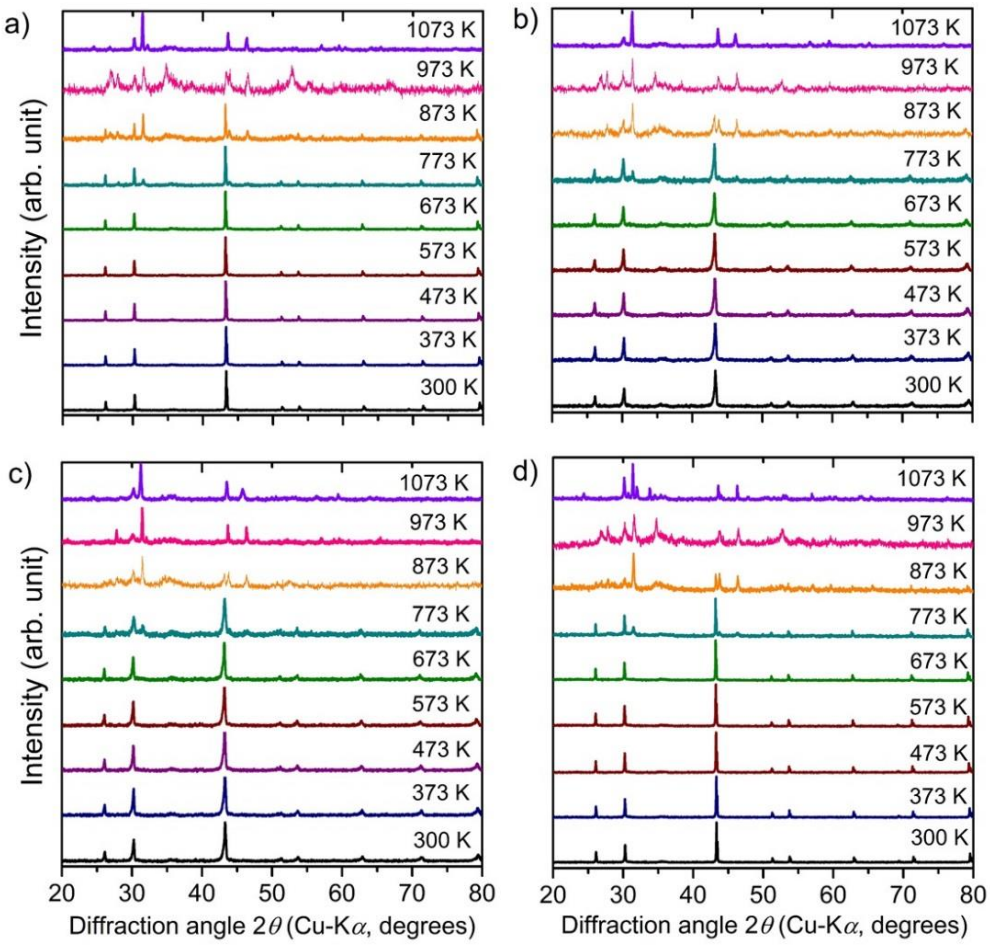

Figure 3.5 HT-XRD patterns of the *n*-type samples, a) $Nb_{0.75}Ti_{0.1}CoSb$, b) $Nb_{0.75}Zr_{0.1}CoSb$, c) $Nb_{0.75}Hf_{0.1}CoSb$, and d) $Nb_{0.85}CoSb$ collected in air in the temperature range 300 - 1073 K.

In order to evaluate the high-temperature stability, the HT-XRD was performed in air and an inert atmosphere for both *n*-type $Nb_{0.75}M_{0.1}CoSb$ and *p*-type $FeNb_{0.9}M_{0.1}Sb$. As can be seen in Figure 3.5, the HT-XRD patterns of all the *n*-type samples, a peak at 2θ equals around 32 degree appears at 773 K in addition to the peaks derived from the HH phase, meaning that the *n*-type $Nb_{0.75}M_{0.1}CoSb$ is stable up to 673 K even in air. Similar to the *p*-type samples.

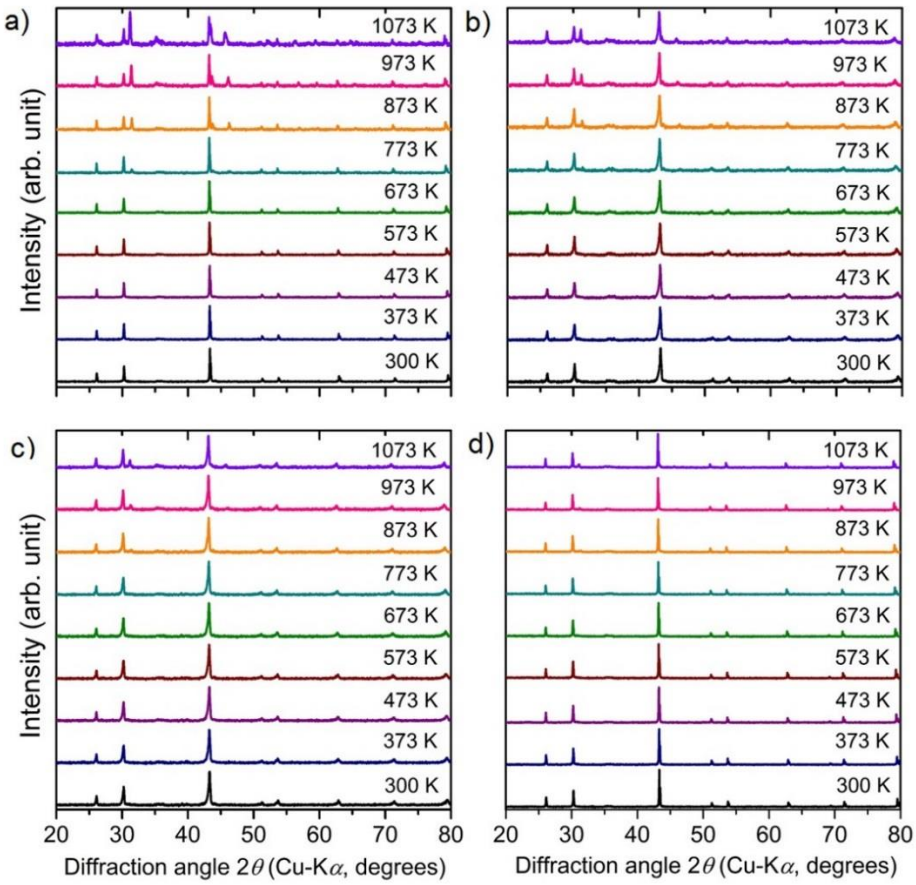

Figure 3.6 HT-XRD patterns of the *n*-type samples, a) $Nb_{0.75}Ti_{0.1}CoSb$, b) $Nb_{0.75}Zr_{0.1}CoSb$, c) $Nb_{0.75}Hf_{0.1}CoSb$, and d) $Nb_{0.85}CoSb$ collected in an inert atmosphere in the temperature range 300 - 1073 K.

As can be seen in Figure 3.6, the non-doped *n*-type $Nb_{0.85}CoSb$ is stable up to 1073 K in an inert atmosphere. Although a small peak is being to appear at 2θ equals around 32 degrees in the XRD patterns at 773 K for the Ti- and Zr-doped *n*-type samples, it can be said that the doped samples are almost stable up to 773 K. On the other hand, as can be seen in Figure 2.15, all the p-type samples (both of doped and non-doped) are stable up to 1073 K). All the HH peaks shift towards lower angle with increasing temperature because of the lattice thermal expansion. In the temperature ranges of 300 - 1073 K for the non-doped $Nb_{0.85}CoSb$ and all the *p*-type samples and 300 - 773 K for the doped *n*-type samples, the average α_L values were evaluated from the temperature dependences of the lattice parameters. The results are summarized in Table 3.4.

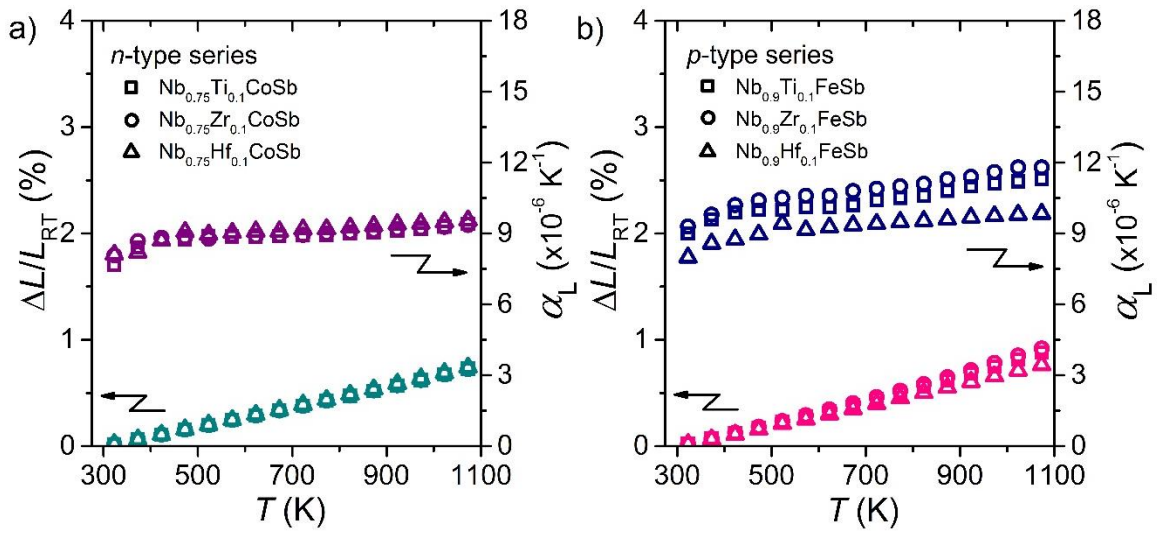

Figure 3.7 Thermal expansion, $\Delta L/L_{RT}$ and linear thermal expansion coefficient, α_L of a) the *n*-type $Nb_{0.75}M_{0.1}CoSb$ and b) *p*-type $Nb_{0.9}M_{0.1}FeSb$ (*M*= Ti, Zr, Hf) obtained by the dilatometer measurement in the temperature range 300 - 1073 K.

Figure 3.7 indicates the temperature dependences of the thermal expansion ($\Delta L/L_{RT}$) and linear thermal expansion coefficient (α_L) in the temperature range 300 - 1073 K of the *n*-type $Nb_{0.75}M_{0.1}CoSb$ (Figure 3.7a) , together with the measured data of *p*-type $Nb_{0.9}M_{0.1}FeSb$ (Figure 3.7b). From the measured α_L values plotted in this figure, the average α_L values in the temperature ranges 300 - 773 K for the *n*-type samples and 300 - 1073 K for the *p*-type samples are calculated. The results are summarized in Table 3.4. There are differences in the average α_L values measured by the two methods. The α_L values of the *n*-type samples measured by HT-XRD are larger than those of the *p*-type samples, but ones obtained by the dilatometer measurements are smaller. Note that here the temperature ranges used in calculating the α_L values are different, resulting in such inconsistencies. Moreover, the α_L values of each doped system measured by both techniques do not trend with each other. The sample types used for the HT-XRD and the dilatometer measurement are fine powders and bulks, respectively. It is suggested that defects existed in bulk samples such as pores and cracks might disturb the accurate dilatometer measurement, resulting for the conflicting data.

Table 3.4 Average linear thermal expansion coefficient, α_L of the *n*-type $Nb_{0.75}M_{0.1}CoSb$ and *p*-type $Nb_{0.9}M_{0.1}FeSb$, evaluated from the HT-XRD and dilatometer methods.

Carrier Type	**Compounds**	**α_L ($\times 10^{-6}$ K^{-1})**		***T* (K)**
		HT-XRD	**Dilatometer**	
n	$Nb_{0.75}Ti_{0.1}CoSb$	10.34	9.01	300-773
	$Nb_{0.75}Zr_{0.1}CoSb$	10.59	9.02	
	$Nb_{0.75}Hf_{0.1}CoSb$	9.55	9.27	
p	$Nb_{0.9}Ti_{0.1}FeSb$	8.71	11.28	300-1073
	$Nb_{0.9}Zr_{0.1}FeSb$	8.57	11.79	
	$Nb_{0.9}Hf_{0.1}FeSb$	6.79	9.89	

According to TE properties and thermal stability, Ti-substituted *p*-type and *n*-type samples are selected. Considering at the same temperature 773 K, the α_L of *p*-type $Nb_{0.9}Ti_{0.1}FeSb$ is 10.5×10^{-6} K^{-1}, while the α_L of *n*-type $Nb_{0.75}Ti_{0.1}CoSb$ is 9.01×10^{-6} K^{-1}. Thus the calculated $\%\Delta\alpha_L$ between *p*-type and *n*-type is 14%. This value is lower than the reference data in Table 1.2. Thus this small percentage is acceptable in the group of different material types. As reported by the data of TE properties and thermal stability, *n*- and *p*-type Ti-doped system has a small percentage of different α_L, which is an outstanding character for fabricating a TE module.

3.3.3 Compatibility of *p*- and *n*-type HH compounds

As mention above, achieving a high-performance TE module, not only *zT* but also high-temperature stability between *p*- and *n*-type materials, should be comparable, which is the key parameter for fabrication a module. In this study, there are three properties needed to be considered for checking the compatibility between *p*- and *n*-type.

***High-temperature stability*;** good TE material should be stable at high-temperature because this module is working under high-temperature differences in a practical situation. This property is identified by powder XRD pattern from HT-XRD measurement, as can be seen in Figure 2.14, 2.15 for *p*-type HH samples and Figure 3.5, 3.6 for *n*-type HH samples. The results confirmed that all samples stable up to 1073 K in a He atmosphere and 773 K in air. It means *p*- and *n*-type Niobium-based HH compound is appropriated for working under a high-temperature environment.

***Similar linear thermal expansion coefficient*;** in this study, the average linear thermal expansion coefficient, α_L of *p*- and *n*-type, are obtained from two methods, calculated lattice expansion from HT-XRD data and obtained from Dilatometer measurement. Table 3.4 reveals the comparison of the average α_L of *p*- and *n*-type samples. All samples can be comparable. However, in this case, the $\%\Delta\alpha_L$ of NbFeSb/$Nb_{0.85}$CoSb is smaller than the reference data in Table 1.2. The Ti-substituted *p*- and *n*-type system demonstrated the highest *zT* and small $\%\Delta\alpha_L$ between *p*-type and *n*-type is only 14%. It might be said that this couple is better than another couple because of the lowest $\%\Delta\alpha_L$. It is expected that NbFeSb/$Nb_{0.85}$CoSb HH TE material is an excellent couple for the fabrication of a TE module.

***Thermoelectric performance*;** The excellence conversion efficiency of TE module required high TE properties such as large Seebeck coefficient, high power factor, high electrical conductivity and low lattice thermal conductivity to produced maximize *zT*. All TE properties are compared in Figure 3.4. TE properties of *p*- and *n*-type Nb-based HH compounds can be approved that the Ti-substituted sample demonstrated high TE performance than those of other elements. Therefore, Ti-substituted *p*- and *n*-type Niobium-based HH compounds are selected to fabricated a *2π*-module in a simulation program, COMSOL Multiphysics. The simulated result is shown in the next Chapter.

3.4 Summary

The *n*-type Nb-based HH compounds substituted by the *M* elements, $Nb_{0.75}M_{0.1}CoSb$ (*M* = Ti, Zr, Hf), are synthesized, and their TE properties, as well as the thermomechanical properties/high-temperature stability, is investigated. $Nb_{0.75}Ti_{0.1}CoSb$ exhibited the largest *zT* of 0.7 at 1073 K and excellent high-temperature stability in both in air and an inert atmosphere. Moreover, the $Nb_{0.75}Ti_{0.1}CoSb$ showed a good compatibility with the *p*-type $Nb_{0.9}Ti_{0.1}FeSb$ in terms of the TE properties and the linear thermal expansion coefficient. Therefore, for a promising couple for fabricating a TE module, it can be concluded that the Ti-doped system is the best system among the other systems in both *n*-and *p*-type Nb-based HH compounds.

3.5 Reference

[1] K. Kaczmarska, J. Pierre, J. Beille, J. Tobola, R. V. Skolozdra, and G. A. Melnik, *J. Magn, Mater*., 187, 210 (1998).

[2] J. Tobola and J. Pierre, *J. Alloys Compd*., 296, 243 (2000).

[3] H. Zhang, Y. Wang, L Huang, S. Chen, H. Dahal, D. Wang, and Z. Ren, *J. Alloys Compd.*, 654, 321 (2016).

[4] W.G. Zeier, S. Anand, L. Huang, R. He, H. Zhang, Z. Ren, C. Wolverton, and G. J. Snyder, *Chem. Mater*., 29, 1210 (2017).

[5] K. Xia, Y. Liu, S. Anand, G. J. Snyder, J. Xin, J. Yu, X. Zhao and T. Zhu, *Adv. Funct. Mater*., 28, 1705845 (2018).

[6] R. D. Shannon and C. T. Prewitt, *Acta Cryst.*, B25, 925 (1969).

[7] G. Brown, The Inaccessible Earth: An Integrated View to Its Structure and Composition, Springer Science & Business Media, Cham, Switzerland, 2012.

[8] Y. Pei, A. D. LaLonde, H. Wang and G. J. Snyder, *Energy Environ. Sci.*, 5, 7963–7969 (2012).

Chapter IV

The Efficiency of Thermoelectric Module based on Nb-based HH compound

To understand the module behavior, confirm experimental measurements, and predict the possibility of module performance, the simulation part is needed to study. In this Chapter, half-Heusler (HH) compounds are currently promising thermoelectric (TE) materials due to their outstanding performance. For reliable *n*- and *p*-type HH compounds, the dimensionless figure of merit *zT* is needed to maximized. However, to develop a high-performance TE module, not only *zT* but also high-temperature stability, thermal expansion, and compatibility of *p*- and *n*-type materials become key parameters. Previous Chapter, I investigate the TE and thermomechanical properties as well as the high-temperature stability of Nb-based HH compounds: *n*-type $Nb_{0.75}M_{0.1}CoSb$ and *p*-type $FeNb_{0.9}M_{0.1}Sb$ (*M* = Ti, Zr, Hf). The performance of a 2π-module based on the best *n*-type $Nb_{0.75}Ti_{0.1}CoSb$ and *p*-type $FeNb_{0.9}Ti_{0.1}Sb$ is simulated by using the COSMOL code. The conversion efficiency (ω_{max}) and maximum power output (η_{max}) of the 2π-module are reported. The simulation section was computed at AIST Tsukuba center[1].

[1] *National Institute of Advanced Industrial Science and Technology (AIST), Energy Techology Research Institute, 1-1-1 Umezono, Tsukuba, Ibaraki 305-8568, Japan.*

4.1 COMSOL Multiphysics

The geometry of a 2π-module was constructed in COMSOL. The fabricated module structure and the properties of every material were used to build the model of module.

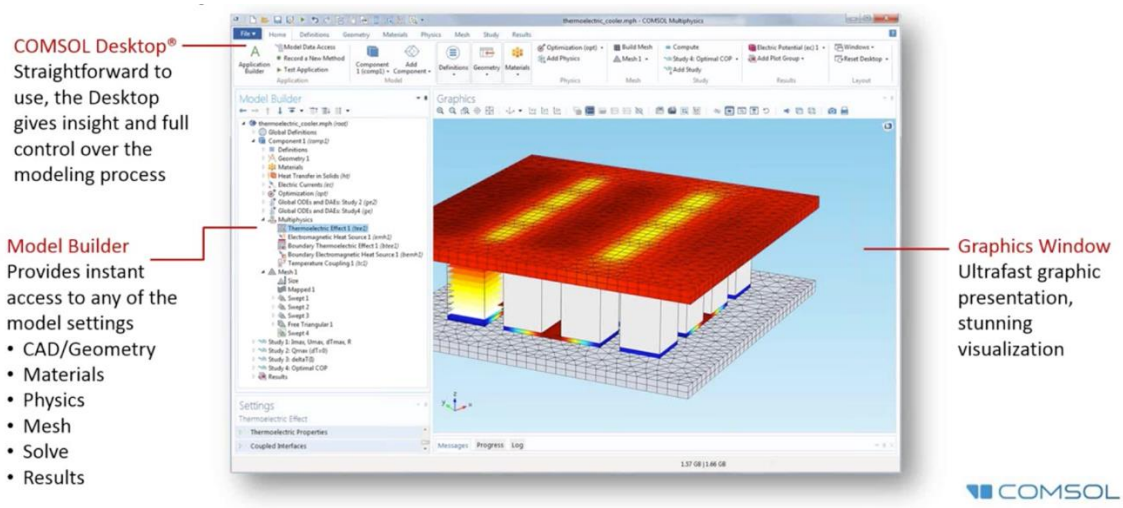

Figure 4.1 COMSOL Multiphysics. [1]

The numerical problem is solved using thermoelectric-effect multiphysics module in temperature gradients (ΔT). The governing equations of the simulation model are mentioned below.

1. Heat transfer in solids; the equation of energy conservation for heat transfer rate.

$$q = -k\nabla T \tag{4.1}$$

2. Electric currents: the current conservation equation.

$$\nabla J = 0 \tag{4.2}$$

3. Thermoelectric effects

$$J = -\sigma\left(-\nabla V - S\nabla T\right) \tag{4.3}$$

$$\nabla\left(k\nabla T\right) + \frac{J^2}{\sigma} - TJ\cdot\nabla S = 0 \tag{4.3}$$

where S is seebeck coefficient, σ is electrical conductivity, κ is thermal conductivity, V is electric potential, J (Am^{-2}) is electrical current density, q (Wm^{-2}) is heat flux, and T (K) is temperature.

The COMSOL Multiphysics is used to simulate the temperature gradient, I-V curve, output power, and conversion efficiency characteristics of the TE module, based on the measured TE materials properties. The partial differential equations used to obtain the module parameters are given by:

$$-\nabla\left(\left(\sigma S^2 T+\kappa\right)\right)\nabla T-\nabla\left(\sigma S\nabla V\right)=\sigma\left(\left(\nabla\right)^2+S\nabla T\nabla V\right) \tag{4.4}$$

$$\nabla\left(\sigma S\nabla T\right)+\nabla\left(\sigma\nabla V\right)=0 \tag{4.5}$$

where σ is the electrical conductivity, S is Seebeck coefficient, and κ is the thermal conductivity of the material. The simulation model, built in COMSOL, is explained in extensive details in references [2,3]. The detail is explained in next part.

Then the output power density (ω) and conversion efficiency (η) can be calculated by following equation:

$$\omega=\frac{P(I)}{A}=\frac{V(I)\times I}{A}, \tag{4.1}$$

$$\eta=\frac{P}{Q_{in}}=\frac{P}{Q_{out}+P}, \tag{4.2}$$

where P is the electrical power of the module, Q_{in} is the heat absorbed, Q_{out} is the heat rejected, I is the electric current, V is the voltage, and A is the total cross-section area of TE legs.

4.2 Thermoelectric *2π*-module design

The TE module performance is theoretically simulated using a 3D model of a *2π*-module by using the COMSOL code. Based on the TE properties as well as the thermomechanical properties, the Ti-substituted samples are selected for assembling a TE module in both *n*- and *p*-types, i.e., $Nb_{0.75}Ti_{0.1}CoSb$ for *n*-type and $Nb_{0.9}Ti_{0.1}FeSb$ for *p*-type. The HH legs are modeled as a rectangular cross-section of dimensions 3×4 mm^2 (*n*-type) and 3×3 mm^2 (*p*-type) of height 5.6 mm. In general, to protect each one of the materials from corrupting to each other, a diffusion layer between both sides of each HH TE leg and Cu electrodes are needed. It has been reported that Mo has a good affinity with *p*-type HH with low contact resistivity of < 1 $\mu\Omega cm^2$. [4] In this simulation, Mo sheets (thickness = 100 μm) are added as a diffusion layer for both *n*- and *p*-type legs. A schematic of the *2π*-module geometry is shown in Figure 4.2.

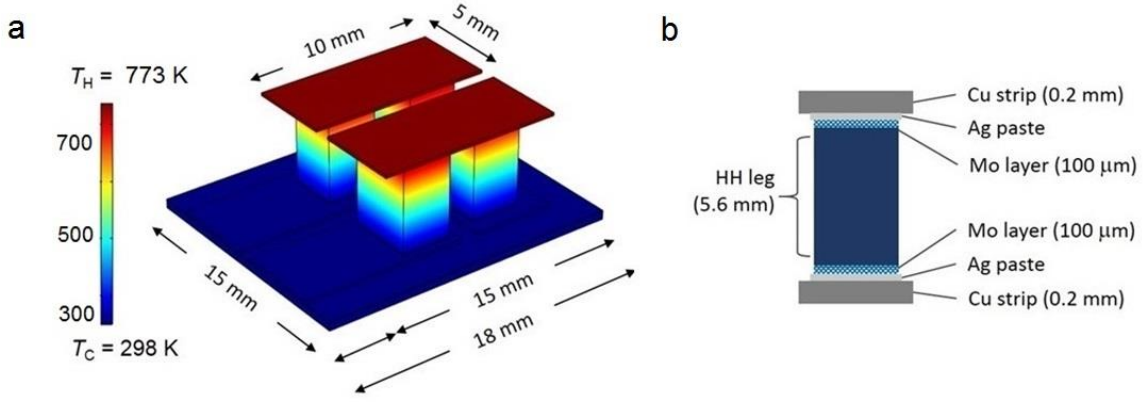

Figure 4.2 a) 3-dimensional schematic of a *2π*-module consisting of *n*- and *p*-type HH legs. b) A HH TE leg with Mo layers.

The initial parameters of *n*- and *p*-type are need to be input for calculation, which summarized in Table 4.1

Table 4.1 The measured thermoelectric characteristic of *n*- and *p*-type HH compound in three-order polynomial as function of temperature. While the properties of Cu, Mo, and polymer are already available in the COMSOL Multiphysics materials library.

Material	**Properties**	$y = aT^3+bT^2+cT+d$			
		a	b	c	d
n-type	S (VK^{-1})	1.674E-13	-1.897E-10	-1.248E-7	-4.813E-5
	σ (Ωm^{-1})	-1.000E-4	2.853E-1	-2.953E+2	1.586E+5
	κ ($Wm^{-1}K^{-1}$)	-5.330E-9	1.392E-5	-1.318E-2	7.665
p-type	S (VK^{-1})	-3.065E-13	5.446E-10	-1.481E-7	1.113E-4
	σ (Ωm^{-1})	-8.305E-4	2.497	-2.663E+3	1.098E+6
	κ ($Wm^{-1}K^{-1}$)	-1.791E-8	4.819E-5	-4.651E-2	2.222E+1
Cu	S (VK^{-1})	-1.00E-6			
	σ (Ωm^{-1})	5.998E+7			
	κ ($Wm^{-1}K^{-1}$)	400			
Mo	S (VK^{-1})	5.00E-6			
	σ (Ωm^{-1})	2.00E+7			
	κ ($Wm^{-1}K^{-1}$)	138			
Polymer	S (VK^{-1})	1.00E-10			
	σ (Ωm^{-1})	1.00E-14			
	κ ($Wm^{-1}K^{-1}$)	10			

4.3 The conversion efficiency of Nb-based HH TE module

In general, a couple of *n*- and *p*-type TE legs should have similar *zT* and thermal expansion coefficient to ensure high efficiency and the integrity of a device. The present study has revealed that the *n*-type $Nb_{0.75}Ti_{0.1}CoSb$ and *p*-type $FeNb_{0.9}Ti_{0.1}Sb$ legs have very similar trends of *zT* at most temperature ranges and they also have the closest α_L. Further, all the doped samples exhibit similar high-temperature stability (Figure 2.14, 2.15 for *p*-type HH samples and Figure 3.5, 3.6 for *n*-type HH samples). Thus, it can be said that the Ti-doped system is most compatible pair to assemble a TE module in terms of both TE and thermomechanical properties.

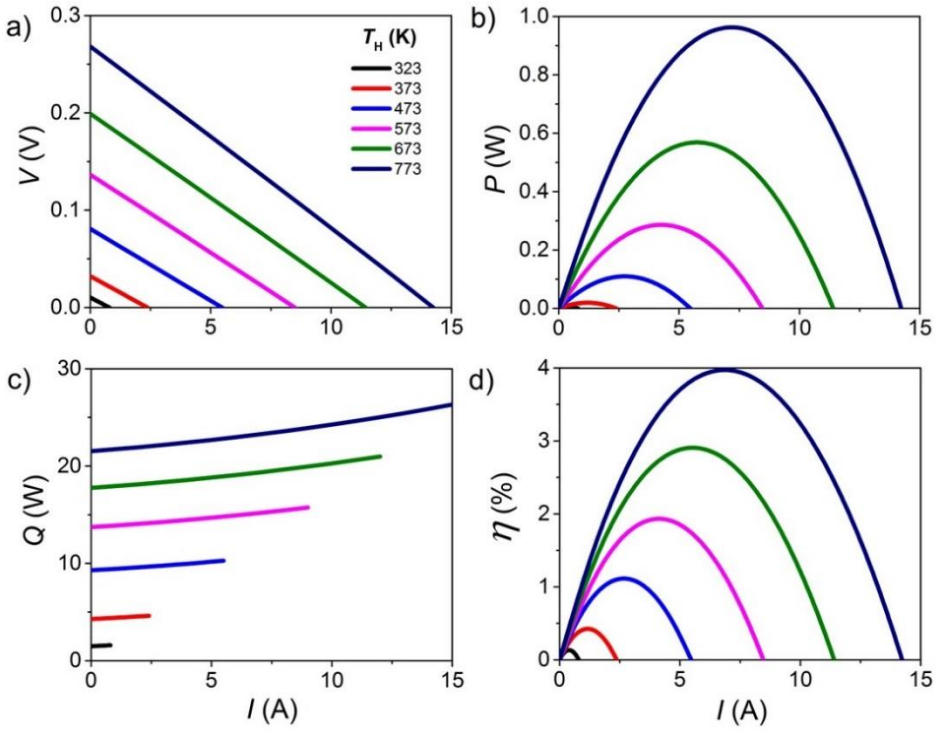

Figure 4.3 Simulation results of characteristic curves of a) voltage-current (*V*-*I*), b) power-current (*P*-*I*), c) heat flow-current (*Q*-*I*), and d) conversion efficiency-current (η-*I*), where the hot- and cold-side temperatures are 323-773 and 298 K, respectively.

The power generation characteristics simulated for the 2π-module composed of *n*-type $Nb_{0.75}Ti_{0.1}CoSb$ and *p*-type $FeNb_{0.9}Ti_{0.1}Sb$ are summarized in Figure 4.3. The HH legs are modeled as a rectangular cross-section of dimensions 3×4 mm^2 (*n*-type) and 3×3 mm^2 (*p*-type) of height 5.6 mm. Both sides of the TE legs are coated with Mo sheets (thickness = 100 μm) as a diffusion layer (Figure 4.2b).

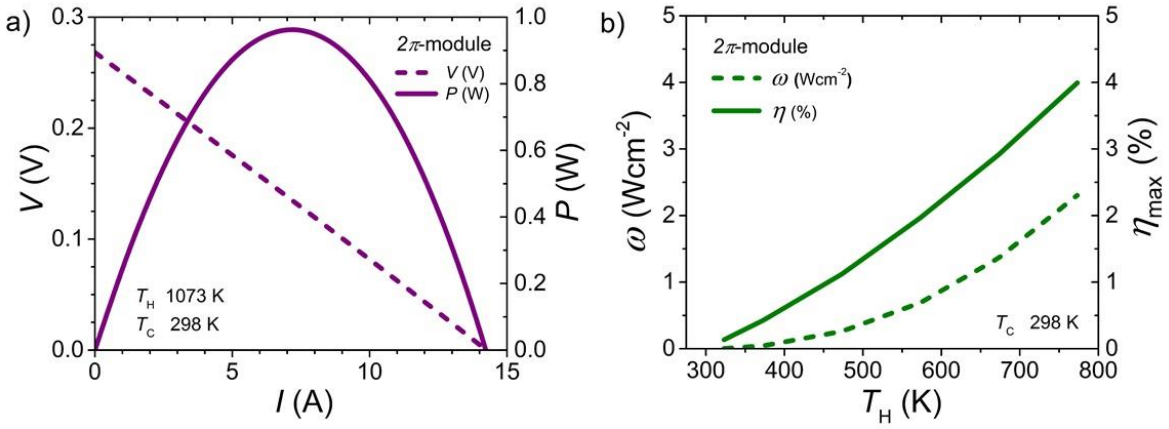

Figure 4.4 Simulation results of characteristic curves of a) power-current (*P*-*I*) obtained where the hot- and cold-side temperatures are 773 and 298 K, respectively and b) power density and conversion efficiency as a function of the hot-side temperature.

Here we set the hot-side temperature as 773 K, because the present study has confirmed that the HH samples are stable up to 773 K in an inert atmosphere. Simulation results of characteristic curves of voltage-current (*V*-*I*), power-current (*P*-*I*), heat flow-current (*Q*-*I*), and conversion efficiency-current (η-*I*) in the hot-side temperature T_H = 323-773 are summarized in Figure 4.4.

Table 4.2 Comparison of different TE module geometry based on HH TE materials.

Materials (*n*/*p*)	**T_C (K)**	**T_H (K)**	**ω_{max} (Wcm^{-2})**	**η_{max} (%)**	**Ref.**
$Nb_{0.85}CoSb$ / FeNbSb	298	773	2.31	4.0	This work
*M*NiSn /*M*CoSn	320	743	0.90	4.0	5
ZrNiSn / FeNbSb	336	991	2.20	6.2	6
*M*NiSn / *M*CoSb	293	820	3.20	5.0	7

At the hot-side temperature T_H = 773 K, the simulated 2π-module exhibits the P_{max} of 0.97 W (Figure 4.4a), resulting in ω_{max} of 2.3 Wcm^{-2} (= P_{max}/A , where A = 0.42 cm^2) and η_{max} of 4.0% as can be seen Figure 4.4b. The present module exhibits higher ω_{max} than those of the reported modules composed of conventional HH compounds, i.e. *M*NiSn /*M*CoSn (ω_{max} = 0.90 Wcm^{-2} , T_C/T_H = 298/773) K [5] and ZrNiSn / FeNbSb (ω_{max} = 2.2 Wcm^{-2} , T_C/T_H = 336/991 K) [6], while η_{max} is comparable to these modules *M*NiSn/*M*CoSn (η_{max} = 4.0%, T_C/T_H = 298/773 K) [5], *M*NiSn/*M*CoSb (η_{max} = 5.0%, T_C/T_H = 293/820 K) [7], and ZrNiSn / FeNbSb (η_{max} = 6.2%, T = 336/991 K) [2], as summarized in Table 4.2.

4.4 Summary

By using the obtained TE data, the power generation performance of a 2π-module composed of the Ti-doped Nb-based HH couple was simulated using the COMSOL code. The maximum power density ω_{max} and the efficiency η_{max} of the 2π-module were 2.3 Wcm^{-2} and of 4.0%, respectively, when the hot- and the cold-side temperatures of T_H = 773 and T_C = 298 K. These results are comparable to or higher than those of the previously developed modules composed of conventional HH compounds under similar operating temperature conditions. The present study reveals that a module composed of Nb-based HH compounds has excellent potential for practical applications with high performance functioning in the high temperature region.

4.5 Reference

[1] COMSOL Multiphysics, http:www.comsol.com.

[2] M. Jaegle, Multiphysics Simulation of Thermoelectric Systems—Modeling of Peltier-Cooling and Thermoelectric Generation. COMSOL Conference, Hannover, 2008.

[3] E.E. Antonova, and D.C. Looman, Finite Elements for Thermoelectric De- vice Analysis in ANSYS. 24th International Conference on Thermoelectrics, 2005.

[4] J. Shen, Z. Wang, J. Chu, S. Bai, X. Zhao, L. Chen and T. Zhu, *ACS Appl. Mater. Interfaces*, 11, 14182-14190 (2019).

[5] X. Hu, A. Yamamoto and K. Nagase, *J. Appl. Phys*., 117, 225102 (2015).

[6] C. Fu, S. Bai, Y. Liu, Y. Tang, L. Chen, X. Zhao and T. Zhu, *Nat. Commun*., 6, 8144 (2015).

[7] K. Bartholome, B. Balke, D. Zuckermann, M. Kohne, M. Muller, K. Tarantik and J. Konig, *J. Electron. Mater.*, 43, 1775-1781 (2014).

Chapter V

Conclusion

This dissertation has aimed to study the behavior of *p*- and *n*-type Nb-based half-Heusler compounds in the viewpoint of (i) thermoelectric performance, such as Seebeck coefficient, electrical conductivity, lattice thermal conductivity and the dimensionless figure of merit (zT), and (ii) thermal stability of these materials; thermal expansion and high-temperature stability. The appropriate couple thermoelectric material based on the Nb-based HH compound able to avoid the ineffective of a module during operating at high-temperature, as can be seen in Figure 5.1.

From the study, we could understand the characteristic of the Nb-based HH module and each *p*- and *n*-type half-Heusler compounds. Firstly, all of *p*- and *n*-type HH samples exhibited high-temperature up to 1073 K in a He atmosphere and 773 K in air. This result shows good agreement with the operating temperature target (673-873 K). Furthermore, the average linear thermal expansion coefficient of *p*- and *n*-type HH samples are good comparable, which would be an excellent candidate to minimize the ineffective of the TE module. Because the $\%\Delta\alpha_L$ of 14% is smaller than another couple of TE material, it can be confirmed from the literature data in Table 1.2 that the percentage of linear thermal expansion different in this study is acceptable due to lower than another thermoelectric couple. Secondly, *p*-type $Nb_{0.9}Ti_{0.1}FeSb$ exhibited the highest power factor. As a result, the Ti-substituted sample exhibited the best zT values, zT_{max} = 0.7 at 1073 K. While *n*-type $Nb_{0.75}Ti_{0.1}CoSb$ exhibited lower power factor than *p*-type, but lattice

thermal conductivity of *n*-type shows extremely lower than *p*-type $Nb_{0.9}Ti_{0.1}FeSb$. These characters lead to enhance *zT* in *n*-type samples, the best *zT* of *n*-type is around 0.7 at 1073 K, which close to the *p*-type sample. Besides the substitution technique, it is possible to suppress more κ_{lat} by introducing nanostructure in the half-Heusler compound. This strategy can be achieved via a combination of malt-spinning and spark plasma sintering method.

Therefore, for an appropriated couple for fabricating a TE module, it can be concluded that the Ti-doped system is the best system among the other systems in both *n*-and *p*-type Nb-based HH compounds. By using the obtained thermoelectric properties data, the power generation performance of a 2π-module consist of the Ti-doped Nb-based HH compound is simulated using the COMSOL code. The maximum power density ω_{max} and the efficiency η_{max} of the 2π-module were 2.3 Wcm^{-2} and of 4.0%, respectively, when the hot- and the cold-side temperatures of T_H = 773 and T_C = 298 K. These results are comparable to or higher than those of the previously developed modules composed of conventional HH compounds under similar operating temperature conditions. The present study reveals that a module consisting of Nb-based HH compounds has excellent potential for practical applications with high-performance functioning in the high-temperature region as the expectation of this study.

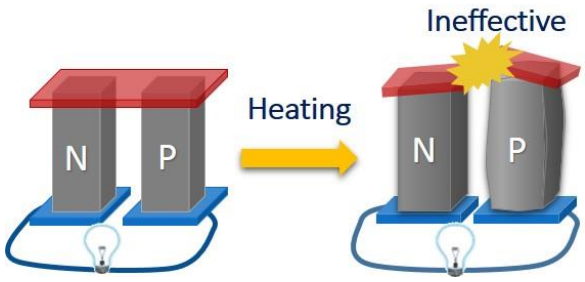

Figure 5.1 Thermoelectric module during working on temperature difference.

Acknowledgments

I would first like to thank my supervisor Assoc. Prof. Hiroaki Muta for helpful advice on my study. I would like to express my sincere gratitude to my co-supervisor, Prof. Ken Kurosaki for providing me instructive support, kind guidance and valuable discussions on my research during my Ph.D. course. I would like to express my gratitude to Prof. Shinsuke Yamanaka for warm welcome in the first day at this laboratory. I am grateful to Assist. Prof. Yuji Ohishi for kind help and constructive comments. I am also indebted to the dissertation committee, Prof. Takao Yamamoto, Prof. Takaori Kitada, and Assoc. Prof. Yoko Akiyama for helpful comments and suggestions on my dissertation.

I would acknowledge to Michihiro Ohta sensei who gave me an invaluable opportunity for assembling thermoelectric module at AIST Tsukuba Center. Aihara Makoto, Naoko Fujimoto, Ichiro Okumura are expert technicians thanked for their help during the work at AIST. A post-doctoral at AIST, Raju Chetty is thanked for valuable suggestions in the calculation part of my work.

My thankfulness is also expressed to the support of my lab members who taught me a lot of experiment research, helpful advice and encouragement in my student life. My pleasure to work with them. Thanks to my lovely Thai friend who studies in Japan and also in Thailand for supporting me every single day in Ph.D. life.

Finally, I would like to thank my sweet parents and family members for their endless encouragement, understanding and love.

December 2019

Wanthana Silpawilawan

Research Achievements

Publications

Thesis Related Publications

1. **FeNbSb *p*-type half-Heusler Compound: Beneficial Thermomechanical Properties and High-temperature Stability for Thermoelectrics**

   Journal of Material Chemistry C, 2017, **5**, 6677-6681.

   Wanthana Silpawilawan, Ken Kurosaki, Yuji Ohishi, Hiroaki Muta, and Shinsuke Yamanaka

2. **Thermoelectric Properties of *p*-Type Half-Heusler Compounds $FeNb_{0.9}M_{0.1}Sb$ (*M* = Ti,Zr,Hf)**

   Materials Transactions, 2018, **59**, 1030-1034.

   Wanthana Silpawilawan, Yuji Ohishi, Hiroaki Muta, Shinsuke Yamanaka, and Ken Kurosaki

3. **Realizing of Excellence *n*- and *p*-type Niobium-based Half-Heusler Compounds Based on Thermoelectric Properties and High-temperature Stability**

   Advanced Electronic Materials, 2019, **xx**, xxxx-xxxx.

   Wanthana Silpawilawan, Sora-at Tanuslip, Raju Chetty, Michihiro Ohta, Yuji Ohishi, Hiroaki Muta, and Ken Kurosaki

Others Publications

4. **Thermal and Mechanical Properties of U_3Si and USi_3**

   Annals of Nuclear Energy, 2019, **133**, 186-193.

   Afiqa Mohamad, Wanthana Silpawilawan, Hiroaki Muta, Ken Kurosaki, and Yuji Ohishi

5. **Enhancing Thermoelectric Properties of Higher Manganese Silicide (HMS) by Partial Ta Substitution**

   Journal of Electronic Materials, 2019, doi.org/10.1007/s11664-019-07673-x.

   Nuttawat Parse, Sora-at Tanusilp, Wanthana Silpawilawan, Ken Kurosaki, and Supree Pinitsoontorn

Conferences

Oral Presentation:

2017 The 36th International Conference on Thermoelectrics, Pasadena, Californian, United States, July 31-August 3, 2017.

"**Thermomechanical Properties and High-temperature Stability of FeNbSb *p*-type Half-Heusler Compound**"

2018 Material Research Society (Autumn Meeting), Boston, Massachusetts, United States, November 25-30, 2018.

"**Effect of Element Substitution on The High-temperature Stability and Thermoelectric Properties of $FeNb_{0.9}M_{0.1}Sb$ (*M*=Ti, Zr, Hf) Half-Heusler Compounds**"

2018 The 5th Southeast Asia Conference on Thermoelectrics, Siem Reap, Cambodia, December 14-17, 2018.

"**Half-Heusler FeNbSb: Stability and Thermoelectric Properties**"

2019 The 2nd Materials Research Society of Thailand International Conference, Pattaya, Thailand, July 10-12, 2019.

"**Thermoelectric Properties of Nanostructured Ti-doped FeNbSb Half-Heusler Compound Synthesized by a Melt-spinning/spark Plasma Sintering Technique**"

Poster Presentation:

2017 The 15th International Conference on Advanced Materials, Kyoto, Japan, August 27-September 1, 2017.

"**Thermomechanical Properties and High-temperature Stability of FeNbSb-based *p*-type half-Heusler Compound**"

2017 The 14th Thermoelectric Society Japan Conference, Osaka, Japan, September 11-13, 2017.

"**High-temperature XRD Analysis on *p*-type Half-Heusler Compounds: FeNbSb and ZrCoSb**"

Award:

2018 **Best Oral Presentation Award** at The 5th Southeast Asia Conference on Thermoelectrics, Siem Reap, Cambodia, 2018.